DISSERTATION

Defence held on 11/11/2020 in Luxembourg

to obtain the degree of

DOCTEUR DE L'UNIVERSITÉ DU LUXEMBOURG

EN INFORMATIQUE

by

Jevgenij KRIVOCHIZA
Born on 19 February 1988 in Visaginas, Lithuania

END-TO-END SIGNAL PROCESSING
ALGORITHMS FOR PRECODED SATELLITE
COMMUNICATIONS

Dissertation defence committee

Dr. Symeon Chatzinotas, dissertation supervisor
Professor, Université du Luxembourg

Dr. Bjorn Ottersten, Vice-Chairman
Professor, Université du Luxembourg

Dr. Jens Krause
Satellite Telecommunications Systems, SES Satellites

Dr. Fredrik Tufvesson
Professor, Lund University

Dr. Miguel Angel Olivares Mendez, Chairman
Assistant Professor, Université du Luxembourg

Abstract

The benefits of full frequency reuse in satellite communications consist of increased spectral efficiency, physical layer security, enhanced coverage, and improved Quality of Service. This is possible due to novel digital signal processing techniques for interference mitigation as well as signal predistortion in non-linear high-performance amplifiers. Advanced linear precoding and symbol-level precoding can jointly address the signal processing demands in the next-generation satellite communications. The real-time signal precoding increases the computational complexity handled at the gateway, thus requiring low-complexity high-performance algorithms to be developed. Additionally, extensive in-lab and field tests are required to increase the technology readiness level and industrial adaption rate. In this thesis, we focus on low-complexity precoding design and in-lab validations. We study the state-of-the-art linear and symbol-level precoding techniques and multi-user MIMO test-beds available in the literature. First, we present a novel low-complexity algorithm for sum power minimization precoding design. This technique allows to reduce transmitted power in a multi-beam satellite system and improves the quality of the received signal at user terminals. Next, we demonstrate an FPGA accelerated high-throughput precoding design. The FPGA precoding design is scalable for a different number of beams in the systems and operates in a real-time processing regime using a commercially available software defined radio platform. One of the highlights of this research is the creation of a real-time in-lab precoding test-bed. The test-bed consists of a DVB-S2X precoding enabled gateway prototype, a MIMO channel emulator, and user terminals. By using the radio frequency for transmitting and receiving the precoded signals, we can test the performance of different precoding techniques in realistic scenarios and channel impairments. We demonstrate an end-to-end symbol-level precoded real-time transmission, in which user terminals can acquire and decode the precoded signals showing an increase in performance and throughput. The in-lab validations confirm numerical results conducted alongside in this work.

Acknowledgements

Acknowledgements

I would like to express my gratitude to all the people I have met and worked with at the University of Luxembourg, the Société Européenne des Satellites (SES), and the European Space Agency (ESA). Their support and contributions were invaluable though all the past years.

Acknowledgements

Table of Contents

List of Abbreviations

5G	Fifth Generation Mobile Technology.
5GPPP	The 5G Infrastructure Public Private Partnership.
ACM	Adaptive coding and modulation.
ADC	Analog-to-digital converter.
APSK	Amplitude and phase-shift keying.
AWGN	Additive White Gaussian Noise.
BER	Bit error rate.
CDMA	Code-division multiple access.
CI	Constructive interference.
CF	Closed-form.
CSI	Channel State Information.
CVX	Convex optimization.
DAC	Digital-to-analog converter.
DSP	Digital signal processor.
DVB-S2	Digital Video Broadcasting - Satellite - Second Generation.
DVB-S2X	Extension of DVB-S2 satellite digital broadcasting standard.
FDD	Frequency-division duplexing.
FDM	Frequency-division multiplexing.
FER	Frame error rate.

FPGA   Field-programmable gate array.

GW   Gateway.

HDL   Hardware Description Language.

HLS   High-Level Synthesis.

HPA   High power amplifier.

I/O   The input and output.

I/Q   In-phase and quadrature.

ITU-R   The ITU Radiocommunication Sector.

LDPC   Low-density parity-check code.

LLR   Log-likelihood ratio.

LTE   Long Term Evolution.

LUT   Look-up table.

MIMO   Multiple-input and multiple-Output.

MISO   Multiple-input and single-Output.

MMSE   Minimum-mean-squared-error.

MRT   Maximum Ratio Transition.

NNLS   Non-negative least squares.

QoS   Quality-of-Service.

OFDM   Orthogonal frequency division multiplexing.

RF   Radio frequency.

PAPR   Peak-to-average power ratio.

PSK   Phase-shift keying.

QAM   Quadrature amplitude modulation.

QPSK   Quadrature phase-shift keying.

RTL   Register-transfer level.

SATCOM   Satellite communications.

SDM   Space-division multiplexing.

SDR   Software defined radio.

SINR   Signal-to-interference-and-noise ratio.

SNR   Signal-to-Noise ratio.

SLP   Symbol-level precoding.

TDD   Time-division duplexing.

TDM   Time-division multiplexing.

UHTS   Ultra High Throughput Satellites.

USRP   Universal Software Radio Peripheral.

UT   User terminal.

VP   Vector perturbation.

WH   Walsh-Hadamard.

ZF   Zero-forcing.

List of Notation

β Roll-off factor.

γ_i SINR threshold/demand at the i-th UT.

$\mathbf{a}$ Column vectors.

$\mathbf{A}$ Matrix.

min   Minimum.

σ Noise variance.

$\mathbb{C}$ Set of complex numbers.

$\mathbb{R}$ Set of real numbers.

C_R Code rate.

B_w Bandwidth.

M Modulation order.

$\mathcal{I}$ Identity matrix.

ι Imaginary unit $\iota = \sqrt{-1}$.

$(\cdot)^{\dagger}$ Matrix transpose.

$(\cdot)^{H}$ Hermitian transpose.

$(\cdot)^{-1}$ Matrix inverse.

$\lVert \cdot \rVert_2$ Euclidean norm.

κ_2 2-norm matrix condition number.

N_t Number of transmit antennas.

N_u Number of UTs.

n_i Independent complex circular symmetric independent identically distributed zero mean noise measured at the i-th UT.

O	Asymptotic computational complexity.
$\lvert \cdot \rvert$	Absolute value of a complex number.
$(\bullet)$	Element-wise vector multiplication.
diag$[\cdot]$	Square diagonal matrix with the elements defined on the main diagonal.
0	All elements zero vector.
trace	Sum of all diagonal elements of a matrix.
$\mathrm{Re}(\cdot)$	Real part of a complex number.
$\mathrm{Im}(\cdot)$	Imaginary part of a complex number.

List of Tables

List of Figures

Preface

This Ph.D. Thesis has been carried out from March 2017 to September 2020 at the Interdisciplinary Centre for Security, Reliability and Trust (SnT), University of Luxembourg, Luxembourg, under the co-supervision of Prof. Symeon Chatzinotas and Prof. Björn Ottersten at SnT, University of Luxembourg, Luxembourg, and Dr. Jens Krause at SES S.A., Luxembourg. The timely evaluation of the Ph.D. Thesis was duly performed by the CET members constituting the supervisors at SnT, University of Luxembourg, Luxembourg. The fruitful discussions during the SES S.A. meetings and suggestions are gratefully acknowledged.

Support of the Thesis

Publications

Below is a list of original publications that have been produced during the period of Ph.D. candidacy, which are referred to in the text by **J** ≡ Journal, **B** ≡ Book Chapter, **C** ≡ Conference and **S** ≡ Survey Paper.

Journal Papers

[**J1**] A. Li, D. Spano and J. Krivochiza, S. Domouchtsidis, C. Tsinos, C. Masouros, S. Chatzinotas, Y. Li, B. Vucetic, B. Ottersten, **"Interference Exploitation via Symbol-Level Precoding: Overview, State-of-the-Art and Future Directions,"** in *IEEE Communications Surveys and Tutorials*, 2020.

[**J2**] J. Krivochiza, J. Merlano Duncan, S. Andrenacci, S. Chatzinotas, B. Ottersten, **"FPGA Acceleration for Computationally Efficient Symbol-Level Precoding in Multi-User Multi-Antenna Communication Systems,"** in *IEEE Access*, vol. 7, pp. 15509-15520, 2019.

[**J3**] J. Krivochiza, J. Merlano Duncan, S. Andrenacci, S. Chatzinotas, B. Ottersten, **"Computationally and energy efficient symbol-level precoding communications demonstrator,"** in *Physical Communication*, vol. 28, pp. 108-115, 2018.

Book Chapter

[**B1**] A. Stefano, J. Merlano Duncan, J. Krivochiza S. Chatzinotas, **"Satellite Multi-Beam Precoding Hardware Demonstrator,"** in *Satellite Communications in the 5G Era*, IET, September 2019, pp. 249-275.

Conference Papers

[**C1**] J. Krivochiza, J. C. Merlano-Duncan, S. Chatzinotas, B. Ottersten, **"M-QAM Modulation Symbol-Level Precoding for Power Minimization: Closed-Form Solution,"** in *2019 16th International Symposium on Wireless Communication Systems (ISWCS)*, Oulu, Finland, August, 2019.

[**C2**] N. Maturo, J. C. Merlano-Duncan, J. Krivochiza, J. Querol, D. Spano, S. Chatzinotas, B. Ottersten, **"Demonstrator of Precoding Technique for a Multi-Beams Satellite System,"** in *2019 8th International Workshop on Tracking, Telemetry and Command Systems for Space Applications (TTC)*, Darmstadt, Germany, September, 2019.

[**C3**] J. C. Merlano-Duncan, J. Querol, N. Maturo, J. Krivochiza, D. Spano, S. Norshahida, L. Martinez Marrero, S. Chatzinotas, B. Ottersten, **"Hardware Precoding Demonstration in Multi-Beam UHTS Communications under Realistic Payload Characteristics,"** in *37th International Communications Satellite Systems Conference (ICSSC2019)*, Okinawa, Japan, October, 2019.

[**C4**] J. Krivochiza, J. C. Merlano-Duncan, S. Andrenacci, S. Chatzinotas, B. Ottersten, **"Closed-Form Solution for Computationally Efficient Symbol-Level Precoding,"** in *2018 IEEE Global Communications Conference (GLOBECOM)*, Abu Dhabi, United Arab Emirates, December, 2018.

[**C5**] J. Duncan, J. Krivochiza, S. Andrenacci, S. Chatzinotas, B. Ottersten, **"Hardware demonstration of precoded communications in multi-beam UHTS systems,"** in *36th International Communications Satellite Systems Conference (ICSSC 2018)*, Niagara Falls, ON, Canada, October, 2018.

[**C6**] J. C. Merlano-Duncan, J. Krivochiza, S. Andrenacci, S. Chatzinotas, B. Ottersten, **"Computationally efficient symbol-level precoding communications demonstrator,"** in *2017 IEEE 28th Annual International Symposium on Personal, Indoor, and Mobile Radio Communications (PIMRC)*, Montreal, QC, October, 2017.

[**C7**] J. Krivochiza, A. Kalantari, S. Chatzinotas, B. Ottersten, **"Low Complexity Symbol-Level Design for Linear Precoding Systems,"** in *2017 Symposium on Information Theory and Signal Processing in the Benelux*, Delft, Netherlands, May, 2017.

Side Publications during PhD

[**J4**] C. Politis, S. Maleki, J. M. Duncan, J. Krivochiza, S. Chatzinotas, B. Ottesten, **"SDR Implementation of a Testbed for Real-Time Interference Detection With Signal Cancellation,"** in *IEEE Access*, vol. 6, pp. 20807-20821, 2018.

[**C8**] J. C. Merlano-Duncan, J. Querol, L. Martinez Marrero, J. Krivochiza, A. Camps, S. Chatzinotas, B. Ottersten, **"SDR implementation of a Synchronization Link for Coherent Distributed Remote Sensing Systems"** - in *2020 IEEE International Geoscience and Remote Sensing Symposium*, July, 2020.

[**C9**] S. Gautam, J. Krivochiza, A. Haqiqatnejad, S. Chatzinotas and B. Ottersten, **"Boosting SWIPT via Symbol-Level Precoding"** - in *2020 IEEE 21st International Workshop on Signal Processing Advances in Wireless Communications (SPAWC)*, Atlanta, GA, USA, May, 2020.

Chapter 1

Introduction

1.1 Problem Overview and Motivation

The 5th generation of mobile radio communications systems should provide a high level of integration and flexibility between different types of telecommunication networks. Terrestrial and satellite systems historically were developed independently of each other which results in technological diversity between the networks. The launched 5GPPP research program co-funded by the European Commission is set to work towards a definition of a new common standard for 5G networks [1]. The objective of the project METIS 2020 as a part of 5GPPP is to build the foundation for a future mobile and wireless communications system for 2020 and beyond [2]. These standards allow seamless joint operation of mobile cellular communications and satellite systems as a single service. The use cases of modern satellite communications (SATCOM) systems in 5G networks include increasing coverage of conventional terrestrial cells, facilitating caching through multicast/broadcast data transmission, and providing off-load backhauling for unicast user traffic [3].

The main driving commercial applications behind SATCOM technologies were and remain services like television and different types of data broadcasting. The new era of broadband internet and on-demand services brings new challenges to the design ideas behind SATCOM systems. The market importance of broadband services and the limited frequency resources pushes the SATCOM industry and academia towards the development of novel, more efficient, and smart wireless communication technologies. The energy efficiency of the SATCOM systems is an additional issue on the way towards new generation networks. Therefore, it becomes crucial to define and investigate new network architectures that can support higher system spectrum and energy efficiency, while providing large-scale coverage and availability. To reduce the cost of SATCOM missions, a single wideband onboard High-Power Amplifier (HPA) is used for multiple carrier amplification. This approach in comparison to the conventional narrowband amplifier per link design allows reducing the power consumption, heat emission, and complexity of a cooling system while lowering the amount of the payload mass [4].

In SATCOM, aggressive reuse of available spectrum resources by exploiting Multi-user multiple-input multiple-output (MU-MIMO) techniques brings the following benefits: increased spectral efficiency; fairness of SINR over users; optimization of satellite transponders transmit power; advanced interference mitigation; enhanced security of the physical layer (PHY). Major research on MU-MIMO precoding techniques and interference in previous

works [5–8] promise optimistic theoretical results in terms of increased SINR, more efficient bandwidth utilization, and higher satellite throughput. The next challenge towards the novel SATCOM paradigm is to design and research a realistic MU-MIMO transmitter for SAT-COMs, which would exploit the potential of the precoding techniques.

In this sense novel software defined radio (SDR) platforms allow us to prototype a PHY level of MIMO wireless systems of high complexity and scalability. The SDR platform generally consists of two parts: analog-to-digital (ADC) and digital-to-analog (DAC) converters preceded by radio frequency (RF) front end on the hardware side and signal processing on the software side, where the former should fall in with the latter. The software side can perform with high precision all the analytical calculations. The hardware side, though, due to the nature of the physical properties of the wireless channel and RF chains impose restrictions on the design of the transmitter. The SDR implementation would subject precoding algorithms to frequency and phase misalignments, quantization noise of multichannel ADC and DAC, non-linearities of RF components. The performance of a MIMO precoder is likewise reduced due to signal carrier frequency and phase mismatching between a transmitter and users' receivers. Correction of these impairments must be considered in the design of the receivers. On the other hand, to enable the efficient utilization of satellite transponders, multiple carriers have to be relayed through a single high power amplifier (HPA). However, the non-linear nature of HPAs results in adjacent channel interference and increased Peak-to-average power-ratio (PARP), which limits the expected performance gains. In this context, studies on energy-efficient on-board digital predistortion techniques, to maximize the performance of HPAs by uniformly distributing the power load are required [9]. A system could operate continuously very close to the saturation point by applying advanced precoding techniques. For the same reason, the impact of the MIMO precoding techniques on a shape and distortions of a signal frequency spectrum must be studied as well. Furthermore, the MU-MIMO precoder at the transmitter utilizes a closed-loop approach by employing the retrieved channel state information (CSI) from the user terminals (UTs), hence, a feedback channel is required for precoding to operate.

Accuracy of the CSI estimations, which are affected by imperfections of the transmitter and all the receivers, and relevance due to the time-varying nature of a wireless channel are not perfect in real communications systems [10]. The long round trip time and restrictive feedback channel capacity bring complementary challenges for the CSI based precoding. Generally, due to the inability of acquiring instantaneous CSI at the gateway (GW) precoding for mobile satellite systems can be very challenging and impose additional limitations on the precoder design. However, there is potential for specific types of applications such as aeronautical/maritime systems, where the channel is predictable and there is no direct blockage of the line of sight component [11]. Alternatively, open-loop precoding techniques are studied for satellite communication systems [12].

Also, MU-MIMO precoding techniques, which are defined as optimization problems, require solution by time-consuming iterative Convex optimization (CVX) or Non-negative least squares (NNLS) solving methods that must fit into relevant time window [4]. Hence, further research on the optimization of the methods processing times to meet channel requirements and current SDR computation power is required.

Thereby, the problem of integrating multicast satellite precoding algorithms into the over-the-air transmitter is taken into consideration. The active development of end-to-end signal processing algorithms for precoded SATCOM concerns as well the practical implementation aspects of computational complexity [13] and large-scale MIMO arrays [14]. Facing the design issues of the theoretical approaches while creating a practical implementation leads

us to a self-sustained evolution of the previously developed precoding techniques generating new valuable knowledge in the academic and industrial fields of study.

1.2   Main Contributions of this Thesis

In this thesis, we investigate SLP implementation and application in realistic communications systems. In this scope, we design low complexity algorithms to address hardware processing limitations. Also, we build a precoding test-bed using the state-of-the-art SDR equipment for in-lab real-time verification of the precoding algorithms. The synergy of the in-lab verification and custom design of the precoding algorithm enables us to further analyze and achieve the high system symbol rates at the low computational complexity cost. We verify the feasibility and the gains of SLP over the conventional MU-MIMO precoders in terms of complexity, SINR, and data rate.

We propose a framework for SLP design and devised a closed-form algorithm to solve NNLS problems with a limited number of computational resources. We show both in numerical simulations and in-lab demonstration that the closed-form algorithm provides a feasible solution for convex optimization problems with a limited number of computational operations and delivers enhanced performance in receivers.

The main contributions of the thesis are listed are as follows:

- Novel precoding algorithms with computational complexity optimization: Carried out the practical design of the SLP algorithms and proposed the enhanced solution for the SLP implementation. The necessary steps were considered towards practically reasonable novel precoding design development, re-imagining the outcomes of the previously achieved findings in the literature.

- Precoding enabled gateway, user terminals, and channel emulator for SATCOM: In the course of the thesis preparation, a considerable amount of work was put into the development of an in-lab real-time precoding demonstrator with satellite multi-beam channel emulator for benchmarking and validating the performance of the precoder design in close-to-reality conditions and facilitate further design improvements in a practical environment.

- End-to-end precoding algorithms in-lab tests: Numerical approximations of the precoding performance were validated with the in-lab data from the over-the-cable real-time test-bed.

The main areas of this thesis are SLP algorithms optimization, computational complexity reduction, practical precoder implementation, and in-lab demo development and validation. In this context, convex optimization problems relative to the subject are formulated, explained and efficient solutions are proposed. The prototyping tools and the implementation design used for the in-lab validation are extensively discussed as well.

1.3   Organization of the Thesis

The Thesis comes in eight chapters as follows:

- Chapter 2 gives an overview of the state-of-the-art in interference management in multi-antenna systems, in particular SLP. It highlights the main challenges of the practical implementation found in the existing literature. [**J1**], [**B1**].

- In Chapter 3 we propose a for sum power minimization SLP technique for M-th order phase-shift keying (M-PSK), and amplitude and phase-shift keying (M-APSK) symbol constellations, used in SATCOM. We construct a quadratic convex minimization problem and derive a high-performance closed-form solution. [**C4**].

- In Chapter 4 we focus on sum power minimization SLP for M-QAM symbol constellations for terrestrial wireless communication. We show that despite M-QAM constellations have different symbol mapping from M-APSK, making the convex optimization problem more difficult, we can modify and apply the same closed-form solution to efficiently solve the problem. [**C1**].

- In Chapter 5 we elaborate on the closed-form solution design to operate it in the real-time mode using FPGA hardware acceleration. We present a complete design of an efficient SLP technique for modern SDR equipment and benchmark it against numerical simulations. [**J2**].

- In Chapter 6 we demonstrate the in-lab test-bed for real-time precoded communications. The test-bed is used to validate precoding techniques available in the literature and developed in this Thesis. [**C2**], [**C3**], [**C5**].

- In Chapter 7 we benchmark the sum power minimization SLP for M-PSK performance using the in-lab test-bed.

- We validate the design of the sum power minimization SLP for M-QAM in Chapter 8. [**J3**], [**C6**] [**C7**].

- We conclude in Chapter 9 with our main research findings and discuss the possible extensions.

Chapter 2

Multiple-Antenna Communication Systems: Overview

Interference in wireless systems was considered as a harmful impairment and different communication standards like TDM, FDM, CDMA, etc. were devised to avoid transmissions in the same physical channel and suppress interference harming effect on wireless services. The emerging technology of active beamforming allowed to elaborate on the idea of space-division multiplexing (SDM) to reuse the same frequency and time resources in multiple simultaneous transmissions. Basic SDM is based on power control and high beam directivity. With evolving digital signal processors (DPS) and SDR technologies, SDM can explore advanced interference mitigation techniques.

2.1 Multi-Antenna Transmit Systems

Phased-arrays were fast-growing technology in the past decades. The technology was applied in a wide range of communications and radar systems. The discrete solid-state active phased arrays like the Swedish Erieye [15] and solid-state MMIC (monolithic microwave integrated circuit) active phased arrays like the L-band cellular-satellite IRIDIUM are one of the highlights of the progress in the field [16].

Other applications can be found in acoustic active arrays for ultrasonic image reconstruction [17]. Acoustic imaging technology is now widely used for medical purposes, underwater imaging, and nondestructive testing applications. Acoustic imaging in the air became popular with advances in air-coupled transducers [18].

In recent years, transmitter arrays found their application in wireless power transfer [19], becoming an underlying paradigm for simultaneous data and power transfer communications [20–23]. Another related interference scenario is found in very-high-bit-rate digital subscriber line (VDSL) technology [24, 25]. The multi-antenna configuration is used for spatial diversity to increase signal-to-interference and noise ratio by reducing the fading effect [26]. Additionally, a multi-antenna setup can be used for optimal antenna selection for channel capacity maximization [27]. Passive and reconfigurable antenna arrays are used to enhance antenna radiation directivity [28]. Advanced transmit diversity techniques are possible on multi-antenna systems with an addition of DSP [29]. Furthermore, fully digital baseband based multiple independent data streams for each spatial location were first demonstrated in 1991 by ArrayComm company [30].

2.2 Beamforming and Precoding

Precoding is a design of the transmitted signals to efficiently deliver the intended data to the transmitters. Precoding has been studied recently as a way to reduce co-channel interference in wireless communications (Wi-Fi, LTE) and multi-beam satellite systems [31–34]. Some precoders can be tailored for the spectrum or power efficiency. Other precoders are designed with hardware impairments in mind, like amplifier non-linearities and digital-to-analog converter (DAC) quantization errors [35]. For optimal precoder design, dynamic channel characteristics have to be measured or modeled.

Downlink channel response can be measured at the receiver side and feedback to the transmitter. In the TDD systems, the transmitter can use channel reciprocity to measure the estimated channel directly from the uplink signals. In satellite systems channel reciprocity is not applicable due to many reasons. In SATCOMs, FDD is used for forward and return links instead of TDD. Switching between forward and return links in the TDD manner is inefficient due to considerable signal propagation delays and the particularities of the design of satellite payloads. Also, in a satellite payload, the return and forwards links are relayed through different radio components, thus they experience different channel impairments. Instead, implicit receiver-sided channel estimation [36] or codebook based CSI techniques are required. Precoders use CSI to calculate optimal weights for each data stream and transmit antenna. The optimal weights are subject to a particular precoder design.

Interference in wireless communication systems is considered a performance-limiting factor. In a MU-MIMO transmission, the interference occurs from the superposing of the transmitted signals for different users sharing the same channel resources. Linear precoding techniques with prior knowledge of CSI efficiently mitigate the interference at the user side with a predistortion of the transmitted modulated signals at the transmitter to cancel the interference as shown in Fig. 2.1a. Linear precoding is calculated once per transmitted frame and applied to all symbols irrespective of a symbol's value.

A classical maximal ratio transmission (MRT) [37] technique calculates the weights of the signals from the multiple transmit antennas such that the signal-to-noise ratio (SNR) of their sum is maximized in the absence of interference, or when interference is negligible compared to the background noise. The transmit antenna weights are matched to counter channel fading.

In zero-forcing (ZF) beamforming [38] the weights are calculated based on the channel inverse. Channel inversion is one of the simplest interference mitigation techniques for the multi-user interference-limited channel [39]. This technique multiplies the vector signal to be transmitted by the inverse of the channel matrix creating orthogonal channels to each user. Regularizing the inverse (RZF) improves the performance over the ZF performance [40]. Generally, the regularized precoder is obtained via minimizing the mean square error (MSE) between the transmitted and received symbols, which is, thus, also termed as minimum MSE (MMSE) precoder [41, 42]. These methods were further studied and extended in the recent works [43, 44]. MMSE is especially useful for poorly conditioned channel matrices and provides better SINR than ZF [40] in noise-limited scenarios.

Truncated polynomial expansion (TPE)-based precoding is a recently proposed technique to reduce the computational complexity of RZF precoder while maintaining similar performance [45, 46]. It has been shown that even for a small number of matrix polynomial terms, TPE-based schemes closely approach the sum rate and the minimum user rate of the optimal RZF precoder. In terms of computational complexity, by using an appropriate implementation technique, e.g., Horners scheme, significant computation reduction can be achieved as

(a) Linear precoding

(b) SLP

(c) Linear precoding
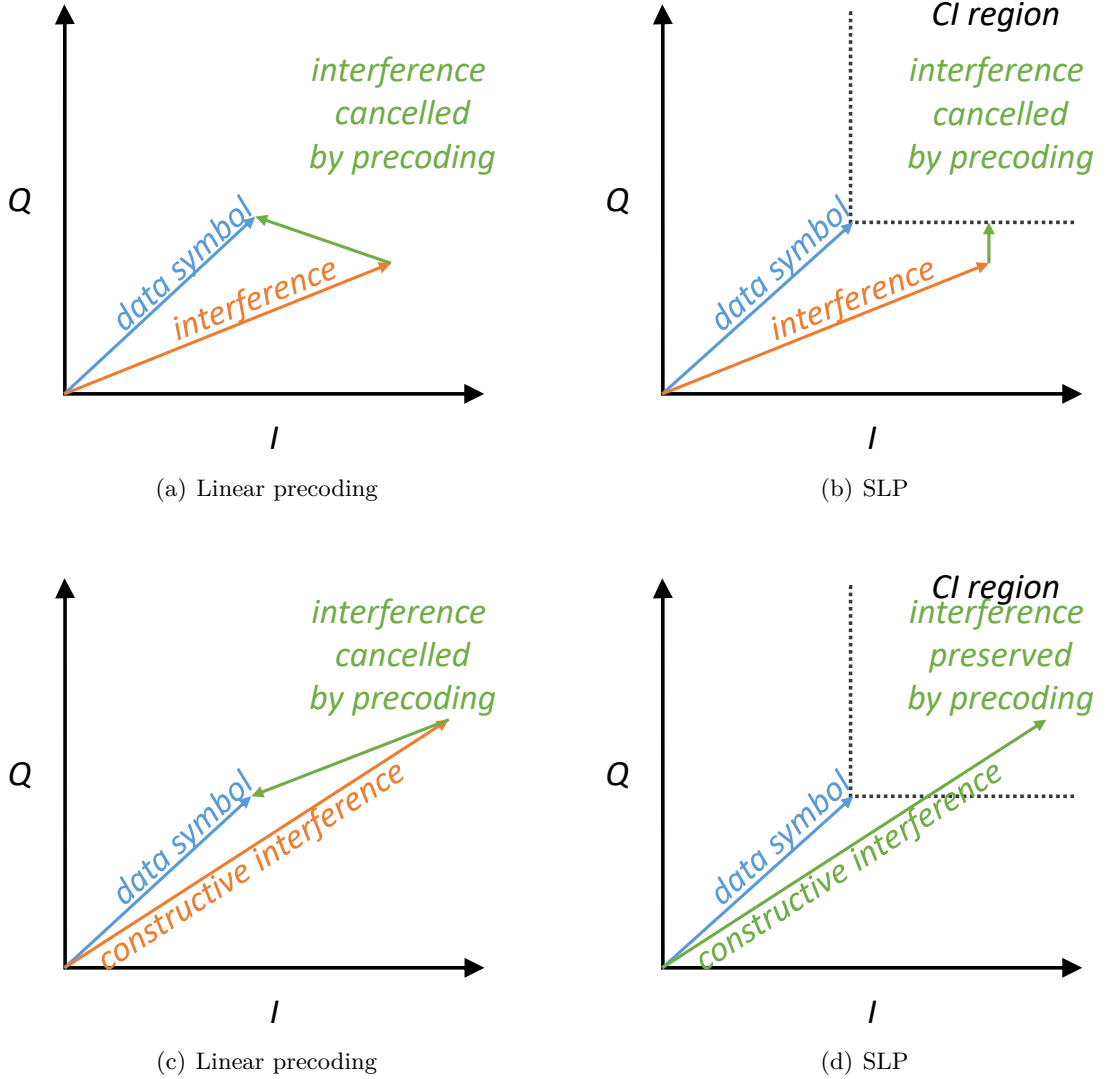
(d) SLP

FIGURE 2.1: Interference management in the I/Q plane for linear precoding and SLP.

compared to the RZF precoder [47].

2.3 Symbol-Level Precoding

On the other hand, SLP techniques are managing interference on an instantaneous transmitted symbol level [48] instead of a transmitted frame. Aware of the correct constructive interference (CI) regions of each data symbol, SLP can manage interference more efficiently as shown in Fig. 2.1b. Also, SLP can preserve CI components in the received signal, such that the interference positively contributes to the data signal power as shown in Fig. 2.1d. While linear precoding techniques in a similar scenario will attempt to cancel CI as shown in Fig. 2.1c. Therefore, CI is the interference that pushes the data signals further into CI regions defined by the selected modulation scheme. SLP exploits the effect of CI as an additional degree of freedom to optimize precoded signals at the transmitter side. Thought it becomes

apparent, that SLP has to be designed specifically for every considered modulation scheme.

The design of SLP can serve different optimization targets of the transmitted signal waveform. In this context, SLP is actively studied in recent works [44, 49, 49–53]. In [54], the authors use a novel SLP approach to mitigate user interference in both spatial and temporal domains of a MIMO channel. Consumed power minimization and green energy are trending in modern smart wireless communications [55]. In this scope, the technique to reduce spatial peak-to-average power ratio (PAPR) is proposed in [56, 57], while in [58] the approach is used for the peak power minimization. SLP was applied to minimize the transmission power for green wireless communications [55]. On the other hand, academic research shows that precoding techniques in SATCOM potentially allow more efficient spectral utilization and substantially higher service availability [59–61]. In this context, studies on energy efficient onboard predistortion techniques for HPAs, to maximize the performance by uniformly distributing the power load are conducted [62–64].

2.4 Precoding for SATCOM

The new era of broadband internet and on-demand services challenges to come up with new approaches towards the design of the SATCOM systems. The market importance of broadband services and the limited frequency resources drive the SATCOM industry and academia towards the development of novel smart and more efficient in terms of power and frequency wireless communication technologies. Multi-beam satellites, on the one hand, are more power-efficient and, on the other hand, have higher capacity in the satellite channel through the spatial multiplexing [65]. While conventional multi-beam systems employ the 4 color reuse (4CR) scheme to mitigate interference between the beams, precoding enabled full frequency reuse (FFR) schemes are more efficient. Therefore, the application of MIMO in SATCOM is highly challenging due to the practical constraints, but at the same time, extremely rewarding academic tasks [66, 67] from both literature and project point of views. The authors in [68] present a real-time demonstrator for precoded communications in multi-beam satellites. In [69] the closed-loop ZF precoded transmission is demonstrated over-the-air satellite link showcasing precoding practical application.

Recent works studied the practical application of precoding in SATCOM [4, 12, 32, 34, 67, 70–73]. Moreover, the SLP approach provides extra flexibility to improve the efficiency of satellite payloads. The authors in [62] propose a novel SLP design to reduce the power peaks in the transmitted signal to efficiently drive the nonlinear HPS and reduce the detrimental saturation effect. In [56] the authors demonstrate a technique for spatial PAPR reduction in the multi-beam satellite downlink. While the authors in [74] present a precoding technique at the gateway of a multi-beam mobile satellite systems to enable a robust full frequency reuse pattern among the beams. Energy-efficient precoding is proposed in [75, 76]. In [77] the authors propose constant-envelope precoding for satellite systems improving the robustness of the latter to the nonlinear distortions.

Particular attention is given to joint user scheduling and precoding design in [78–83]. Distributed precoding systems for multiple gateways are studied in [84]. By deploying several gateways, the available spectrum for the feeder link can be reused among spatially separated gateways through very directive antennas.

2.5 Precoding Test-beds

Precoding techniques are deployed at the transmitter side and introduce additional computational complexity on top of the existing signal preprocessing algorithms. The increased computational complexity involves defining and solving complex optimization problems at the system's symbol rate. Recent works try to address the implementation of the computational complexity of precoding techniques on actual hardware [85, 86].

The authors in [87] present a real-time mmWave (28 GHz) massive MIMO test-bed, which includes a hybrid beamforming architecture based on precoding and beam selection approaches. The presented test-bed supports up to 64 transmitting antennas with 16 active RF feeds, simultaneously serving 12 user terminals using orthogonal frequency division multiplexing (OFDM) in time-division duplex (TDD) mode.

In [88] the authors have developed an extensible test-bed, to realize a 100-antenna MIMO communication test-bed. It is built up of commercial off-the-shelf hardware, making it accessible and modifiable. Due to the heavy real-time processing requirements for massive MIMO, the test-bed uses linear precoders like MRT and ZF.

A reconfigurable real-time digital baseband MIMO channel emulator was presented in [89]. The emulator implements several transceiver impairments and a wireless correlated MIMO channel with the help of a low-complexity Rayleigh fader design. The proposed system has a rich set of emulated effects and high emulation speed to facilitate MIMO baseband transceiver development and testing.

The authors in [90] proposed a flexible FPGA-based channel emulator for non-stationary MIMO fading channels. The non-stationary channel emulator is suitable for certain propagation scenarios, such as high-speed train (HST) [91].

Solving optimization algorithms [92,93] for large-scale problems in real-time is not a trivial task and is a barrier to the implementation and demonstration of SLP techniques. Recent works focus on the complexity reduction of SLP. In [94] it is demonstrated that SLP design can be approached as ZF precoding with transmitted symbols perturbations and in [95] the authors devised a novel closed-form solution to exploit constructive interference in precoding by using a similar approach. In [96] the authors proposed another closed-form sub-optimal solution for power minimizing SLP. At the same time, the SLP technique for large-scale antenna arrays is shown in [14].

Constructive interference (CI) vector perturbation (VP) based precoding [97] offers a reduction in algorithm complexity [98]. Other closed-form solutions were developed in [95,96, 99] to further facilitate practical implementations of SLP techniques. In [100–103] the authors demonstrated the feasibility to deliver low computationally complexity of SLP techniques and implement it on actual hardware processing the baseband on a real-time basis for downlink transmission.

In [104] the authors demonstrated a 2×2 MIMO precoded real-time transmission system by using lookup tables (LUTs) for storing SLP optimized symbol mapping. While the use of the LUTs is an efficient solution for small systems with few transmitters, the large-sized LUTs are needed for s large number of transmitters and receivers in the system. The size of the LUTs increases as a function of M^N for M-th modulation order and N number of receiver terminals. In [105] a real-time satellite precoded transmission hardware demonstrator is presented, where a gateway has 6 transmitting antennas and simultaneously serves 6 user terminals with up to 32-APSK modulated signals. In this case, the required size of LUTs would be more than $6^{32} \approx 7.95 \times 10^{24}$ elements. It is inefficient to implement and handle

34

LUTs at such a scale on the transmitter side. Therefore, there is a demand for novel, low-complexity, real-time based algorithms for SLP precoders.

Chapter 3

Closed-Form Solution for M-PSK and M-APSK Symbol-Level Precoding for Power Minimization

In this chapter, we propose a precoder design for high-performance symbol processing. We derive an NNLS convex optimization problem for transmit power minimization and propose a closed-form solution to reduce the computational complexity of the technique. We benchmark the proposed closed-form algorithm against the conventional Fast NNLS [106] algorithm.

3.1 Closed-Form Symbol-Level Precoding Design

3.1.1 System Model

We consider a system model, which focuses on the forward link of a multi-beam satellite system. We assume the full frequency reuse scenario, in which all the beams transmit in the same frequency and time. The multi-user interference is mitigated by using the signal precoding technique. We define the number of transmitting antennas as N_t and the total number of users as N_u in the coverage area. In the specified MU-MIMO channel model, the received signal at the i-th user is given by $y_i = \mathbf{h}_i^\dagger \mathbf{x} + n_i$, where $\mathbf{h}_i^\dagger$ is a $1 \times N_t$ vector representing the complex channel coefficients between the i-th user and the N_t antennas of the transmitter, $\mathbf{x}$ is defined as the $N_t \times 1$ vector of the transmitted symbols at a certain symbol period and n_i is the independent complex circular symmetric (c.c.s.) independent identically distributed (i.i.d) zero mean Additive White Gaussian Noise (AWGN) measured at the i-th user's receive antenna.

Looking at the general formulation of the received signal, which includes the whole set of users, the linear signal model is

$$\mathbf{y} = \mathbf{Hx} + \mathbf{n} = \mathbf{HWs} + \mathbf{n}, \tag{3.1}$$

where $\mathbf{y} \in \mathbb{C}^{N_u \times 1}$, $\mathbf{n} \in \mathbb{C}^{N_u \times 1}$, $\mathbf{x} \in \mathbb{C}^{N_t \times 1}$, and $\mathbf{s} \in \mathbb{C}^{N_u \times 1}$ and $\mathbf{H} \in \mathbb{C}^{N_u \times N_t}$. In this scenario, we define the linear precoding matrix $\mathbf{W} \in \mathbb{C}^{N_t \times N_u}$ which maps the information symbols $\mathbf{s}$ into precoded symbols $\mathbf{x}$. We normalize the data symbols $\mathbf{s}$ to be unit variance in average over the length of a frame.

3.1.2 Optimization Problem Definition

In this section, we define an optimization problem of a computationally efficient SLP technique, which aims to minimize the sum power of the precoded symbols at the transmitter side. The technique is applicable on the M-th order phase-shift keying (M-PSK), and amplitude and phase-shift keying (M-APSK) symbol constellations. The aim is to optimally preserve constructive interference components to decrease the total transmitted power at the transmitter side. The essential difference of the SLP technique from a linear precoding method is the optimization vector $\mathbf{u} = [u_1, u_2, \ldots, u_i] \in \mathbb{C}^{N_u \times 1}$, which is recalculated for every set of symbols $\mathbf{s}$ to construct the optimized precoded signal given by

$$\mathbf{x} = \mathbf{W}(\mathbf{\Gamma} \bullet \mathbf{s} + \mathbf{u}), \tag{3.2}$$

where $\mathbf{\Gamma} = [\Gamma_1, \Gamma_2, \ldots, \Gamma_i] \in \mathbb{R}^{N_u \times 1}$ is per terminal SNR requirements. The following formulation allows us to split the problem of constructing an optimal beamforming into two independent tasks: channel orthogonalization and optimal symbol mapping for power minimization. In this scenario, we define the precoding matrix ($\mathbf{W}$) as the Zero-Forcing linear precoder:

$$\mathbf{W}_{\mathrm{ZF}} = \hat{\mathbf{H}}^{\dagger}(\hat{\mathbf{H}}\hat{\mathbf{H}}^{\dagger})^{-1}, \tag{3.3}$$

where $\hat{\mathbf{H}}$ is the channel matrix estimated from the channel state information (CSI). We choose ZF for its properties to orthogonalize the channel so that in the case of $\hat{\mathbf{H}} = \mathbf{H}$ the received symbols are a summation of the transmitted symbols, the optimization vector, and Gaussian noise:

$$\mathbf{y} = \mathbf{H}\mathbf{W}_{\mathrm{ZF}}(\mathbf{\Gamma} \bullet \mathbf{s} + \mathbf{u}) + \mathbf{n} = \mathbf{\Gamma} \bullet \mathbf{s} + \mathbf{u} + \mathbf{n}. \tag{3.4}$$

ZF is not an optimal precoder in a sense of energy efficiency and there are more efficient techniques in the literature [107], which provide better power and BER performance on a frame basis. By using the ZF precoding matrix we guarantee to meet the SNR constraints in the design of SLP and simplify the precoder. The optimal symbol mapping we derive in the following paragraphs.
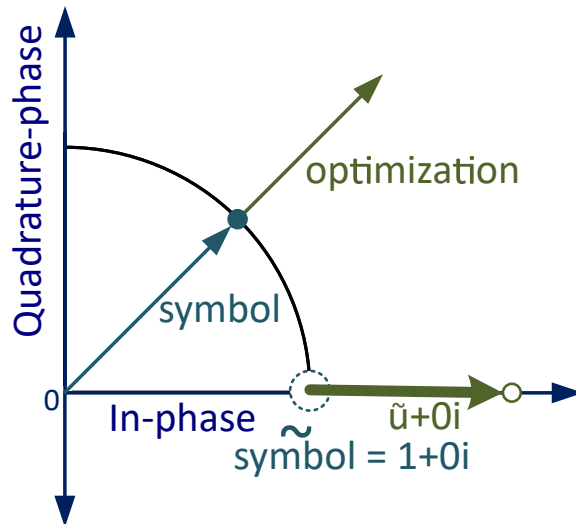
FIGURE 3.1: Symbol optimization of the proposed SLP.

In Fig. 3.1 we generalize the effect of the optimization u_i on a single complex data symbol s_i with unit power. The optimization vector increases the absolute magnitude of the symbol and keeps its phase in a fixed direction. In a case of the multi-ring constellation we consider, that power of the symbols, which are mapped to the external ring, is $|s_i| \geq 1$. All the symbols on the internal rings with power $|s_i| < 1$ retain their original position.

To avoid operations with complex numbers in the optimization problem we reformulate the input data to real-defined values and keep the rest of the optimization problem relevant. We replace the complex data symbols with equivalent symbols $\tilde{\mathbf{s}} \in \mathbb{R}^{N_u}$, where $\tilde{s}_i = 1 + \iota 0$ for every $i = 1, 2, \ldots, N_u$, by introducing the following transformation

$$\mathbf{\Gamma} \bullet \mathbf{s} = \mathbf{B}\tilde{\mathbf{s}}, \tag{3.5}$$

where $\mathbf{B}$ is a diagonal matrix, where elements of the vector $\mathbf{\Gamma} \bullet \mathbf{s}$ are its diagonal elements such as:

$$\mathbf{B} = \begin{bmatrix} \Gamma_1 s_1 & 0 & 0 & \ldots & 0 \\ 0 & \Gamma_2 s_2 & 0 & \ldots & 0 \\ 0 & 0 & \Gamma_3 s_3 & \ldots & 0 \\ \vdots & \vdots & \vdots & \ddots & \vdots \\ 0 & \ldots & 0 & 0 & \Gamma_i s_i \end{bmatrix}. \tag{3.6}$$

We also replace the optimization vector $\mathbf{u}$ with a new real-defined vector $\tilde{\mathbf{u}} = [\tilde{u}_1, \tilde{u}_2, \ldots, \tilde{u}_i] \in \mathbb{R}_{\geq 0}^{N_u \times 1}$ and rewrite the equation (3.2) as

$$\mathbf{x} = \mathbf{W}_{\text{ZF}} \mathbf{B}(\tilde{\mathbf{s}} + \tilde{\mathbf{u}}). \tag{3.7}$$

The new vector optimization $\tilde{\mathbf{u}}$ can only acquire zero or positive real values, which accommodates the objective to increase the absolute magnitude and keep the phase fixed of the data symbols received by the terminals while pushing the sum power of the transmitted precoded symbols to its minimum.

In the case of a single-ring M-PSK constellation, we define the optimization problem to minimize the sum power of the precoded symbols vector $\mathbf{x}$ as

$$\begin{aligned} \min_{\tilde{\mathbf{u}}} \quad & \|\mathbf{x}\|_2 \\ \text{s. t.} \quad & \tilde{u}_i \geq 0, \end{aligned} \tag{3.8}$$

for all $i = 1, 2, \ldots, N_u$.

By substituting (3.7) in (3.8) we get

$$\begin{aligned} \min_{\tilde{\mathbf{u}}} \quad & \|\mathbf{A}\tilde{\mathbf{u}} - \mathbf{d}\|_2 \\ \text{s. t.} \quad & \tilde{u}_i \geq 0, \end{aligned} \tag{3.9}$$

where $\mathbf{A} = \mathbf{W}_{\text{ZF}} \mathbf{B}$ and $\mathbf{d} = -\mathbf{W}_{\text{ZF}} \mathbf{B}\tilde{\mathbf{s}}$. Finally, we transform the objective function in (3.9) from the complex domain to the real domain. In this case, we apply the equality between the Euclidean norm of a complex vector $\tilde{z} = [\tilde{z}_1, \tilde{z}_2, \ldots, \tilde{z}_i]$ and a real vector $z = [z_1, z_2, \ldots, z_i]$, where $\tilde{z}_i = a_i + \iota b_i$ and $z_i = [a_i, b_i]$, to rewrite (3.9) as

$$\begin{aligned} \min_{\tilde{\mathbf{u}}} \quad & \|\widetilde{\mathbf{A}}\tilde{\mathbf{u}} - \tilde{\mathbf{d}}\|_2 \\ \text{s. t.} \quad & \tilde{u}_i \geq 0, \end{aligned} \tag{3.10}$$

where $\widetilde{\mathbf{A}} = [\mathrm{Re}(\mathbf{A}); \mathrm{Im}(\mathbf{A})] \in \mathbb{R}^{2N_t \times N_u}$ and $\tilde{\mathbf{d}} = [\mathrm{Re}(\mathbf{d}^\dagger), \mathrm{Im}(\mathbf{d}^\dagger)]^\dagger$.

In a case where the symbols generated from multi-ring M-APSK constellations, we need to fix the symbols on the internal rings ($\tilde{u}_i = 0$) and optimize the symbols only on the external ring by increasing their absolute magnitude ($\tilde{u}_i \geq 0$). For this, we define the optimization problem by constraining the external and internal symbols separately as:

$$
\begin{aligned}
\min_{\tilde{\mathbf{u}}} \quad & \|\mathbf{x}\|_2 \\
\text{s. t.} \quad & \tilde{u}_i \geq 0, |s_i| \geq 1, \\
& \tilde{u}_i = 0, |s_i| < 1.
\end{aligned}
\tag{3.11}
$$

We follow the same derivation steps as in the case of M-PSK constellations and get the following optimization expression:

$$
\begin{aligned}
\min_{\tilde{\mathbf{u}}} \quad & \|\widetilde{\mathbf{A}}\tilde{\mathbf{u}} - \tilde{\mathbf{d}}\|_2 \\
\text{s. t.} \quad & \tilde{u}_i \geq 0, |s_i| \geq 1, \\
& \tilde{u}_i = 0, |s_i| < 1.
\end{aligned}
\tag{3.12}
$$

We can see that the problem (3.10) is a subset of the more general problem formulation (3.12).

The problem (3.10) is a NNLS optimization problem. It can be solved in different ways found in the literature [106, 108]. The problem (3.12) can be solved by using CVX [109, 110]. After the optimization vector $\tilde{\mathbf{u}}$ is found, the gateway constructs the precoded signal using the equation (3.7). If the optimal solution is not found, then all the elements of $\tilde{\mathbf{u}}$ are equal to zero. In this case, the SLP technique is equivalent to the conventional ZF precoding technique

$$
\mathbf{x} = \mathbf{W}_{\mathrm{ZF}}\mathbf{B}(\tilde{\mathbf{s}} + \tilde{\mathbf{u}}^{0}) = \mathbf{W}_{\mathrm{ZF}}(\mathbf{\Gamma} \bullet \mathbf{s}).
\tag{3.13}
$$

Thus, in the worst case scenario the proposed SLP technique performs the same as the ZF precoding in terms of energy efficiency and sum power rate.

3.1.3 Complexity Analysis of the SLP design and the Fast NNLS Algorithm

The computationally efficient SLP design, as described in the previous section, shares the same operations as the ZF technique. For the MU-MIMO system with an equal number of the transmitting and receiving antennas $N_t = N_u = N$, the asymptotic computational complexity of the inversion of the channel matrix $\mathbf{H}$ is $O(N^3)$. The matrix inverse is calculated once per symbol frame. The asymptotic complexity of the multiplication between the channel precoding matrix $\mathbf{W}$ and the vector of symbols $\mathbf{s}$ is $O(N^2)$. The multiplication is performed per each set of symbols in the frame.

The most computationally demanding part of the SLP design is the Fast NNLS and CVX algorithms, which solve the sum power minimization problems (3.10) and (3.12). The algorithm is repeated per every set of transmitted symbols. Hereby we do not provide the exact asymptotic complexity of the CVX algorithm, as it contains several embedded solvers to handle different types of convex problems. On the other hand, the most computationally complex operation of the Fast NNLS algorithm [106, 108] is solving the unconstrained linear least-squares sub-problems by using the QR decomposition. The asymptotic complexity of the QR decomposition is of $O(N^3)$. However, in [111] the authors propose a method to reduce considerably the level of complexity of the QR decomposition up to $O(N^2)$.

3.1.4 Closed-Form Algorithm (CF NNLS SLP)

In this section, we propose a closed-form algorithm (CF NNLS SLP), which do not use the QR decomposition to efficiently solve the optimization problem (3.10) and (3.12) for M-PSK and M-APSK symbols. The Fast NNLS algorithm [106] finds the optimal regression coefficients $\tilde{\mathbf{u}}$ by iteratively updating and solving the active subset P of the quadratic equations as

$$\tilde{\mathbf{u}} = (\widetilde{\mathbf{A}}^\dagger \widetilde{\mathbf{A}})^{-1} \widetilde{\mathbf{A}}^\dagger \tilde{\mathbf{d}}. \tag{3.14}$$

For the Fast NNLS algorithm to converge the number of iteration is not fixed and can reach up to N_u. In every iteration the equation (3.14) is partially solved thought the QR decomposition.

We propose to substantially relax the complexity of the optimization problem by the assumption that the regression coefficients are mutually uncorrelated. In this case, the off-diagonal elements of the matrix product $(\widetilde{\mathbf{A}}^\dagger \widetilde{\mathbf{A}})$ are equal to zero as

$$\widetilde{\mathbf{A}}^\dagger \widetilde{\mathbf{A}} \approx \begin{bmatrix} \sum_{j=1}^{2N_t} \widetilde{A}_{j,1}^2 & \cdots & 0 \\ \vdots & \ddots & \vdots \\ 0 & \cdots & \sum_{j=1}^{2N_t} \widetilde{A}_{j,N_u}^2 \end{bmatrix}. \tag{3.15}$$

By inserting (3.15) into (3.14) we derive an approximate closed-form solution for the optimization problem (3.10) as

$$\tilde{u}_i = \frac{1}{\sum_{j=1}^{2N_t} \widetilde{A}_{j,i}^2} \sum_{j=1}^{2N_t} \widetilde{A}_{j,i} \tilde{d}_j \geq 0, \tag{3.16}$$

for each element i of the vector $\tilde{\mathbf{u}}$. The solution of the equation (3.16) must be equal or greater than zero and cannot take negative values.

In order to solve (3.12) we extend (3.16) to differentiate symbols from external and internal constellation rings as

$$\tilde{u}_i = \begin{cases} \frac{1}{\sum_{j=1}^{2N_t} \widetilde{A}_{j,i}^2} \sum_{j=1}^{2N_t} \widetilde{A}_{j,i} \tilde{d}_j \geq 0 & , |s_i| \geq 1 \\ 0 & , |s_i| < 1. \end{cases} \tag{3.17}$$

In the extended expression, the solution must be equal to zero for every symbol in the internal ring $|s_i| < 1$. In this case, the internal constellation symbols are fixed to their original position. The (3.17) can be also applied to solve the problem (3.10), thus it is a complete solution for any type of PSK and APSK constellations.

The approximate solution (3.17) is solved and considered as converged in a single iteration contrary to the Fast NNLS. The asymptotic complexity of the equation 3.17 is of $O(N^2)$. This is a considerably lower complexity level than the one of the Fast NNLS algorithm, which can use the QR decomposition multiple times in a single optimization problem.

Obviously, the solution provided in equation (3.16) is not optimal and the calculation error of the optimization will increase following the expansion of the dimensions of the matrix $\widetilde{\mathbf{A}}$ as will be demonstrated in the following section of this chapter. We propose to minimize the calculation error by introducing a scale factor ρ as follows:

$$\mathbf{x} = \mathbf{W}_{\text{ZF}} \mathbf{B}(\tilde{\mathbf{s}} + \rho \tilde{\mathbf{u}}). \tag{3.18}$$

The scale factor ρ can be heuristically estimated ranging its values from 1, when the error is not significant, towards 0 as the error increases.

3.2 Theoretical Validation

We demonstrate the feasibility of the proposed SLP technique and compare the performances between the Fast NNLS (denoted as NNLS SLP) algorithm and the closed-form solution (denoted as CF NNLS SLP). Also, we benchmark the SLP techniques against the conventional ZF (3.13) and MMSE precoders defined as

$$\mathbf{W}_{\text{MMSE}} = \hat{\mathbf{H}}^H \cdot (\hat{\mathbf{H}} \cdot \hat{\mathbf{H}}^H + \sigma^2 \mathbf{I})^{-1}, \tag{3.19}$$

where σ^2 is the AWGN noise variance in the I/Q components combined and $\mathcal{I} \in \mathbb{R}^{N_u \times N_u}$ is an identity matrix. The precoded signals are constructed accordingly as follows

$$\mathbf{x}_{\text{ZF}} = \mathbf{W}_{\text{ZF}} \mathbf{s}, \tag{3.20}$$

$$\mathbf{x}_{\text{MMSE}} = \mathbf{W}_{\text{MMSE}} \mathbf{s}. \tag{3.21}$$

In the numerical validation, we consider a MU-MIMO system, which has an equal number of the transmit and receive antennas $N_t = N_u = N$. We accordingly generate a full rank $N \times N$ MIMO channel matrix with a 2-norm matrix condition number defined as

$$\kappa_2(\mathbf{H}) = ||\mathbf{H}||_2 \cdot ||\mathbf{H^{-1}}||_2. \tag{3.22}$$

The matrix condition number corresponds to the ratio of the largest singular value of that matrix to smallest singular value of the matrix. In the case of the MU-MIMO system, the matrix condition number describes the power imbalance in the channel [101]. We average the results over 500 channel matrices.

3.2.1 Averaged Sum Power Benchmark

In this benchmark, we evaluate the averaged sum power of the precoded signal designed using ZF and the proposed SLP techniques - NNLS SLP and CF NNLS SLP. We plot the sum power over the number of the transmit and receive antennas N in Fig. 3.2. All the benchmarks are normalized to the power of the ZF technique, thus ZF benchmark is at 0 dB. We can see that both NNLS SLP and CF NNLS SLP approaches construct the precoded signal at the lower power than the ZF technique. The higher the channel rank, the lower the sum power of the precoded signal is needed to transmit the precoded signal. We observe that the performance of the CF NNLS SLP algorithm does not reach the performance of the NNNLS SLP for $N \geq 5$. The optimization solution of the unscaled CF NNLS SLP becomes unfeasible around the point $N = 13$. The number of the off-diagonal elements of the channel matrix increases exponentially as the matrix size is increasing. Contrary, the number of the diagonal elements has a linear dependency. Accordingly, the sum power of the off-diagonal elements of the matrix product $(\widetilde{\mathbf{A}}^T \widetilde{\mathbf{A}})$ increases faster than the power of the diagonal elements. At a certain point, the sum power of the off-diagonal elements exceeds the sum power of the diagonal elements. As a result, the optimization problem (3.10) error is too large as in this case the off-diagonal elements have a strong influence and must be accounted for designing the regression coefficients. The scaled CF NNLS SLP solution on the other hand minimizes the error and can perform even in the large dimension systems. The scaling parameter ρ was selected heuristically and is equal to 1 for $N = 2 \ldots 6$, ρ is equal to 0.5 for $N = 7 \ldots 14$, and ρ is equal to 0.33 for $N = 15 \ldots 20$.

In Fig. 3.3 we generate variable size channel matrix while keeping its condition number fixed. Although the rank of the channel matrix is increasing, the major sum power will be

FIGURE 3.2: Averaged sum power in different channel realizations for conventional ZF, NNLS SLP and CF NNLS SLP. The number of transmitters is equal to number of the receivers ($N_t = N_u = N$). The 2-norm condition number is a function of $3N$.

concentrated in the diagonal elements for any channel dimensions. We can see that in this channel scenario both optimization algorithms perform identically. The closed-form algorithm even without the scaling remains very close to the optimal solution in the benchmark.

The numerical results show that the mutual correlation between the regression coefficients in the convex optimization problems (3.10) can be neglected for certain MIMO channel scenarios. By using the proposed closed-form algorithm, we can improve the power efficiency of the MIMO system and considerably reduce the complexity of the precoder. The letter is important when implementing the SLP technique on the actual hardware for the in-lab demonstration.

3.2.2 Computation Time Benchmark

The following benchmark shows the processing time per set of N precoded symbols averaged over duration of a frame. The benchmark was performed in the MATLAB R2018b environment using general-purpose central processing unit. Here we do not how separated results for the CF NNLS SLP with the scaling and without it. To disable scaling, we set $\rho = 1$ for every N, therefore the algorithm is the same in both cases. Fig. 3.4 shows the time evaluation required to process the equation (3.20) for ZF, the equation 3.17 for CF NNLS SLP, and the Fast NNLS algorithm of [108] for NNLS SLP.

We observe that the ZF and CF NNLS SLP algorithms perform at the fastest time for any given size of the MIMO system. The processing time of the closed-form algorithm CF NNLS SLP is significantly improved over the benchmark of the Fast NNLS algorithm. By using the CF NNLS SLP algorithm, the transmitter can efficiently construct the precoded symbols with the symbol-level approach. The reduced processing time is an important step towards the in-lab implementation of the SLP technique applicable to the real-time high-throughput satellite communications.
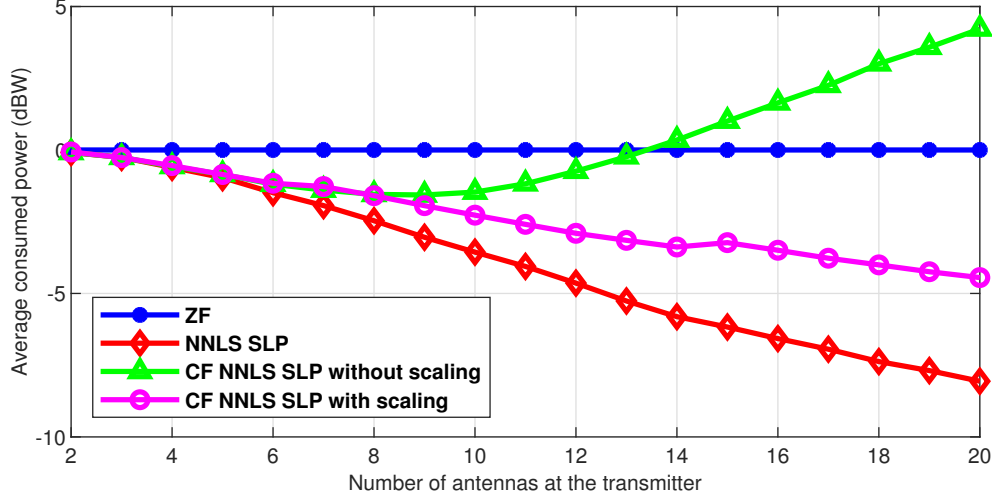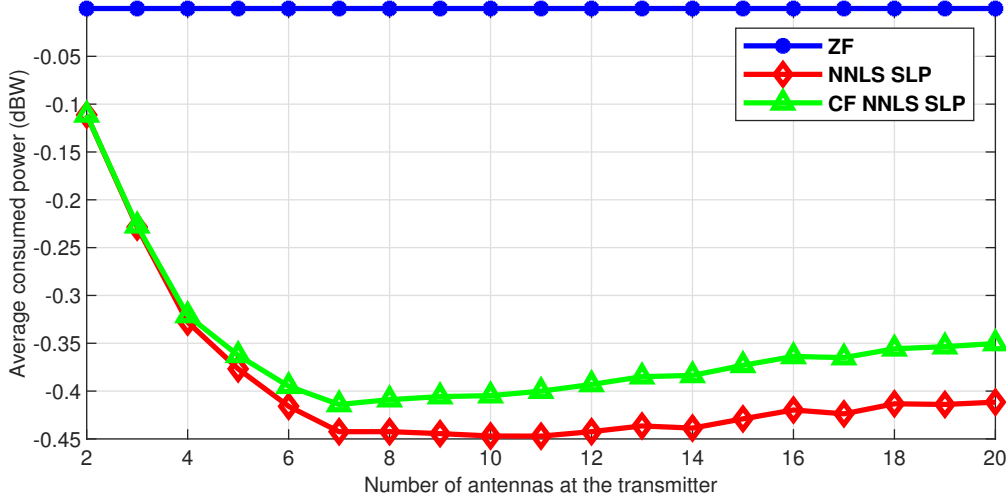
FIGURE 3.3: Averaged sum power in different channel realizations for conventional ZF, NNLS SLP and CF NNLS SLP. The number of transmitters is equal to number of the receivers ($N_t = N_u = N$). The 2-norm condition number is equal 8 and fixed for every N.

3.2.3 Energy Efficiency Benchmark

We evaluate the energy efficiency of the MIMO system using the proposed SLP technique and compare the performance between the Fast NNLS (NNLS SLP) algorithm and the closed-form algorithm (CF NNLS SLP). The energy efficiency is defined as

$$\text{EE}(E_b/N_0) = \frac{(1 - \text{BER}(E_b/N_0))}{J_N N}, \tag{3.23}$$

where J_N is the average sum power of the precoded signals for the channel size N and $E_b/N_0 = 10 \log_{10}(\frac{1}{\log_2(M)\sigma^2})$ is the energy per bit to noise power spectral density ratio for the $M = 8$ PSK constellations.

The proposed SLP technique pushes the data symbols deeper into the detection region by exploiting the constructive inter-user interference. Fig. 3.5 shows an example of received 8-PSK constellation optimized by the proposed SLP algorithm. The excursion in the symbols results in an improved averaged E_b/N_0 ratio over the whole frame of symbols, although the instantaneous E_b/N_0 ratio of some symbols does not improve in relation to the ZF technique.

The E_b/N_0 is set by adding AWGN to the received signal as in (3.1). The demodulator is considered to have a perfect phase alignment and errors in the symbols appear solely due to the injected noise. Fig. 3.6 shows the energy efficiency of the theoretical 8-PSK curve, and of ZF, MMSE, NNLS SLP and CF NNLS SLP algorithms averaged over the channel matrix with conditioning number set to 24. The theoretical $\widehat{\text{BER}}$ for 8-PSK is obtained using equation 8.22 in [112]:

$$\widehat{\text{BER}}(E_b/N_0) = \frac{1}{\pi} \int_0^{(M-1)\pi/M} \exp\left(-(E_b/N_0)\frac{\sin^2(\pi/M)}{\sin^2(\theta)}\right) d\theta. \tag{3.24}$$

It was shown in [112] that the upper bound of the integral in (3.24) is:

$$\widehat{\text{BER}}(E_b/N_0) = \frac{M-1}{M} \exp\left(-(E_b/N_0)\sin^2(\frac{\pi}{M})\right). \tag{3.25}$$
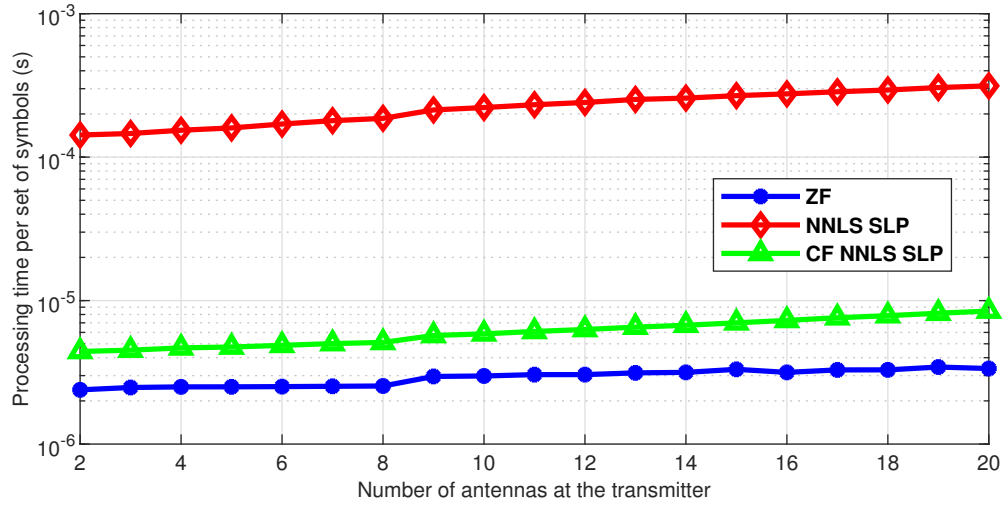
FIGURE 3.4: Averaged processing time of ZF, NNLS SLP and CF NNLS SLP algorithms.
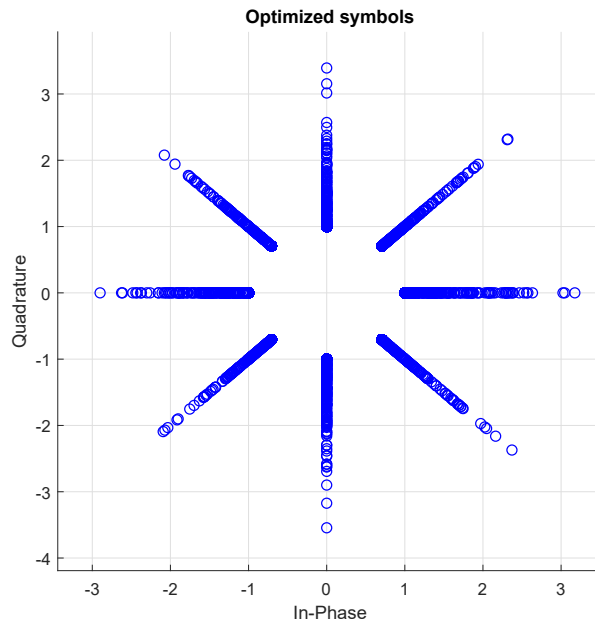
FIGURE 3.5: Received symbols modified by CF NNLS SLP.

43
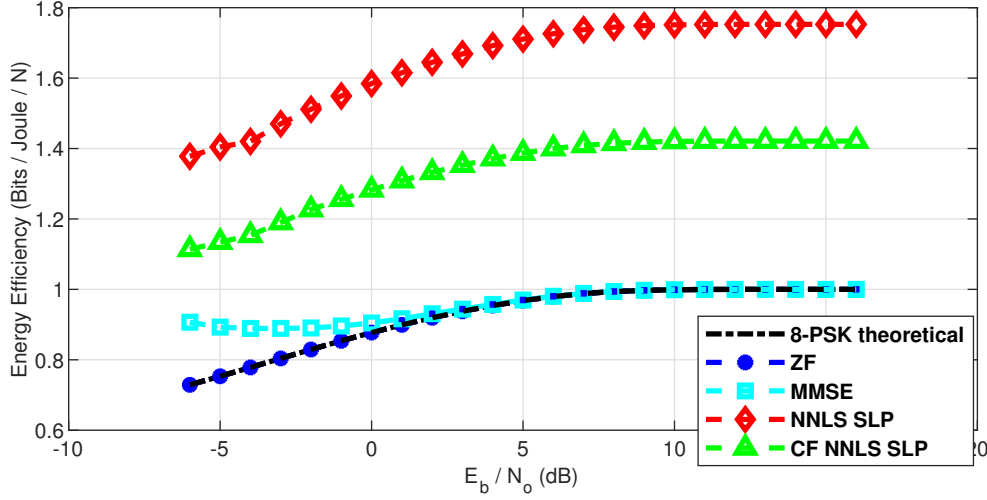
FIGURE 3.6: Energy Efficiency curves for ZF, MMSE, NNLS SLP and CF NNLS SLP compared to the theoretical 8-PSK baseline. The matrix condition for the precoded channel is 24 and $N = 8$.

We can see from Fig. 3.6 that the proposed SLP technique significantly improved the energy efficiency of the system. The higher energy efficiency of the proposed SLP technique is achieved when using the Fast NNLS algorithm. The proposed CF NNLS SLP algorithm also improves the energy efficiency of the system compared to the ZF and MMSE techniques.

3.3 Summary

In this chapter, we presented the computationally and energy-efficient SLP for sum power minimization, where the constellation symbols are optimized in a fixed-phase direction. By using the fixed-phase symbol optimization, we further reduce the computational complexity of the precoding at the transmitter. We demonstrated the efficiency of the precoder design using the Fast NNLS algorithm and the proposed closed-form algorithm for solving the convex optimization problem. The numerical validation shows that the performance of the closed-form algorithm is nearly the same as the performance of the Fast NNLS algorithm in terms of optimization quality for certain MIMO channel matrices. The closed-form algorithm has an asymptotic complexity of $O(N^2)$ and has a significantly shorter processing time in comparison to the Fast NNLS algorithm. The CF NNLS algorithm results in the increased sum power of the precoded signal when compared to the Fast NNLS algorithm. On the other hand, the closed-form algorithm provides a trade-off between the increased sum power and much faster processing time. The efficient processing time and low complexity of the algorithm are essential in the real-time transmission systems with very short symbol periods (DVB-S2, Millimeter-wave communications).

Chapter 4

Closed-Form Solution for M-QAM Symbol-Level Precoding for Power Minimization

In this chapter, we focus on terrestrial communication through a MU-MIMO channel. We derive an energy and computationally efficient symbol-level precoding to minimize the sum power of the transmitted signal while maintaining the minimal required SNR threshold at the receiver terminals. The SLP technique is based on a non-negative convex quadratic optimization problem. We improve the technique to support the optimization of M-th order QAM constellations in the relaxed-phase region.

4.1 Symbol-Level Precoding Design

4.1.1 System Model

We consider a system model with the forward link of a multi-user multi-antenna terrestrial communication system. We assume the system to use the full frequency reuse scenario, in which all the antennas transmit in the same frequency and time. The multi-user interference is managed using precoding. We define the number of transmitting antenna as N_t and the total number of receiver terminals as N_u in the coverage area. In the specified MU-MIMO channel model, the received signal at the i-th terminal is given by $y_i = \mathbf{h}_i^\dagger \mathbf{x} + n_i$, where $\mathbf{h}_i^\dagger$ is a $1 \times N_t$ vector representing the complex channel coefficients between the i-th terminal and the N_t antennas of the transmitter, $\mathbf{x}$ is defined as the $N_t \times 1$ vector of the transmitted symbols at a certain symbol period and n_i is the independent complex circular symmetric (c.c.s.) independent identically distributed (i.i.d) zero mean Additive White Gaussian Noise (AWGN) measured at the i-th terminal's receive antenna.

Looking at the concatenated formulation of the received signal, which includes the whole set of receiver terminals, the linear signal model is

$$\mathbf{y} = \mathbf{H}\mathbf{x} + \mathbf{n} = \mathbf{H}\mathbf{W}\mathbf{s} + \mathbf{n}, \tag{4.1}$$

where $\mathbf{y} = [y_1, y_2, \ldots, y_i] \in \mathbb{C}^{N_u \times 1}$, $\mathbf{n} = [n_1, n_2, \ldots, n_i] \in \mathbb{C}^{N_u \times 1}$, $\mathbf{x} \in \mathbb{C}^{N_t \times 1}$, and $\mathbf{s} \in \mathbb{C}^{N_u \times 1}$ and $\mathbf{H} = [\mathbf{h}_i^\dagger, \mathbf{h}_i^\dagger, \ldots, \mathbf{h}_i^\dagger] \in \mathbb{C}^{N_u \times N_t}$. In this scenario, we define a precoding matrix $\mathbf{W} \in$

$\mathbb{C}^{N_t \times N_u}$ which maps the information symbols $\mathbf{s}$ into precoded symbols $\mathbf{x}$. We consider the data symbols $\mathbf{s}$ to be unit variance complex vectors $|s_i| = 1$ for every $i = 1, 2, \ldots, N_u$.

4.1.2 Symbol-Level Precoding Design

In this section, we define an optimization problem of the computationally efficient SLP technique, which aims to minimize the sum power of the precoded symbols at the gateway side. The technique is applicable to the M-th order quadrature amplitude modulation (M-QAM). It reduces the sum power of the precoded symbols at the transmitter side by exploiting constructive interference components at the receiver side. To achieve this, the SLP technique needs to recalculate a perturbation vector $\mathbf{u} = [u_1, u_2, \ldots, u_i] \in \mathbb{C}^{N_u \times 1}$ for a set of symbols $\mathbf{s}$ in every transmission time frame to construct the optimized precoded signal given by

$$\mathbf{x} = \mathbf{W}\boldsymbol{\Gamma}(\mathbf{s} + \mathbf{u}), \tag{4.2}$$

where $\boldsymbol{\Gamma}$ is per terminal minimal SNR requirements defined as

$$\boldsymbol{\Gamma} = \mathbf{diag}\begin{bmatrix} \Gamma_1, & \Gamma_2, & \ldots, & \Gamma_i \end{bmatrix}. \tag{4.3}$$

In the following formulation, we split the problem of constructing optimal beamforming vectors into two independent tasks: channel orthogonalization and optimal symbol mapping for energy efficiency. In this case, we define the precoding matrix ($\mathbf{W}$) as the Zero-Forcing linear precoder:

$$\mathbf{W}_{\mathrm{ZF}} = \hat{\mathbf{H}}^H(\hat{\mathbf{H}}\hat{\mathbf{H}}^H)^{-1}, \tag{4.4}$$

where $\hat{\mathbf{H}}$ is the channel matrix estimated from the channel state information (CSI). We choose ZF for its properties to orthogonalize the channel so that in the case of $\hat{\mathbf{H}} = \mathbf{H}$ the SNRs of the received symbols are linearly related to the $\boldsymbol{\Gamma}$ applied on the transmitted symbols, the perturbation vector ($\mathbf{u}$) and the Gaussian noise ($\mathbf{n}$):

$$\mathbf{y} = \mathbf{H}\mathbf{W}_{\mathrm{ZF}}\boldsymbol{\Gamma}(\mathbf{s} + \mathbf{u}) + \mathbf{n} = \boldsymbol{\Gamma}\mathbf{s} + \boldsymbol{\Gamma}\mathbf{u} + \mathbf{n}. \tag{4.5}$$

Thought, ZF is not an optimal precoder in a sense of energy efficiency and there are more efficient techniques in the literature [107], which provide better performance on a frame basis. The proposed SLP approach will build upon the ZF precoder and will improve the energy efficiency by optimizing every transmitted set of symbols. The optimal symbol mapping we derive in the following paragraphs.

In Fig. 4.1 we show the effect of the perturbation u_i on a complex data symbol s_i depending on its location in the M-QAM constellation. The perturbation vector has to increase the absolute magnitude of the symbol and preserve detection regions. We consider that all the symbols are mapped in the first quadrature of the complex plane by transforming the actual complex data symbols with the equivalent symbols $\tilde{\mathbf{s}} \in \mathbb{C}^{N_u \times 1}$, where $\tilde{s}_i = b_i s_i$, $\mathrm{Re}(\tilde{s}_i) \geq 0$ and $\mathrm{Im}(\tilde{s}_i) \geq 0$ for every $i = 1, 2, \ldots, N_u$. The variable b_i represents the rotation of the symbol vectors into the first quadrature of the complex plane and is defined as

$$b_i = \begin{cases} 1 & \text{if } \mathrm{Re}(s_i) > 0 \text{ and } \mathrm{Im}(s_i) > 0 \\ -\iota 1 & \text{if } \mathrm{Re}(s_i) < 0 \text{ and } \mathrm{Im}(s_i) > 0 \\ \iota 1 & \text{if } \mathrm{Re}(s_i) > 0 \text{ and } \mathrm{Im}(s_i) < 0 \\ -1 & \text{if } \mathrm{Re}(s_i) < 0 \text{ and } \mathrm{Im}(s_i) < 0 \end{cases}, \tag{4.6}$$
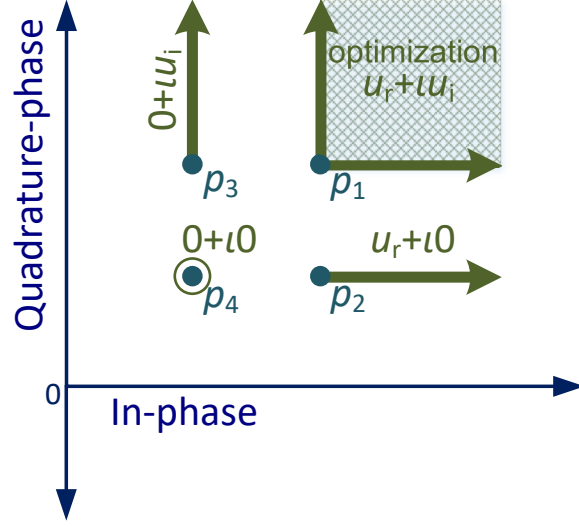
FIGURE 4.1: 16-QAM constellation optimized by CF SLP algorithm.

TABLE 4.1: Properties of perturbation vector based on symbol position.

Position	$\mathrm{Re}(\tilde{s}_i)$	$\mathrm{Im}(\tilde{s}_i)$	$\mathrm{Re}(u_i)$	$\mathrm{Im}(u_i)$
p_1	≥ 1	≥ 1	≥ 0	≥ 0
p_2	≥ 1	< 1	≥ 0	$= 0$
p_3	< 1	≥ 1	$= 0$	≥ 0
p_4	< 1	< 1	$= 0$	$= 0$

for $i = 1, 2, \ldots, N_u$. The following equality is therefore respected

$$\mathbf{s} = \mathbf{B}\tilde{\mathbf{s}}, \tag{4.7}$$

where $\mathbf{B}$ is a diagonal matrix, where the rotation vectors b_i are its diagonal elements such as:

$$\mathbf{B} = \mathbf{diag}\begin{bmatrix} b_1, & b_2, & b_3, & \ldots, & b_i \end{bmatrix}. \tag{4.8}$$

We identify 4 generalized positions of a symbol on the complex plain regardless of the modulation order M considered and summarize the constraints on the perturbation vector based on the position of a symbol in Table 4.1. We replace the perturbation vector $\mathbf{u}$ with a new vector $\tilde{\mathbf{u}} = [\tilde{u}_1, \tilde{u}_2, \ldots, \tilde{u}_i] \in \mathbb{C}^{N_u \times 1}$, where $\mathrm{Re}(\tilde{u}_i) \geq 0$ and $\mathrm{Im}(\tilde{u}_i) \geq 0$ for every $i = 1, 2, \ldots, N_u$. Finally, we rewrite the equation (4.2) as

$$\mathbf{x} = \mathbf{W}_{\mathrm{ZF}}\mathbf{\Gamma}\mathbf{B}(\tilde{\mathbf{s}} + \tilde{\mathbf{u}}). \tag{4.9}$$

We define the optimization problem to minimize the sum power of the precoded symbols

vector $\mathbf{x}$ for any M-QAM constellation as

$$
\begin{aligned}
\min_{\tilde{\mathbf{u}}} \quad & \|\mathbf{x}\|_2 \\
\text{s. t.} \quad & C1: \begin{cases} \mathrm{Re}(\tilde{u}_i) \geq 0 \\ \mathrm{Im}(\tilde{u}_i) \geq 0 \end{cases}, \quad \tilde{s}_i \in p_1. \\
& C2: \begin{cases} \mathrm{Re}(\tilde{u}_i) \geq 0 \\ \mathrm{Im}(\tilde{u}_i) = 0 \end{cases}, \quad \tilde{s}_i \in p_2. \\
& C3: \begin{cases} \mathrm{Re}(\tilde{u}_i) = 0 \\ \mathrm{Im}(\tilde{u}_i) \geq 0 \end{cases}, \quad \tilde{s}_i \in p_3. \\
& C4: \begin{cases} \mathrm{Re}(\tilde{u}_i) = 0 \\ \mathrm{Im}(\tilde{u}_i) = 0 \end{cases}, \quad \tilde{s}_i \in p_4,
\end{aligned}
\tag{4.10}
$$

for all $i = 1, 2, \ldots, N_u$.

By substituting (4.9) in (4.10) and by applying an equality between the Euclidean norm of a complex vector $\tilde{z} = [\tilde{z}_1, \tilde{z}_2, \ldots, \tilde{z}_i]$ and a real vector $z = [z_1, z_2, \ldots, z_i]$, where $\tilde{z}_i = a_i + \iota b_i$ and $z_i = [a_i, b_i]$, we get

$$
\begin{aligned}
\min_{\hat{\mathbf{u}}} \quad & \|\widehat{\mathbf{A}}\hat{\mathbf{u}} - \hat{\mathbf{d}}\|_2 \\
\text{s. t.} \quad & C1: \begin{cases} \hat{u}_i \geq 0 \\ \hat{u}_{i+N_u} \geq 0 \end{cases}, \quad \tilde{s}_i \in p_1. \\
& C2: \begin{cases} \hat{u}_i \geq 0 \\ \hat{u}_{i+N_u} = 0 \end{cases}, \quad \tilde{s}_i \in p_2. \\
& C3: \begin{cases} \hat{u}_i = 0 \\ \hat{u}_{i+N_u} \geq 0 \end{cases}, \quad \tilde{s}_i \in p_3. \\
& C4: \begin{cases} \hat{u}_i = 0 \\ \hat{u}_{i+N_u} = 0 \end{cases}, \quad \tilde{s}_i \in p_4,
\end{aligned}
\tag{4.11}
$$

where $\widehat{\mathbf{A}} = [\mathrm{Re}(\mathbf{A}), -\mathrm{Im}(\mathbf{A}); \mathrm{Im}(\mathbf{A}), \mathrm{Re}(\mathbf{A})] \in \mathbb{R}^{2N_t \times 2N_u}$, $\hat{\mathbf{d}} = [\mathrm{Re}(\mathbf{d}^\dagger), \mathrm{Im}(\mathbf{d}^\dagger)]^\dagger \in \mathbb{R}^{2N_t \times 1}$, $\hat{\mathbf{u}} = [\mathrm{Re}(\tilde{\mathbf{u}}^\dagger), \mathrm{Im}(\tilde{\mathbf{u}}^\dagger)]^\dagger \in \mathbb{R}^{2N_u \times 1}$, $\mathbf{A} = \mathbf{W}_{\mathrm{ZF}}\mathbf{\Gamma}\mathbf{B}$, and $\mathbf{d} = -\mathbf{W}_{\mathrm{ZF}}\mathbf{\Gamma}\mathbf{B}\tilde{\mathbf{s}}$. In general, the optimization problem (4.11) can be solved using CVX tools for MATLAB [109, 110]. In the next section, we propose a closed-form algorithm to solve the problem with a fixed number of iterations.

4.1.3 Closed-Form Algorithm (CF SLP)

In this section we derive the closed-form solution (CF SLP) to solve the optimization problem (4.11) for M-QAM symbols. In the beginning, we solve the problem only for the constraint $C1$ and later expand the solution to deal with the constraints $C1, C2, C3$ and $C4$ jointly. The optimization problem (4.11) with the constraint $C1$ has a form of a non-negative least squares (NNLS) problem. It can be solved using iterative Fast NNLS algorithm [106, 108].

The conventional Fast NNLS algorithm finds the optimal regression coefficients through a number of iteration. In every iteration, it dynamically chooses and solves a subset of quadratic equations from a complete set defined as

$$\hat{\mathbf{u}} = (\widehat{\mathbf{A}}^\dagger \widehat{\mathbf{A}})^{-1} \widehat{\mathbf{A}}^\dagger \widehat{\mathbf{d}}. \tag{4.12}$$

For the Fast NNLS algorithm to converge the number of iteration is not fixed and can reach up to N_u. In every iteration, the equation (4.12) is solved by using the QR decomposition, which asymptotic complexity alone is of $O(N_t \times N_u^2)$.

We propose to substantially relax the complexity of the optimization problem by the assumption that the regression coefficients are mutually uncorrelated. In this case, the off-diagonal elements of the matrix product $(\widehat{\mathbf{A}}^\dagger \widehat{\mathbf{A}})$ are equal to zero as

$$\widehat{\mathbf{A}}^\dagger \widehat{\mathbf{A}} \approx \begin{bmatrix} \sum_{j=1}^{2N_t} \widehat{A}_{j,1}^2 & \cdots & 0 \\ \vdots & \ddots & \vdots \\ 0 & \cdots & \sum_{j=1}^{2N_t} \widehat{A}_{j,2N_u}^2 \end{bmatrix}. \tag{4.13}$$

By inserting (4.13) into (4.12) we derive an approximate closed-form solution to calculate the perturbation vector for the optimization problem (4.11) as

$$\hat{u}_k = \frac{1}{\sum_{j=1}^{2N_t} \widehat{A}_{j,k}^2} \sum_{j=1}^{2N_t} \widehat{A}_{j,k} \hat{d}_j \geq 0, \tag{4.14}$$

for each $k = 1, \ldots, 2N_u$ of the vector $\hat{\mathbf{u}}$. The solution of the equation (4.14) must be equal or greater than zero and cannot take negative values.

We extend the solution derived for the constraint $C1$ to meet the $C1, C2, C3, C4$ constraints jointly. We can deduct a new rule from Figure 4.1 and Table 4.1 saying that if a real or imaginary part of a symbol is mapped on the top ring of the constellation ($\mathrm{Re}(\tilde{s}_i) \geq 1$ or $\mathrm{Im}(\tilde{s}_i) \geq 1$) this part can be increased accordingly to the optimal solution. In other cases, the symbol should remain in its original position. Therefore, we define the rule as follows:

$$\hat{u}_k = \begin{cases} \frac{1}{\sum_{j=1}^{2N_t} \widehat{A}_{j,k}^2} \sum_{j=1}^{2N_t} \widehat{A}_{j,k} \hat{d}_j \geq 0 & , \text{if } \hat{s}_i \geq 1 \\ 0 & , \text{if } \hat{s}_i < 1 \end{cases} \tag{4.15}$$

where $\hat{\mathbf{s}} = [\mathrm{Re}(\tilde{\mathbf{s}}^\dagger), \mathrm{Im}(\tilde{\mathbf{s}}^\dagger)]^\dagger \in \mathbb{R}^{2N_u \times 1}$.

We rewrite equation (4.15) in as a pseudo-code in Algorithm 1 to provide some insights on its computational complexity. We see that Algorithm 1 has a fixed number of iterations and that the asymptotic complexity of the complete closed-form solution is $O(N_t \times N_u)$.

Similarly to the technique derived in Chapter 3, the solution provided in equation (4.15) is not optimal and the calculation error of the optimization will increase following the expansion of the dimensions of the matrix $\widetilde{\mathbf{A}}$. We should introduce the scale factor ρ to minimize the calculation error as

$$\mathbf{x} = \mathbf{W}_{\mathrm{ZF}} \mathbf{B}(\tilde{\mathbf{s}} + \rho \tilde{\mathbf{u}}). \tag{4.16}$$

The scale factor ρ can be heuristically estimated ranging its values from 1, when the error is not significant, towards 0 as the error increases.

Algorithm 1 Closed-Form Solution

 1: Input: $\widehat{\mathbf{A}} \in \mathbb{R}^{2N_t \times 2N_u}, \hat{\mathbf{d}} \in \mathbb{R}^{2N_t \times 1}, \hat{\mathbf{s}} \in \mathbb{R}^{2N_u \times 1}$
 2: Output: $\hat{\mathbf{u}} \in \mathbb{R}^{2N_u \times 1}$
 3: **for** $k = 1, 2, \ldots, 2N_u$ **do**
 4:      $a \leftarrow 0$
 5:      $b \leftarrow 0$
 6:      **for** $j = 1, 2, \ldots, 2N_t$ **do**
 7:          $a \leftarrow a + \hat{d}_j \widehat{A}_{j,k}$
 8:          $b \leftarrow b + \widehat{A}_{j,k}^2$
 9:      **end for**
10:      $\hat{u}_k \leftarrow a/b$
11:      **if** $(\hat{u}_k < 0)$ **OR** $(\hat{s}_k < 1)$ **then**
12:          $\hat{u}_k \leftarrow 0$
13:      **end if**
14: **end for**

4.2 Numerical Results

To generate the numerical results, we consider a MU-MIMO system, which has an equal number of the transmit and receive antennas $N_t = N_u = N$. We accordingly generate a full rank $N \times N$ MU-MIMO channel matrix with i.i.d. complex values with a 2-norm matrix condition number defined as

$$\kappa_2(\mathbf{H}) = ||\mathbf{H}||_2 \cdot ||\mathbf{H^{-1}}||_2. \tag{4.17}$$

The matrix condition number corresponds to the ratio of the largest singular value of that matrix to the smallest singular value. In the case of the MU-MIMO system, the matrix condition number describes the power imbalance in the channel. To generate a channel matrix with random i.i.d. values and a desired condition number we calculate singular-value decomposition (SVD) [113] of the generated matrix ($\mathbf{H}$) as $\mathbf{H} = \mathbf{U\Sigma V}^\dagger$. $\mathbf{U}$ is an $N_u \times N_u$ complex unitary matrix, $\mathbf{\Sigma}$ is an $N_u \times N_t$ rectangular diagonal matrix with non-negative real numbers on the diagonal, and $\mathbf{V}$ is an $N_t \times N_t$ real or complex unitary matrix. We reconstruct $\mathbf{\Sigma}$ for its diagonal elements to monotonically increase from 1 to κ_2 as

$$\mathbf{\Sigma}_{\kappa_2} = \mathbf{diag}\left[1, \ldots, \kappa_2\right]. \tag{4.18}$$

The resulting channel matrix is then computed and its power is normalized as

$$\mathbf{H} = \frac{\mathbf{U\Sigma}_{\kappa_2}\mathbf{V}^\dagger}{\sqrt{\sum_{n=1}^{N_u} \sum_{m=1}^{N_t} h_{n,m} h_{n,m}^H}}. \tag{4.19}$$

We average the results over 100 channel matrix iterations with a defined condition number (κ_2). We benchmark the proposed approximate closed-form algorithm (CF SLP) and CVX (CVX SLP) SLP algorithms and measure the total average power of the precoded symbols generated by the techniques in selected channel scenarios. We conduct the benchmarks with the modulation order $M = 16$.

4.2.1 Transmitted Signal Power

In Fig. 4.2 we see the total average power of the CF SLP and CVX SLP algorithms. The power of the precoded symbols generated by the ZF precoder is present as a baseline for
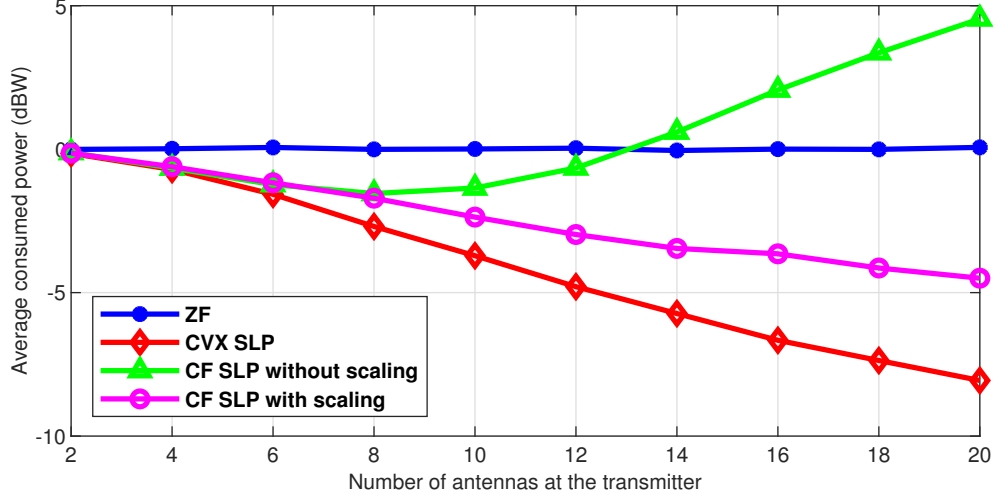
FIGURE 4.2: Total power of the transmitted precoded symbols calculated by ZF, the CF SLP and CVX algorithms.

the benchmarks. This way we can directly compare the increase in the performance of the techniques under the same conditions. The condition number of the channel matrices used in the benchmarks is set as a function of $3N$. For example, for 10 antennas at the transmitter, the condition number of all the 10×10 channel matrices is 30, and for 20 antennas the condition is 60. The impact of the condition number on the solution of the proposed closed-form algorithm was previously demonstrated in Chapter 3. In this benchmark, we choose these values to demonstrate the representative behavior of the algorithm. The CF SLP algorithm performs very closely to the CVX SLP approach up to certain dimensions of the channel matrices. We can see that after the certain size N of the MU-MIMO system the CVX substantially outperforms the CF SLP algorithm in these cases. Moreover, the proposed closed-form algorithm without scaling is performing at higher power than the baseline ZF technique for $N > 14$ region. On the other hand, CF SLP with scaling is performing with lower power than ZF even in the higher regions. The performance is also fairly close to the performance of the CVX algorithm for systems with $N < 10$.

The scaling parameter ρ was selected heuristically and is equal to 1 for $N = 2 \ldots 6$, ρ is equal to 0.5 for $N = 7 \ldots 14$, and ρ is equal to 0.33 for $N = 15 \ldots 20$.

4.2.2 Received Signal Power

In Fig. 4.3 we observe the averaged received power at the receive terminals, which correspond to the consumed power at the transmitter side shown in Fig. 4.2. The received power is decreasing as the number of the transmitting antennas and users increases as the transmit power is limited. The CF SLP algorithm provides higher received power for terminals than ZF in the whole benchmark region due to the perturbation vector $\tilde{\mathbf{u}}$ is positively contributing to the power of the symbols. The CF SLP with the introduced scaling provides less received power than the CVX algorithm.
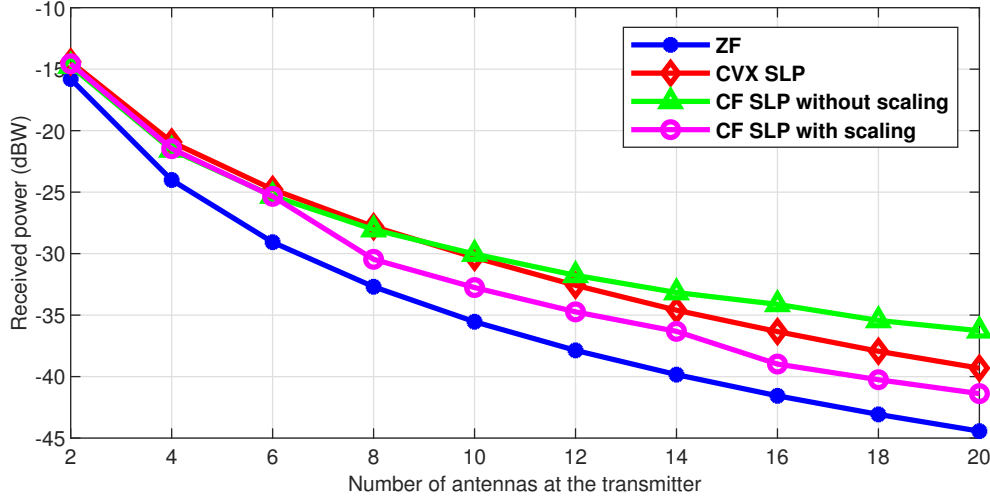
FIGURE 4.3: Received power per UT of the received precoded symbols calculated by ZF, the CF SLP and CVX algorithms.

4.2.3 Signal Processing Time

The following benchmark shows the average processing time per set of N precoded symbols. The benchmark was launched in the MATLAB R2018b environment using a general-purpose central processing unit. Fig. 4.4 shows the time required to process for the ZF, the CF SLP, and the CVX SLP algorithms. Here we do not how separated results for the CF SLP with the scaling and without it. To disable scaling, we set $\rho = 1$ for every N, therefore the algorithm is the same in both cases. The ZF and CF SLP algorithms perform much faster in the conducted benchmark than CVX. The significant improvement of the processing time is a considerable advantage for the closed-form algorithm over CVX. The algorithm potentially allows implementing symbol-level precoding for advanced energy-efficient interference mitigation in novel high-throughput wireless communications.

4.3 Summary

In this chapter, we presented the closed-form algorithm to solve a convex quadratic optimization problem for sum power minimization in the energy-efficient symbol-level precoding. We derive the optimization problem for sum power minimization of symbols in M-QAM constellation and propose a closed-form algorithm to solve this problem with low computational complexity. We demonstrated with numerical benchmarks the efficiency of the precoder design solved by CVX and the proposed closed-form algorithm. The numerical results demonstrated the feasibility of the closed-form algorithm to reduce sum power in a MU-MIMO system. The developed closed-form algorithm provides a trade-off between the efficiency of sum power minimization and much faster processing time. The faster processing time and low complexity of the algorithm are important for the realistic implementation of precoding for energy-efficient wireless communications.
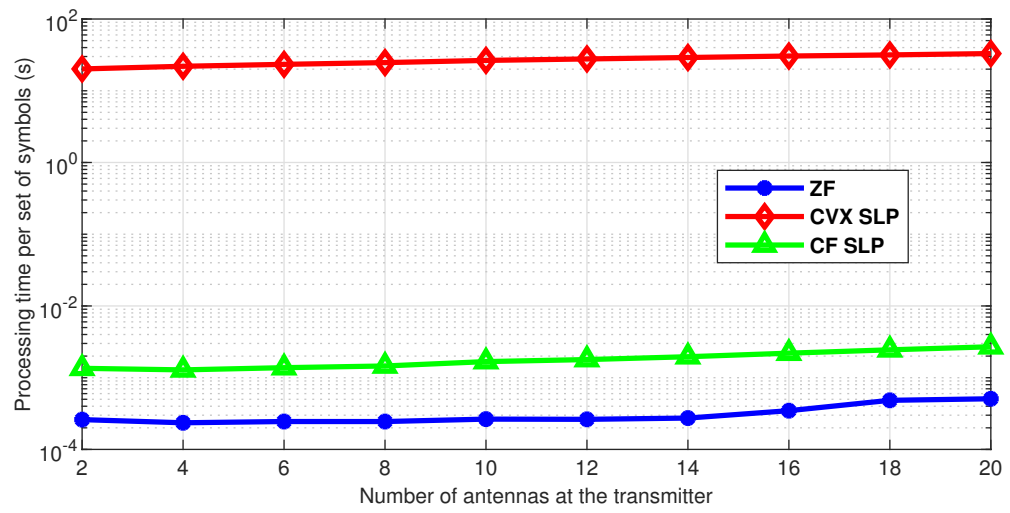
FIGURE 4.4: Average processing time of the precoded symbols calculated by ZF, the CF SLP and CVX algorithms.

Chapter 5

FPGA Acceleration for M-APSK Symbol-Level Precoding Design

In Chapter 3 we design a closed-form solution of a NNLS convex optimization problem for the computationally efficient SLP. The closed-form sub-optimal solution showed a very promising trade-off of the SLP technique performance and processing time when benchmarked against the conventional convex optimization Fast NNLS algorithm [108]. Its computational complexity is in the same order as one of ZF and does not require additional linear algebra operations. Numerical tests revealed a comparable processing time per set of symbols in both ZF and the SLP techniques.

In this chapter, we expand the computationally efficient SLP design to operate in the real-time regime. We develop a complete field-programmable gate array (FPGA) hardware accelerated closed-form algorithm of the SLP technique and optimize it for an actual model of an FPGA silicon chip. For this, we use Vivado High-Level Synthesis (HLS) to translate the algorithm into an Hardware Description Language (HDL) core and integrate the design into an FPGA. We estimate the resource utilization and cycle period. We deploy the HDL core on an actual FPGA board and benchmark its performance in terms of energy efficiency and compare the results with numerical estimations. We draw our conclusion based on the benchmark results and show that the closed-form solution fairly improves the energy efficiency of precoded communications and utilizes a reasonable amount of FPGA resources.

5.1 Computationally Efficient Symbol-Level Precoding

In [114] we benchmarked the symbols throughput of the proposed SLP algorithm in MATLAB environment and achieved over 200 kSymbols per second by running the closed-form algorithm on a standard Intel Central processing unit (CPU). It was shown, that the throughput is only 2 times slower than the performance of the conventional ZF algorithm [40] running on the same CPU. For comparison, by solving the same optimization problem with Fast NNLS algorithm [106] we could reach only around 5 kSymbols per second. For multi-ring constellations, a power minimization problem cannot be solved using the Fast NNLS and more complicated algorithms are required. In [100] we benchmarked the symbol throughput of around 10 Symbols per second in case of 16-APSK modulation while running the optimization code in a similar environment. On the other hand, the closed-form SLP technique can be universally applied for single-ring and multi-ring modulations. It is a good candidate

for realistic real-time hardware implementation in a condition of limited FPGA resources as the same code can be used for multiple modulation types. The same algorithm is optimized for single- and multi-ring constellations and thus no additional algorithm must be developed. We devise an FPGA accelerated design of the precoding technique. Towards a better comprehension of the FPGA code design, in this section, we cover the main implementation aspects of SLP and the approximate closed-form solution.

5.1.1 System Model

We consider a system model, which focuses on the forward link of a multiuser multi-antenna wireless communication system. We assume the full frequency reuse scenario, in which all the antennas transmit in the same frequency and time. The multi-user interference is mitigated using precoding. We define the number of transmitting antenna as N_t and the total number of receiver terminals as N_u in the coverage area. In the specified MIMO channel model, the received signal at the i-th terminal is given by $y_i = \mathbf{h}_i^\dagger \mathbf{x} + n_i$, where $\mathbf{h}_i^\dagger$ is a $1 \times N_t$ vector representing the complex channel coefficients between the i-th terminal and the N_t antennas of the transmitter, $\mathbf{x}$ is defined as the $N_t \times 1$ vector of the transmitted symbols at a certain symbol period and n_i is the independent complex circular symmetric (c.c.s.) independent identically distributed (i.i.d.) zero mean Additive White Gaussian Noise (AWGN) measured at the i-th terminal's receive antenna.

Looking at the concatenated formulation of the received signal, which includes the whole set of receiver terminals, the linear signal model is

$$\mathbf{y} = \mathbf{Hx} + \mathbf{n} = \mathbf{HWs} + \mathbf{n}, \tag{5.1}$$

where $\mathbf{y} = [y_1, y_2, \ldots, y_i] \in \mathbb{C}^{N_u \times 1}$, $\mathbf{n} = [n_1, n_2, \ldots, n_i] \in \mathbb{C}^{N_u \times 1}$, $\mathbf{x} \in \mathbb{C}^{N_t \times 1}$, and $\mathbf{s} \in \mathbb{C}^{N_u \times 1}$ and $\mathbf{H} = [\mathbf{h}_i^\dagger, \mathbf{h}_i^\dagger, \ldots, \mathbf{h}_i^\dagger] \in \mathbb{C}^{N_u \times N_t}$. In this scenario, we define a precoding matrix $\mathbf{W} \in \mathbb{C}^{N_t \times N_u}$ which maps the information symbols $\mathbf{s}$ into precoded symbols $\mathbf{x}$. We consider the data symbols $\mathbf{s}$ to be unit variance complex vectors $|s_i| = 1$ for every $i = 1, 2, \ldots, N_u$.

5.1.2 Optimization Problem Definition

We consider the optimization problem of the computationally efficient SLP technique, which aims to minimize the sum power of the precoded symbols at the gateway side. The technique applies to the M-th order amplitude and phase-shift keying (M-APSK) modulations. It reduces the sum power of the precoded symbols by optimally increasing the amplitudes of the initial data symbols to exploit the constructive interference at the receiver side. The method optimally preserves constructive interference components to decrease the total transmitted power at the transmitter side. The essential difference of the SLP technique from a linear precoding method is the optimization vector $\mathbf{u} = [u_1, u_2, \ldots, u_i] \in \mathbb{C}^{N_u \times 1}$, which is recalculated for every set of symbols $\mathbf{s}$ to construct the optimized precoded signal given by

$$\mathbf{x} = \mathbf{W}(\mathbf{\Gamma} \bullet \mathbf{s} + \mathbf{u}), \tag{5.2}$$

where $\mathbf{\Gamma} = [\Gamma_1, \Gamma_2, \ldots, \Gamma_i] \in \mathbb{R}^{N_u \times 1}$ is per terminal SNR requirements. The following formulation allows us to split the problem of constructing optimal beamforming into two independent tasks: channel orthogonalization and optimal symbol mapping for energy efficiency. In this scenario, we define the precoding matrix ($\mathbf{W}$) as the Zero-Forcing linear precoder:

$$\mathbf{W}_{\mathrm{ZF}} = \hat{\mathbf{H}}^\dagger (\hat{\mathbf{H}} \hat{\mathbf{H}}^\dagger)^{-1}, \tag{5.3}$$

where $\hat{\mathbf{H}}$ is the channel matrix estimated from the channel state information (CSI). We choose ZF for its properties to orthogonalize the channel so that in the case of $\hat{\mathbf{H}} = \mathbf{H}$ the received symbols are a summation of the transmitted symbols, the optimization vector and Gaussian noise:

$$\mathbf{y} = \mathbf{H}\mathbf{W}_{\text{ZF}}(\boldsymbol{\Gamma} \bullet \mathbf{s} + \mathbf{u}) + \mathbf{n} = \boldsymbol{\Gamma} \bullet \mathbf{s} + \mathbf{u} + \mathbf{n}. \tag{5.4}$$

By using the ZF precoding matrix we guarantee to meet the SNR constraints in the design of SLP and simplify the precoder. The optimal symbol mapping we derive in the following paragraphs.
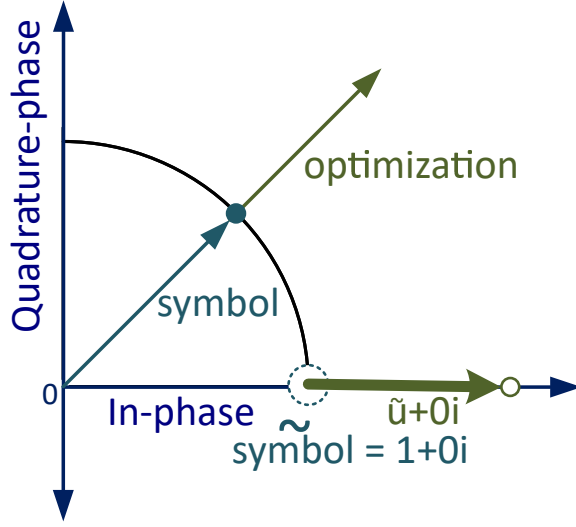
FIGURE 5.1: Symbol optimization of the proposed Symbol-Level Precoding.

In Fig. 5.1 we demonstrate the effect of the optimization u_i on a single complex data symbol s_i with unit power. The optimization vector increases the absolute magnitude of the symbol and keeps its phase in a fixed direction. In a case of the multi-ring constellation we consider, that power of the symbols, which are mapped to the external ring, is $|s_i| \geq 1$. All the symbols on the internal rings with power $|s_i| < 1$ retain their original position.

The optimization problem, which we consider in this implementation can be summarized as in Chapter 3

$$\begin{aligned} \min_{\tilde{\mathbf{u}}} \quad & \|\widetilde{\mathbf{A}}\tilde{\mathbf{u}} - \tilde{\mathbf{d}}\|_2 \\ \text{s. t.} \quad & \tilde{u}_i \geq 0, |s_i| \geq 1, \\ & \tilde{u}_i = 0, |s_i| < 1, \end{aligned} \tag{5.5}$$

for all $i = 1, 2, \ldots, N_u$. Where $\widetilde{\mathbf{A}} = [\text{Re}(\mathbf{A}); \text{Im}(\mathbf{A})] \in \mathbb{R}^{2N_t \times N_u}$, $\tilde{\mathbf{d}} = [\text{Re}(\mathbf{d}^\dagger), \text{Im}(\mathbf{d}^\dagger)]^\dagger$, and $\mathbf{A} = \mathbf{W}_{\text{ZF}}\mathbf{B}$ and $\mathbf{d} = -\mathbf{W}_{\text{ZF}}\mathbf{B}\tilde{\mathbf{s}}$. $\mathbf{B}$ is defined as in (3.6).

The problem (5.5) can be solved by using CVX [109, 110] and the algorithm proposed in Chapter 3.

5.1.3 Approximate Closed-Form Solution

We consider the closed-form solution (CF NNLS SLP) developed in Chapter 3:

$$\tilde{u}_i = \begin{cases} \frac{1}{\sum_{j=1}^{2N_t} \widetilde{A}_{j,i}^2} \sum_{j=1}^{2N_t} \widetilde{A}_{j,i} \tilde{d}_j \geq 0 & , |s_i| \geq 1 \\ 0 & , |s_i| < 1. \end{cases} \tag{5.6}$$

In the expression the solution must be equal to zero ($u_i = 0$) for every symbol in the internal rings $|s_i| < 1$ and must be non-negative ($u_i \geq 0$) for every symbols in the external ring $|s_i| = 1$. In this case the internal constellation symbols are fixed to their original position. The (5.6) can be also applied to solve the problem (5.5), thus it is a complete solution for any type of PSK and APSK modulations.

The approximate solution (5.6) is solved and considered as converged in a single iteration contrary to the Fast NNLS. The asymptotic complexity of the complete approximate closed-form solution is $O(N_t \times N_u)$, which is considerably less complex than Fast NNLS.

5.2 FPGA Implementation Design of CF NNLS SLP

We use Vivado HLS to design the HDL core. Vivado HLS accelerates IP creation by enabling C, C++, and System C specifications to be directly targeted into Xilinx programmable devices without the need to manually create a register-transfer level (RTL) design. Thus, in this section, we translate the computationally efficient SLP technique to a pseudo-code and analyze its computational complexity. We optimize the core for the Xilinx Kintex-7 xc7k410TFFG-2 FPGA model. This particular model is installed in a wide set of commercially available SDRs by National Instruments, like NI USRP (Universal Software Radio Peripheral) 2954R and FlexRIO (Reconfigurable IO) 7976R.

5.2.1 Algorithm Description

For the convenience of the implementation analysis, we rewrite the equation (5.6) as a pseudo-code algorithm (2). The algorithm consists of only two **for** loops, where each of them has a constant number of iterations, which allows us to design the FPGA core at the target symbol throughput. The input arguments of the algorithm is the matrix $\widetilde{\mathbf{A}}$ and the vector $\tilde{\mathbf{d}}$. The output is a vector of the regression coefficients $\tilde{\mathbf{u}}$.

Finally, we derive the complete pseudo-code of the computationally efficient SLP technique in Algorithm 3. The input arguments of the algorithm is a Zero-Forcing precoding matrix $\widehat{\mathbf{W_{ZF}}}$ and a vector of data symbols $\mathbf{s}$. There is no dedicated input for the vector of SNR requirements $\mathbf{\Gamma}$ as it is directly incorporated into the matrix $\mathbf{W_{ZF}}$ as $\widehat{\mathbf{W_{ZF}}} = \mathbf{W_{ZF}\Gamma}$. The output is a vector of precoded symbols $\mathbf{x}$. We implement the condition check for multi-ring modulation at line 22 to fully implement the approximate closed-form solution (5.6). Therefore, the described algorithm does not need a configuration parameter to indicate the type of symbol modulation at the input.

5.2.2 HDL Core I/O Ports Description

The input and output (I/O) ports of the HDL core are presented in Table 5.1. We designed the core using the AXIS handshake for the optimal data transfer towards and from the core. The input port W receives a precomputed precoding matrix and has no handshake signaling.

Algorithm 2 Closed-Form Solution Algorithm

1: Input: $(\widetilde{\mathbf{A}} \in \mathbb{R}^{2N_t \times N_u}, \widetilde{\mathbf{d}} \in \mathbb{R}^{N_t \times 1})$
2: Output: $\widetilde{\mathbf{u}} \in \mathbb{R}^{N_u \times 1}$
3: **for** $i = 1, 2, \ldots, N_u$ **do**
4: $\quad a \leftarrow 0$
5: $\quad b \leftarrow 0$
6: $\quad$ **for** $j = 1, 2, \ldots, 2N_t$ **do**
7: $\quad\quad a \leftarrow a + \tilde{d}_j \tilde{A}_{j,i}$
8: $\quad\quad b \leftarrow b + \tilde{A}_{j,i}^2$
9: $\quad$ **end for**
10: $\quad \tilde{u}_i \leftarrow a/b$
11: $\quad$ **if** $(\tilde{u}_i < 0)$ **then**
12: $\quad\quad \tilde{u}_i \leftarrow 0$
13: $\quad$ **end if**
14: **end for**

The data on this port should be ready before signaling to the port s_TREADY. The bit width of the data ports depends on the bit width of the complex fixed-point format (c_f_p).

The detailed format of the port W is described in Table 5.2. The real and imaginary parts of each entry of the matrix $\mathbf{W}_{\text{ZF}}$ are concatenated and are mapped to a vector in the order as shown in the table. The entries of the matrix are concatenated row by row so that the first row should start at the bit 0, following by the second row and the last row should end at the most significant bit (MSB).

The format of the port s_TDATA is described in Table 5.3. The real and imaginary parts of each entry of the vector $\mathbf{s}$ are concatenated and are mapped to a vector in the order as shown in the table. The first entry starts at the bit 0, following by the second entry and the last entry ends at the most significant bit.

The format of the port x0_TDATA is described in Table 5.4. The real part of the first symbol is placed at the bit 0. Its imaginary part is appended after the real part. The rest of the symbols are concatenated in the same order until the MSB is the imaginary part of the last symbol.

5.2.3 Functional Behavior Description

In Fig. 5.3 we see the complete flow of the core functional behavior for multiple sets of symbols. In this demonstration, we feed the port W of the core with an identity matrix $\boldsymbol{\mathcal{I}}_N \in \mathbb{R}^{N \times N}$ during all the cycles defined as

$$
\boldsymbol{\mathcal{I}}_N = \begin{bmatrix} 1 & 0 & 0 & \ldots & 0 \\ 0 & 1 & 0 & \ldots & 0 \\ 0 & 0 & 1 & \ldots & 0 \\ \vdots & \vdots & \vdots & \ddots & \vdots \\ 0 & \ldots & 0 & 0 & 1 \end{bmatrix}.
\tag{5.7}
$$

The core reads $N_t \times N_u$ elements of the matrix and a set of N_u symbols in parallel in a single cycle. During the iteration cycle 0 we feed the s_TDATA port with a vector of symbols $\mathbf{s}_1 = [0.7071 + 0.7071i, 0.7071 + 0.7071i, \ldots, 0.7071 + 0.7071] \in \mathbb{C}^N$ and switch s_TVALID

TABLE 5.1: HDL core I/O ports.

Symbol	I/O	Width	Name	Description
ap_clk	I	1	Primary clock	Primary system clock. The system is synchronous and operates at the rising edge of this clk signal.
W	I	c_f_p*N_t*N_u	Precoding matrix	Complex values of the Zero-Forcing precoding matrix reshaped to a vector.
s_TDATA	I	c_f_p*N_u	Vector of input symbols	Complex values of the input symbols.
s_TVALID	I	1	AXIS input valid	Data input valid. When asserted the data are valid for input on the port s_TDATA.
s_TREADY	O	1	AXIS input ready	Data input ready. When high the core signals that the port s_TDATA is ready for input.
x0_TDATA	O	c_f_p*N_u	Vector of output symbols	Complex values of the output symbols.
x0_TVALID	O	1	AXIS output valid	Data output valid. When high the core signals that the data are valid for output on port x0_TDATA.
x0_TREADY	I	1	AXIS output ready	Data output ready. When asserted the data are ready to output on the port s_TDATA.

TABLE 5.2: Data port W format.

W[MSB downto 0]				
$\mathrm{Im}(W_{\mathrm{ZF}N_t,N_u})$	$\mathrm{Re}(W_{\mathrm{ZF}N_t,N_u})$	...	$\mathrm{Im}(W_{\mathrm{ZF}1,1})$	$\mathrm{Re}(W_{\mathrm{ZF}1,1})$

TABLE 5.3: Data port s_TDATA format.

s_TDATA[MSB downto 0]				
$\mathrm{Im}(s_{N_u})$	$\mathrm{Re}(s_{N_u})$	...	$\mathrm{Im}(s_1)$	$\mathrm{Re}(s_1)$

60

Algorithm 3 Complete SLP algorithm

1: Input: $(\widehat{\mathbf{W_{ZF}}} \in \mathbb{R}^{N_t \times N_u}, \mathbf{s} \in \mathbb{R}^{N_u \times 1})$
2: Output: $\mathbf{x} \in \mathbb{R}^{N_t \times 1}$
3: **for** $j = 1, 2, \ldots, N_t$ **do**   ▷ Compute matrix $\mathbf{A}$
4:     **for** $i = 1, 2, \ldots, N_u$ **do**
5:         $A_{j,i} \leftarrow W_{\text{ZF}j,i} s_i$
6:     **end for**
7: **end for**
8: **for** $j = 1, 2, \ldots, N_t$ **do**   ▷ Build matrix $\widetilde{\mathbf{A}}$
9:     **for** $i = 1, 2, \ldots, N_u$ **do**
10:         $\widetilde{A}_{j,i} \leftarrow \text{Re}(A_{j,i})$
11:         $\widetilde{A}_{j+N_t,i} \leftarrow \text{Im}(A_{j,i})$
12:     **end for**
13: **end for**
14: **for** $j = 1, 2, \ldots, 2N_t$ **do**   ▷ Compute vector $\widetilde{\mathbf{d}}$
15:     $\widetilde{d}_i \leftarrow 0$
16:     **for** $i = 1, 2, \ldots, N_u$ **do**
17:         $\widetilde{d}_j \leftarrow \widetilde{d}_j + \widetilde{A}_{j,i}$
18:     **end for**
19: **end for**
20: $\widetilde{\mathbf{u}} \leftarrow \textbf{Algorithm 2}(\widetilde{\mathbf{A}}, (-\widetilde{\mathbf{d}}))$ ▷ Compute vector $\widetilde{\mathbf{u}}$
21: **for** $i = 1, 2, \ldots, N_u$ **do**
22:     **if** $|s_i| < 1$ **then**   ▷ Eq. (5.6) condition
23:         $\widetilde{u}_i \leftarrow 0$
24:     **end if**
25: **end for**
26: **for** $j = 1, 2, \ldots, N_u$ **do**   ▷ Compute vector $\mathbf{x}$
27:     $x_j \leftarrow 0$
28:     **for** $i = 1, 2, \ldots, N_t$ **do**
29:         $x_j \leftarrow x_j + W_{\text{ZF}j,i} s_i + W_{\text{ZF}j,i} \widetilde{u}_i$
30:     **end for**
31: **end for**

---

from low to high. At the interval cycle 1 we switch s_TVALID back to low. We feed the port s_TDATA with a new set of symbols $\mathbf{s}_2 = [-0.7071 - 0.7071i, -0.7071 - 0.7071i, \ldots, -0.7071 - 0.7071] \in \mathbb{C}^N$ and switch s_TVALID again from low to high for the period of interval cycle 2. We can see, that the port x0_TVALID switches from low to high during the same iteration cycle. We can read the data on the port x0_TDATA. At the interval cycle 4 we feed the port s_TDATA again with the set of symbols $\mathbf{s}_1$. We can see, that the output data corresponds to the input data delayed by 2 cycles as $\mathbf{x} = \mathcal{I}_N \mathbf{s}_1$ at the cycle 2 and $\mathbf{x} = \mathcal{I}_N \mathbf{s}_2$ at the cycle 4. The core produces output data every 2 cycles, which are delayed by 2 cycles with respect to the corresponding input data.

5.2.4   FPGA Resource and Timing Performance

We define the complex fixed-point format as 16 signed bits (C1.15) for the design of the HDL core. The format allocates 16 signed bits to real values and 16 bits to complex values, which
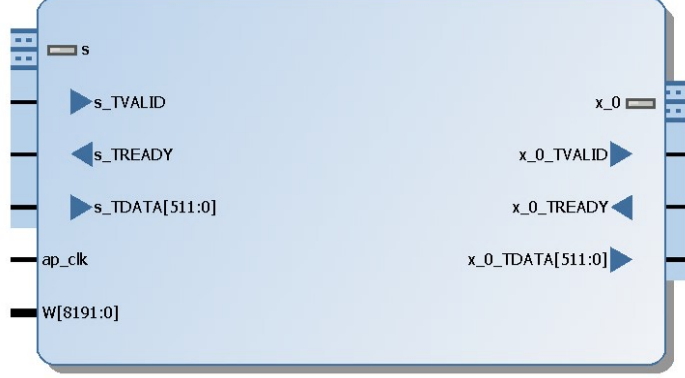
FIGURE 5.2: Core schematic symbol.

TABLE 5.4: Data port x0_TDATA format.

x0_TDATA[MSB downto 0]				
$\text{Im}(x_{N_u})$	$\text{Re}(x_{N_u})$	...	$\text{Im}(x_1)$	$\text{Re}(x_1)$

TABLE 5.5: HDL core resource occupation on Kintex-7 (xc7k410TFFG900-2).

# of stream	DSP	Slices	LUT	Baudrate per stream	Total throughput
4	4%	2%	3%	83 MBd	332 MBd
6	33%	8%	15%	83 MBd	498 MBd
8	59%	13%	24%	83 MBd	664 MBd
10	92%	19%	34%	83 MBd	830 MBd
Available	1540	508400	254200		

results in a total of 32 bits for a single complex value. We target the HDL core to operate at the symbol rate of 83 MSymbols per second. The motivation behind the target is the new symbols rates, which are considered in the DVB-S2X standard [115]. We estimate the resource consumption by the core design for a number of transmitting antennas and receiver terminals $N = N_t = N_u = 4$, 6, 8 and 10. In Table 5.5 we see the numerical estimation of the FPGA resource utilization for a different number of beams. For all the scenarios the core is optimized to operate at a 166 MHz clock ($\approx$ 6 ns per cycle) with a cycle interval 2. The clock allows to operate at the 166 MHz/2 = 83 MSymbols per second symbol rate per each receiver terminal. For the 10 transmitting antennas and 10 receiver terminals case, the design utilizes around 92 percent of the DSP blocks available at the given FPGA model (xc7k410TFFG-2).
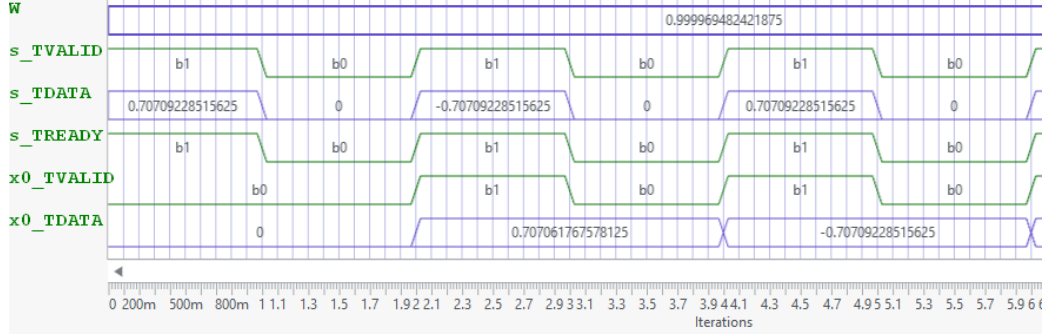
FIGURE 5.3: Functional behavior of the control ports for the first 7 iteration cycles.

5.3 Experimental Validation

In this section, we benchmark the performance of Algorithm 3 implemented on the HDL core and deployed on an actual FPGA against the same algorithm running in a MATLAB environment. The HDL core is implemented using fixed-point arithmetic, while MATLAB is running in a float-point precision mode. We estimate the difference between the arithmetic precision implementations.
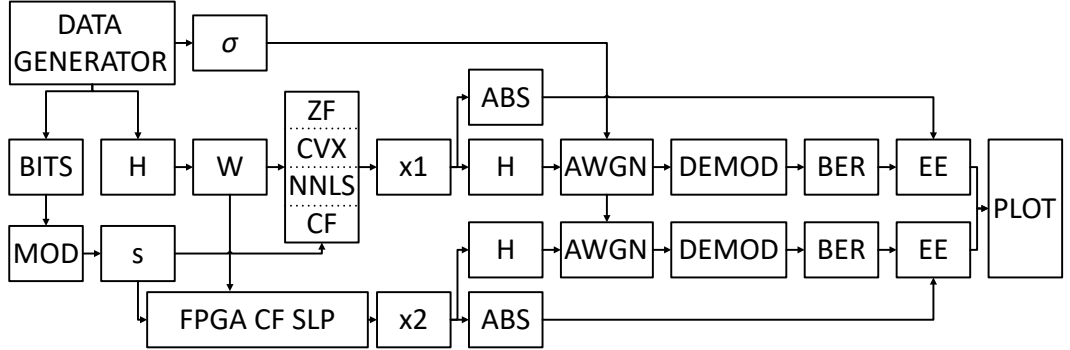
FIGURE 5.4: Schematic block diagram of the benchmark of the SLP implementation.

In Fig. 5.4 we show the block diagram of the conducted benchmark. We benchmark energy efficiency (EE) of the presented SLP technique implemented on FPGA and in MATLAB environments. In MATLAB we generate data bits, a channel matrix $\mathbf{H}$, a precoding matrix $\mathbf{W}$ and modulated data symbols $\mathbf{s}$. We generate a $N_t \times N_u$ channel matrix with a specific 2-norm matrix condition number.

We calculate precoded symbols $\mathbf{x1}$ using the ZF and the computationally efficient SLP implemented in MATLAB with CVX (CVX SLP), Fast NNLS (NNLS SLP) or the approximate closed-form (CF NNLS SLP) optimization algorithms. We use Fast NNLS algorithm for M-PSK and CVX for M-APSK constellations optimization. The approximate closed-form algorithm is used for both these constellations. We transfer the same set of the generated symbols with the precoding matrix to the FPGA node, which runs the HDL core to calculate precoded symbols $\mathbf{x2}$ using the approximate closed-form algorithm (FPGA SLP). The two

63

versions **x1** and **x2** of the precoded symbols are multiplied by the channel matrix and mixed with the AWGN noise. We demodulate the resulting signals and calculates BER scores for each precoding algorithm. Finally, we calculate EE as

$$\text{EE}(E_b/N_0) = \frac{\log_2(M)(1 - \text{BER}(E_b/N_0))}{\|\mathbf{x}_{\text{norm}}\|_2}, \tag{5.8}$$

where $\|\mathbf{x}_{\text{norm}}\|_2$ is the normalized average sum power of the precoded symbols and $E_b/N_0 = 10\log_{10}(\frac{1}{\log_2(M)\sigma^2})$ is the energy per bit to noise power spectral density ratio.
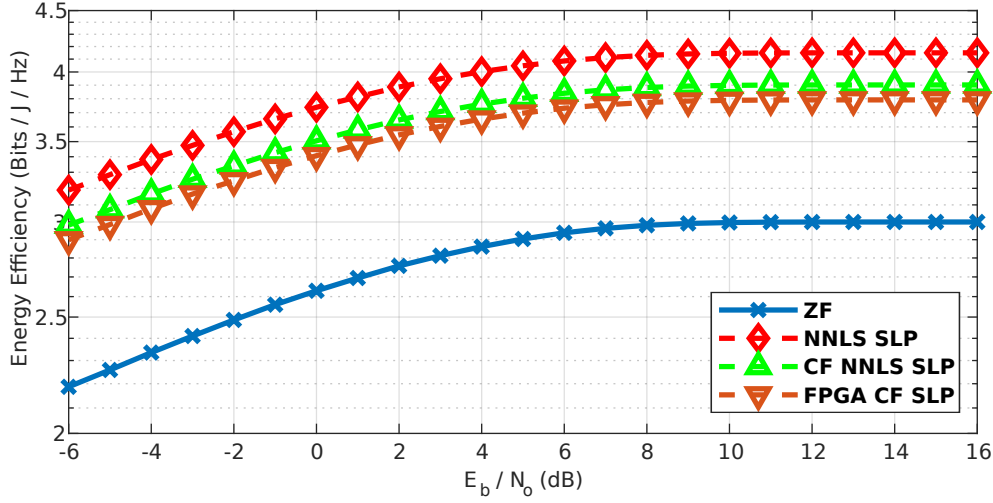

FIGURE 5.5: Energy efficiency curves of 8-PSK for FPGA implementation of FPGA SLP compared to ZF, NNLS SLP and CF NNLS SLP on MATLAB.

In Fig. 5.5 we can see the energy efficiency curves as a function of E_b/N_0 of the ZF, NNLS SLP, and CF NNLS SLP algorithms for 8-PSK constellation symbols. We average the results over 50 iterations of $N_t = N_u = 6$ channel matrices with a condition number ($\kappa_2(\mathbf{H})$) fixed to 18. The difference between the performance of the Fast NNLS and the CF algorithms running in the MATLAB environment is around 2.5 dB due to the approximation method used in the closed-form solution. We also observe an additional 1 dB difference between the MATLAB and FPGA implementations of the CF algorithm due to the fixed-point implementation.

In Fig. 5.6 we demonstrate energy efficiency benchmarks as a function of E_b/N_0 of the ZF, CVX SLP, and CF NNLS SLP algorithms for 16-APSK symbols. We generate 16-APSK symbols with constellation radius ratio $\gamma = 3.15$ and average the results over 10 iterations of $N_t = N_u = 6$ channel matrix with a condition number $\kappa_2(\mathbf{H}) = 18$. In this case, we observe that CVX optimization is 1 dB more efficient than the CF algorithm in the MATLAB environment. But as we previously discussed and demonstrated in [100] CVX has much lower symbol throughput than the CF algorithm and ZF. The FPGA implementation of the CF algorithm demonstrate similar result with an additional 1 dB performance loss due to the fixed-point implementation.

The CF algorithm designed for FPGAs delivers considerably improved energy efficiency when compared to ZF in all the benchmarks. The Fast NNLS and CVX solutions are shown to outperform the CF algorithm, but they are not designed to run in real-time on an FPGA. The FPGA implementation operates at a high symbol throughput but has an additional
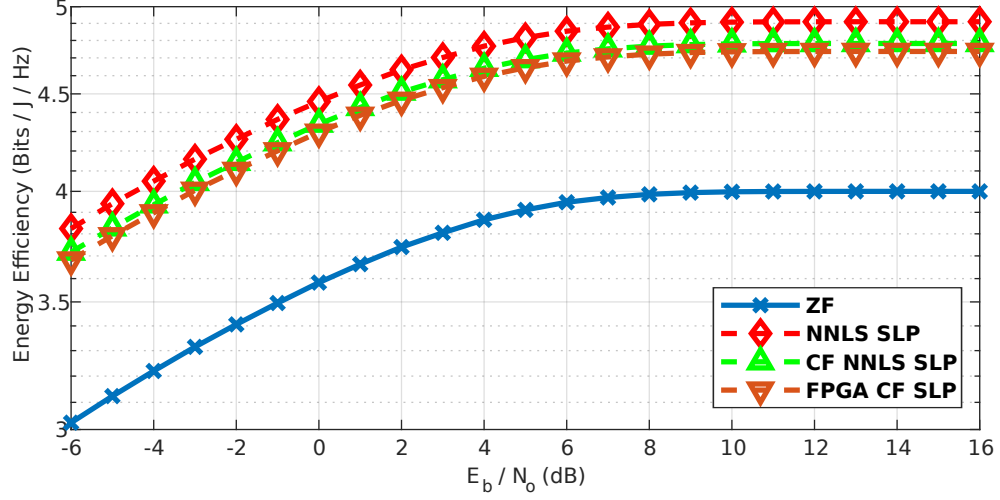
FIGURE 5.6: Energy efficiency curves of 16-APSK ($\gamma = 3.15$) for FPGA implementation of FPGA SLP compared to ZF, CVX SLP and CF NNLS SLP on MATLAB.

energy efficiency loss of 1 dB due to losses in fixed-point arithmetic. This drawback can be addressed if we choose to increase the number of bits in the fixed-point arithmetic at the cost of extra FPGA resources.

5.4 Summary

In this chapter, we devised an FPGA accelerated design of the energy and computationally efficient symbol-level precoding operating in a real-time operation mode, the first such case to our knowledge. We successfully deployed and validated the design on an actual FPGA platform.

We describe the algorithmic code, the I/O ports mapping, and the functional behavior of the FPGA design. We optimized the design of the HDL core to operate at up to 83 MSymbols per second throughput per each receiver terminal with up to 20 simultaneously operating terminal units while utilizing a reasonable amount of the FPGA resources. The achieved symbol throughput is considered for the DVB-S2X standard [115] communications. The designed HDL core universally supports single- and multi-ring symbol modulations with fixed-phase optimization. It can directly operate with any M-PSK and M-APSK constellation and does not need to reconfigure. The approximate closed-form algorithm, which we developed for the FPGA design, demonstrated a 2 dB loss of energy efficiency during the conducted benchmarks against conventional Fast NNLS and CVX optimization algorithms. We also measured an additional 1 dB loss of energy efficiency of the approximate closed-form algorithm when deployed on an actual FPGA platform. This can be addressed with increased precision of the fixed-point implementation at the expense of FPGA resources.

Chapter 6

In-lab Real-time Test-bed for Precoded Communications in Multi-Beam UHTS Systems

In this chapter, we show the implementation of the in-lab test-bed for the closed-loop precoded SATCOM. We describe the design and functionality of the multi-beam DVB-S2X compliant GW, the satellite MIMO Channel Emulator and the set of UTs. We validate the design requirements using reasonable software and hardware resources.

We implemented the physical layer of the DVB-S2X standard using commercial SDR platforms. Developing on SDR allows us to rapidly prototype and deploy the precoded transmission in a more realistic environment rather than using only numerical simulations.

6.1   In-lab test-bed

In this chapter, we present a in-lab test-bed to demonstrate closed-loop precoded communications for interference mitigation in multi-beam Ultra High Throughput Satellites (UHTS) under realistic environments. For this matter, we designed a scalable architecture of the gateway and user terminals compatible with the DVB-S2X superframe structure. Fig. 6.1 shows the block diagram of the test-bed and on Fig. 6.2 we show the actual photo of the test-bed during a public demonstration.

We use the commercially available SDR platform developed by National Instruments (NI). The platform consists of two NI PXI (PCI EXtension for Instruments) 1085 chassis, which allow centralised connection of the set of the NI USRP 2954R and FlexRIO 7976R. The NI USRP and FlexRIO have integrated FPGA module Kintex-7 from Xilinx.

The gateway simultaneously transmits 6 precoded signals towards 6 user terminals through a 6×6 multi-beam satellite channel emulator. The channel emulator acquires the gateway signals, applies the impairments of the satellite payload, Gaussian noise, and the multi-beam interference and transmits the signals to the UTs. The UTs estimate the CSI based on the DVB-S2X standard pilots and report the estimated values to the gateway through a dedicated feedback channel over an Ethernet link. The gateway uses this CSI data to compute a precoding matrix. The table 6.1 summaries the current capabilities and the final targets of the test-bed.
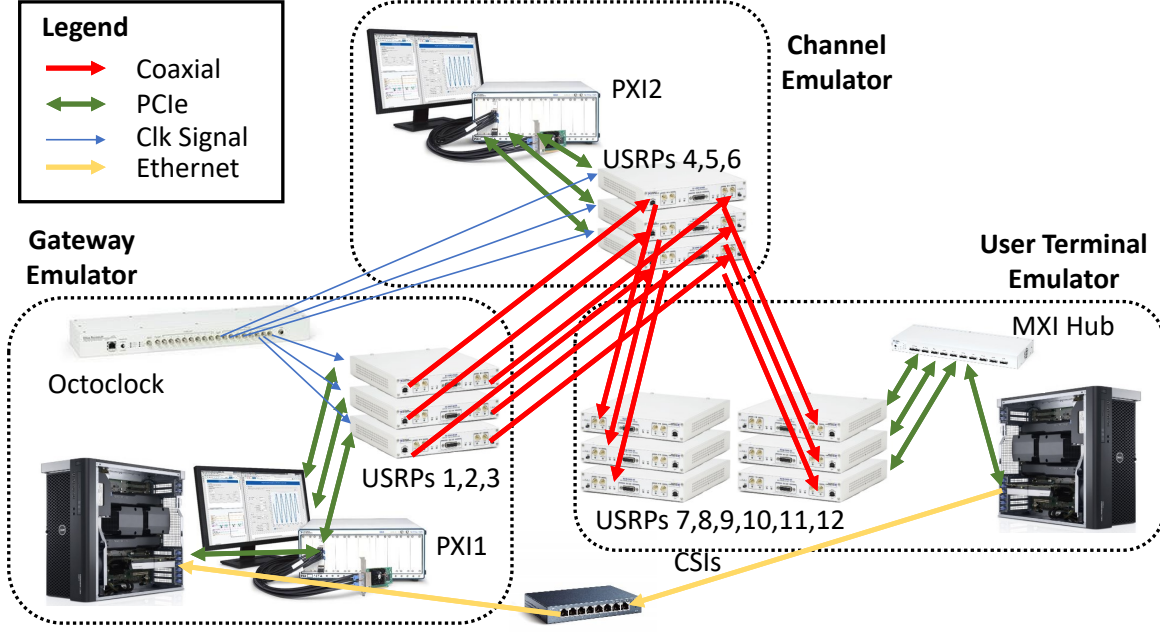
FIGURE 6.1: Block diagram of the in-lab test-bed.

6.1.1 System Model

We consider a system model, which focuses on the forward link of a multi-beam satellite system. We assume a full frequency reuse scenario, in which all the beams transmit in the same frequency and time. The multi-user interference is mitigated by using signal precoding techniques. The number of transmitting antennas is equal to the total number of users in the coverage area. In this case, we consider a 6×6 MIMO channel. In the specified MIMO channel model, the received signal at the i-th terminal is given by $y_i = \mathbf{h}_i^\dagger f(\mathbf{x}) + n_i$, where $\mathbf{h}_i^\dagger$ is a 1×6 vector representing the complex channel coefficients between the i-th terminal and the 6 antennas of the transmitter, $\mathbf{x}$ is defined as the 6×1 vector of the transmitted symbols of DVB-S2X superframe at a certain symbol period and n_i is the independent complex circular symmetric (c.c.s.) independent identically distributed (i.i.d) zero mean Additive White Gaussian Noise (AWGN) inserted to the i-th terminal's receive signal. The function $f(\mathbf{x})$ represents the non-linear behaviour of the satellite channel.

Looking at the general formulation of the received signal, which includes the whole set of terminals, the signal model is

$$\mathbf{y} = \mathbf{H}f(\mathbf{x}) + \mathbf{n} = \mathbf{H}f(\mathbf{Ws}) + \mathbf{n}, \tag{6.1}$$

where $\mathbf{y} \in \mathbb{C}^{6 \times 1}$, $\mathbf{n} \in \mathbb{C}^{6 \times 1}$, $\mathbf{x} \in \mathbb{C}^{6 \times 1}$, and $\mathbf{s} \in \mathbb{C}^{6 \times 1}$ and $\mathbf{H} \in \mathbb{C}^{6 \times 6}$. We consider the data symbols $\mathbf{s}$ to be unit variance complex vectors $|s_k| = 1$ for every $k = 1 \ldots 6$.

6.1.2 Gateway

The gateway operates with a central NI FlexRIO FPGA and 3 NI USRP nodes. The 3 NI USRP nodes are connected to the same oscillator reference clock source. A single NI

FIGURE 6.2: Photo of the in-lab test-bed.

TABLE 6.1: Parameters of the in-lab test-bed.

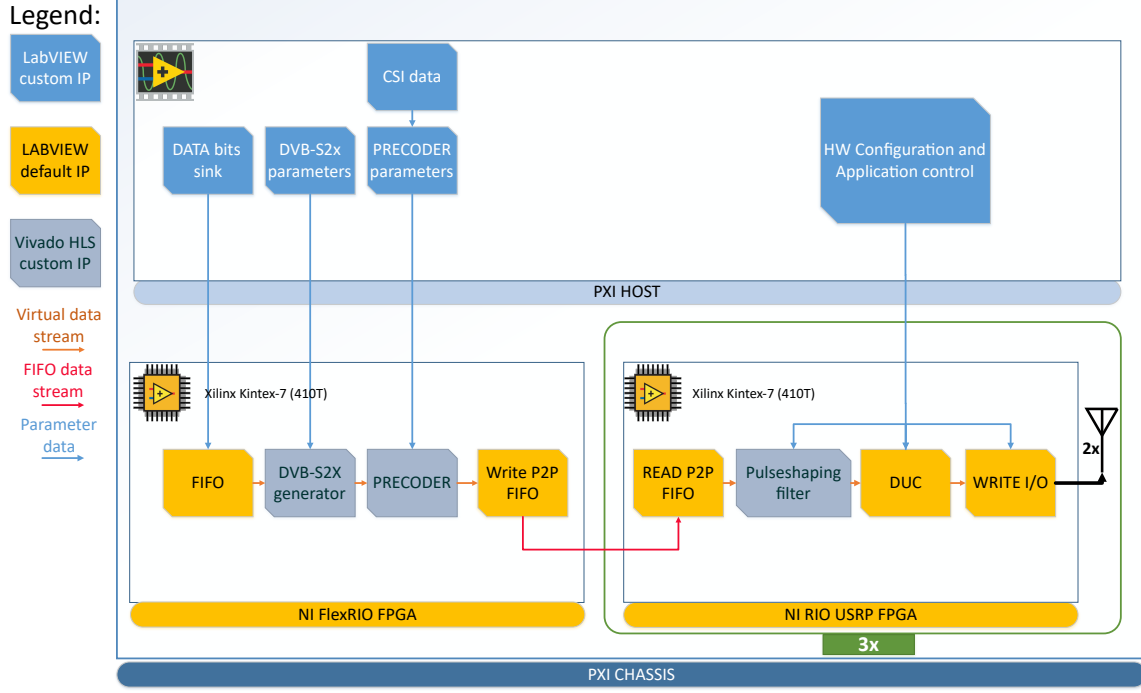| Parameter	Value
Gateway IQ channels	6
Sampling frequency	24.8 MHz
Oversampling factor	4
Gateway TX freq.	1.21 GHz
Channel Emulator RX freq.	1.21 GHz
Channel Emulator TX freq.	960 MHz
User Terminal RX freq.	960 MHz
Filter roll-off factor	0.2
Forward Error Correction	LDPC with BCH
LDPC code rate	1/2, 2/3, 3/4, 4/5

FIGURE 6.3: Block diagram of the DVB-S2X Gateway.

USRP has only 2 RF outputs. In order to transmit 6 independent signals on 6 RF channels simultaneously, we need to utilize 3 NI USRP nodes. It is required to have the synchronized frequency and time clocks in all the nodes while performing joint beamforming. The Fig. 6.3 shows the logical connections between the NI FlexRio, the NI USRP nodes, and the controller (NI PXI HOST). Here the upper blue section represents the processes implemented in the host computer and the lower yellow section represents the blocks implemented in the FPGA for fast processing.

The FPGA IP block of the DVB-S2X deployed in the NI FlexRio generates 6 parallel streams of symbols of the DVB-S2X superframe. Each stream carriers terminal-specific data. The streams can be independently configured through the dedicated graphical interface as shown in Fig. 6.4.

We implemented the configurations, which are covered by the DVB Standards [115, 116], namely: MODulation and CODing Mode (MODCOD), Super-Frame Format Indicator (SFFI), Index Stream, Index of the Walsh-Hadamard (WH) matrix, scramble flag for Pilots and Start Of Super-Frame (SOSF).

The streams are jointly precoded by the PRECODE IP block. The PRECODE IP block multiplies 6 symbols from a single time slot with the precoding matrix $\mathbf{W}$ and performs the SLP optimization. Additionally, the precoding mask controls precoding behavior over the segments of the DVB-S2X superframe as illustrated in Fig. 6.5.

Through the configuration panel we can enable and disabled Zero-Forcing and SLP Precoding techniques for each segment of the DVB-S2X superframe. We disable Precoding for SOSF and P pilots under normal operation. The SOSF is a known sequence, which can be reliably detected at a user terminal even in a high interference environment. The P pilots are not precoded because they are used by UTs to estimate the CSI ($\hat{\mathbf{H}}$).

FIGURE 6.4: DVB-S2X Gateway configuration graphical interface.

FIGURE 6.5: Precoding mask configaration for DVB-S2X superframe structure.
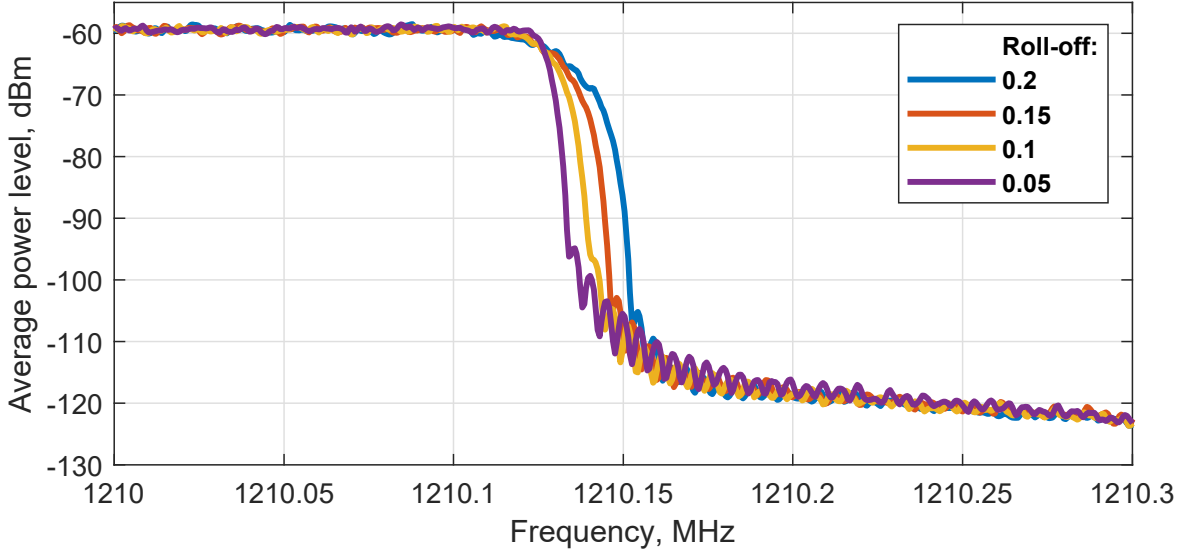
FIGURE 6.6: Frequency characteristics of the transmitted signal.

The streams with 6 superframes are transferred to the 3 NI USRP nodes, where the signals are oversampled using the Pulshaping filter IP block. The filter's impulse response is given by the Raised-cosine function with different roll-off factors. The roll-off factor of the filter response is configurable according to the DVB-S2X standard. In this iteration of the in-lab test-bed, we implemented the roll-off factors of 0.2, 0.15, 0.1, and 0.05. We measured the actual filter's frequency response for these roll-off values as shown in Fig. 6.6. The oversampled signals are processed by the digital upconverter (DUC) and transmitted to the RF domain at the desired carrier frequency.

6.1.3 Channel Emulator

The channel emulator is running on a PXI HOST controller, a NI FlexRIO module for central signal processing, and 3 NI USRP nodes for the RF front-end. The nodes are interconnected as shown in Fig. 6.7. Each NI USRP node acquires two streams of the sampled baseband, which are generated by the digital down converter (DDC). Therefore, by utilizing 3 synchronized RIO USRP nodes the channel emulator simultaneously samples 6 independent RF baseband streams. The RF inputs and outputs of the NI USRP nodes operate in RF bands of the Low Noise Block (LNB) in the GW uplink and the LNB on the UTs downlink. All the effects that occur in the actual Ka-band are emulated in the channel emulator.

We designed and implemented custom IP blocks into USRP FPGA nodes to emulate the channel impairments in real time. We designed and build an additive white Gaussian noise (AWGN) generator [117] with configurable amplitude.

The streams from the 3 USRP nodes are transferred to the FlexRIO FPGA. The channel matrix ($\mathbf{H}$) is jointly applied towards all the streams by the MIMO Channel Emulator IP block. The desired channel matrix is controlled by the PXI HOST. The 6×6 matrix of complex coefficients is based on the realistic satellite beam pattern illustrated in Fig. 6.8. The beam pattern makes use of the Ka-band exclusive band 19.7 to 20.2 GHz. We consider a scenario of full frequency reuse, where the same frequency band is applied in every beam. We can simultaneously select up to 6 user terminals in the coverage area and generate realistic

FIGURE 6.7: Block diagram of the channel emulator.

channel coefficients.

The resulting signals with added interference are transferred back to the corresponding NI USRP nodes. In every NI USRP node, the signal is upsampled in DUC and sent through the RF analog outputs. The RF inputs and outputs of the channel emulator operate at different carrier frequencies as shown in the Table. 6.1. Using this configuration we decrease the mutual coupling between the transmission and reception links through the RF part of the Channel Emulator to facilitate the accuracy of the designed channel matrix.

6.1.4 User Terminal

The User Terminals (UT) are the are ground-based users which collect the transmitted waveforms and recover the transmitted data bits. The UTs are implemented using the same SDR platform used in for the Gateway and the Channel Emulator, the USRP RIO NI2944. We use 6 USRPs for each independent UT. The FPGA of a single USRP performs signal processing of the UT chains and communicates with the host computer.

Fig. 6.9 shows an architectural block diagram of the UT implementation. The FPGA interface the RF daughter boards, which down-convert the incoming RF signal using an analog local oscillator. The FPGA reads the ADCs sampled data coming in four sampled streams for the two IQ down-converted pairs. The sampling rate of this particular SDR platform is 200 MSPS. After sampling, two DDC blocks take the two IQ sampled streams. Each DDC shifts in frequency the IQ streams using a Numerically Controlled Oscillator, and applies a decimation filter in order to produce a decimated output stream at a selectable sampling rate. The frequency shifting performed in the DDC has the advantage of avoiding the problematic zero-frequency part of the spectrum after analog down-conversion, which usually is corrupted by some leakage of the local oscillator signal.

Due to the efficient FPGA accelerated processing, a single USRP RIO FPGA unit is capable to receive DVB-S2X compliant signal in real-time. The DVB-S2X processing chain is capable of recovering the format 2 and 3 super-frames from the DVB-S2X standard. These

FIGURE 6.8: ESA71 beam pattern, antenna performance.

processes include frequency acquisition, matched filtering, time synchronization, frame (including Super-Frame) synchronization, fine phase tracking, and CSI estimation. The recovered symbols contain the payload data plus the pilot structure of the DVB-S2X framing. All the frame fields and the CSI information are passed to the host computer for their further utilization. The host computer reports the CSI information to the central GW using a custom feedback channel.

We use a custom web server for CSI feedback through the Internet. The CSI web server acts as a middleman between the UTs and the GW. The purpose of the server is to store, log and provide CSI and telemetry data. The server can be accessed by the GW and the UTs though the Internet or local networks and can be used in the over satellite and in-lab demo for reliable CSI data transfer.

6.2   Summary

In this chapter, we present the in-lab test-bed for precoding in DVB-S2X systems. The in-lab test-bed is a full-chain closed-loop communication system with a multi-beam gateway transmitter, MIMO channel emulator, and user terminals with real-time CSI estimation. With the in-lab test-bed, we are able to show experimentally the application of precoding in
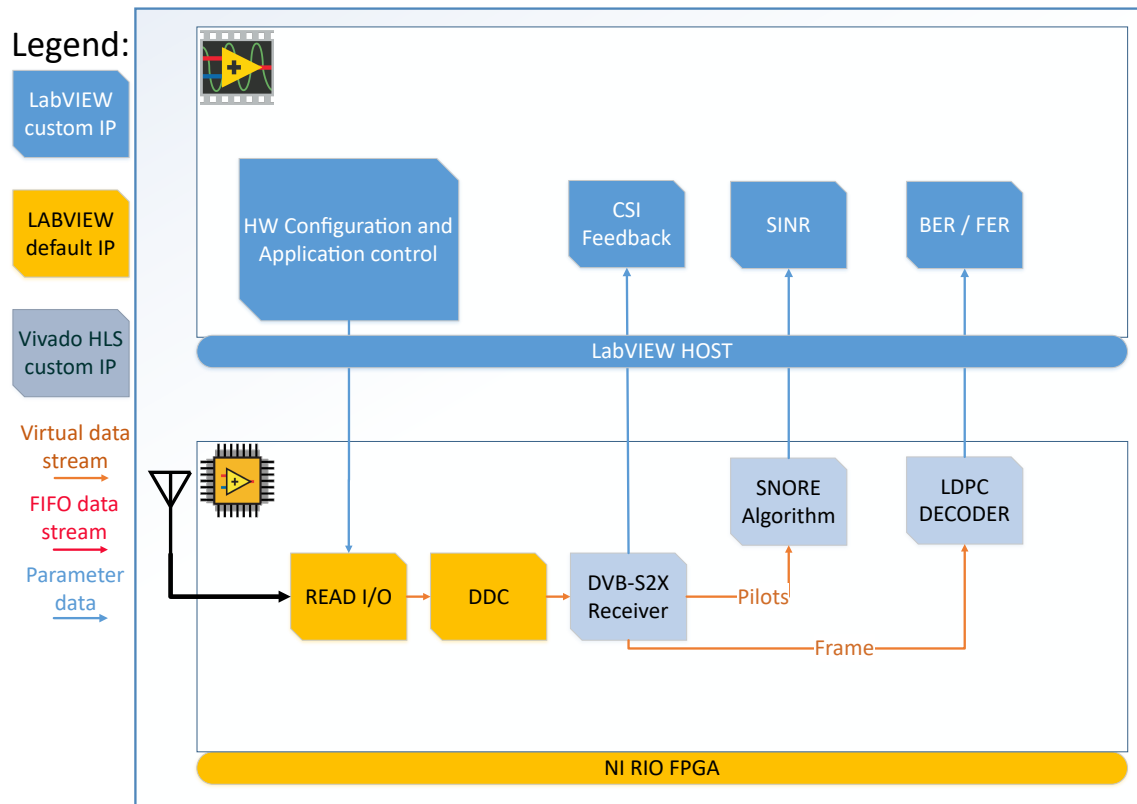
FIGURE 6.9: Block diagram of the User Terminal.

satellite communications based on the DVB-S2X standard.

In-lab Validation of M-APSK Symbol-Level Precoding

7.1 Introduction

In this chapter, we investigate coded BER and FER and spectral efficiency performance of the closed-form SLP running in a real-time operation mode. We implemented a DVB-S2X compatible receiver. The receiver estimates SINR from the pilots embedded into the DVB-S2X frame and decodes information bits from the data symbols using Logarithmic Likelihood ratio (LLR) estimations and the Low Density Parity Check (LDPC) decoder. We compare the SINR, BER, FER, and spectral efficiency performance of SLP to a conventional ZF precoding technique. In this benchmark, the receiver was not modified in any way to decode symbols modified by the SLP processing at the GW side. Thus, we investigate the impact of the SLP symbols on a conventional receiver chain. The benchmark resembles a realistic SLP processing deployment in communication systems, where only the transmitter is modified, while the user terminals stay unchanged.

7.2 System Parameters

7.2.1 SINR Estimation

To evaluate the performance of the precoding techniques, we consider the signal-to-interference-plus-noise ratio (SINR) measured on the actual pilots at the UT side rather than using SINR estimation based on the precoding matrix [49]. SINR estimation is suitable for SLP techniques, where SINR depends on both the precoding matrix and the symbol constructive interference. The authors in [118] showed that estimating SINR at the UT side is more reliable than SINR calculated at the gateway side. The DVB-S2 implementation guidelines [116] describe the Signal-to-Noise Ratio Estimation (SNORE) algorithm (Fig. 7.1).

FIGURE 7.1: SNORE algorithm.

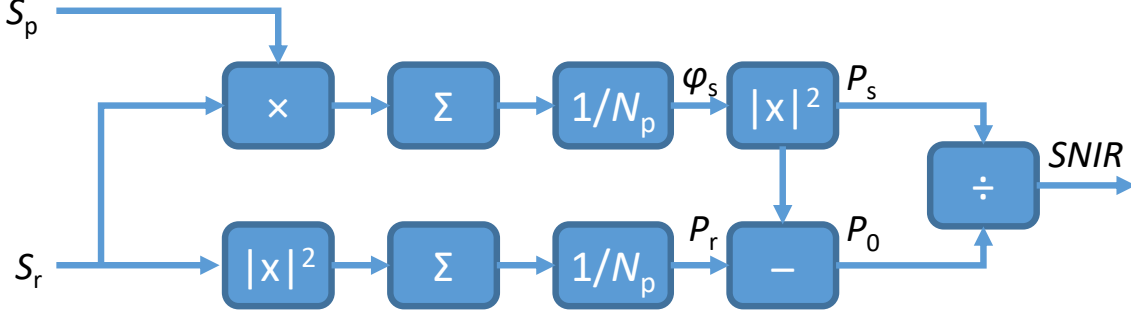The SNORE algorithm work in data-aided (DA) operating mode. The DA mode is bias-free until very low $E_c/N_t < -20$ dB [116]. The pilot presence allows us to use the DA version of the SNORE algorithm operating on the pilot time slots and therefore we insert pilots into the beginning of transmitted frames for each user. The pilot sequence for i-th UT is generated as in [115] part E.3.5.3. The pilot fields are determined by a Walsh-Hadamard (WH) sequence of size 32 plus padding of a WH sequence of size 16. A set of $2^5 = 32$ orthogonal WH sequences result from the following recursive construction principle:

$$\mathbf{P}_m = \begin{bmatrix} \mathbf{P}_{m-1} & \mathbf{P}_{m-1} \\ \mathbf{P}_{m-1} & -\mathbf{P}_{m-1} \end{bmatrix}, \tag{7.1}$$

starting from $m > 1$ and $\mathbf{P}_1 = 1$ until $\mathbf{P}_{32}$ is denoted. The i-th row of $\mathbf{P}_{32}$ corresponds to the i-th WH sequence with $i = 1 \ldots 32$. For the sake of padding, a matrix of size 32×16 is appended. This matrix is generated from $\mathbf{P}_{16}$ by repeating $\mathbf{P}_{16}$ vertically to get:

$$\mathbf{P}_{\text{padding}} = \begin{bmatrix} \mathbf{P}_{16}; \mathbf{P}_{16} \end{bmatrix}. \tag{7.2}$$

Combining both matrices together yields:

$$\mathbf{P}_{\text{pilot3}} = \begin{bmatrix} \mathbf{P}_{32}; \mathbf{P}_{\text{padding}} \end{bmatrix}, \tag{7.3}$$

hosting the whole set of possible pilot sequences row by row. The selection of the parameter i is a static choice for the transmit signal, thus we transmit i-th sequence to the i-th UT. The pilot sequences are multiplied by $(1 + \iota)\sqrt{2}$ to generate complex symbols.

At each UT, SINR is calculated as follow:

$$\frac{E_b}{N_0} = \frac{P_s}{P_N}, \tag{7.4}$$

where P_S - power of the intended signal and P_N - power of noise plus interference. We calculate P_s as

$$P_S = \frac{1}{48} | \sum_{t=1}^{48} y_i[t] \times P_{\text{pilot3}_i}[t]|^2 \tag{7.5}$$

We calculate P_N from the total signal power

$$P_N = P_R - P_s, \tag{7.6}$$

where $P_R = \frac{1}{48} \sum_{t=1}^{48} |y_i[t]|^2$.

7.2.2 LLR Calculation

For robust communication under noisy channels, the UT performs the Forward Error Correction (FEC) of the recovered DVB-S2X encoded payloads symbols. The soft demodulation is performed using a LLR algorithm. The LDPC decoder uses the LLR values to recover information bits from the symbols. The classical formulation of the LLR is:

$$LLR_j = \ln \left[\frac{\sum_{b:b_j=0} \exp \left(\frac{-\|r-c(b)\|^2}{2\sigma^2} \right)}{\sum_{b:b_j=1} \exp \left(\frac{-\|r-c(b)\|^2}{2\sigma^2} \right)} \right], \tag{7.7}$$

where σ^2 is the noise variance, r is the received complex symbol, and c is the nominal constellation complex point. Thus, to compute the j-th bit LLR from r, one may compute the squared distance to each of the constellation points, separating those constellation points that have a 0 in bit j from those that have a 1. A common approximation to the LLR is to approximate each sum in 7.7 by its largest term, i.e., by using only the nearest constellation point that has $b_j = 0$ in the numerator, and the nearest neighbor that has $b_j = 1$ in the denominator. The approximate LLR can be expressed as in [119]

$$LLR_j = \frac{1}{2\sigma^2} \left(\|r - c_1\|^2 - \|r - c_0\|^2 \right). \tag{7.8}$$

Equation 7.8 is used in the following benchmarks. The LLR values obtained are quantized into 6-bit fixed-point values, represented as five bits for the integer part (one of these 5 bits is used for the sign) and one bit for the fractional part of the LLR, so obtaining values that range from -15.5 up to +15.5. For this particular case, the quantization is implemented in a saturated and symmetrical fashion, to avoid the -16 minimum value, which represents a bias in the calculation. The fixed-point arithmetic operations are implemented due to the receiver's hardware performance requirements.

7.2.3 LDPC

The error correction capability of a FEC system strongly depends on the amount of redundancy as well as on the coding algorithm itself. The LDPC codes are powerful, capacity-approaching channel codes and have exceptional error correction capabilities. The high degree of parallelism that they offer enables efficient, high-throughput hardware architectures. The LDPC decoder in the receiver implements the LDPC Block Codes (LDPC-BC) or QC-LDPC Quasi-Cyclic LDPC Codes as mentioned in the literature [115, 116]. These LDPC codes are based on block-structured LDPC codes with circular block matrices. The entire parity check matrix can be partitioned into an array of block matrices, each block matrix is either a zero matrix or a right cyclic shift of an identity matrix. The parity check matrix designed in this way can be conveniently represented by a base matrix represented by cyclic shifts. The main advantage of this feature is that they offer high throughput at low implementation complexity. The current LDPC decoder implementation uses an approximation of the log-domain LDPC iterative decoding algorithm (Belief propagation) known as Layered Offset Min-Sum Algorithm [120]. The decoder is highly reconfigurable and is tailored for the DVB-S2 standard.

The supported modes of the available LDPC decoder block are shown in Table 7.1.

TABLE 7.1: LDPC decoder supported modes.

Mode	Frame Size	Code rate (C_R)
0	64800	1/2
1	32400	1/2
2	64800	2/3
3	32400	2/3
4	64800	3/4
5	32400	3/4
6	64800	5/6
7	32400	5/6

7.3 Channel Coefficients and CSI

We use a realistic channel matrix generated based on provided beam pattern as shown in Fig. 7.2. In Fig. 7.3 we can see the example channel matrix used in the channel emulator, which corresponds to the selected beams in the pattern. The condition number of the channel matrix is 3.52984. It is possible to use other beam patterns and beam scenarios by configuring the channel emulator.

FIGURE 7.2: Channel selected beams configuration.

	1	2	3	4	5	6
1	0.2721 + 0.0000i	-0.0082 + 0.1513i	0.0052 - 0.0020i	-0.0154 - 0.0303i	-0.0075 + 0.0001i	-0.0067 + 0.0051i
2	-0.0172 + 0.0328i	0.3988 - 0.0000i	0.0190 + 0.0248i	0.0111 + 0.0037i	0.0515 - 0.0367i	0.0034 - 0.0182i
3	-0.0046 + 0.0062i	-0.0245 - 0.0505i	0.3698 + 0.0000i	6.1035e-04 + 8.5449e-04i	0.1573 + 0.0663i	0.0281 - 0.0134i
4	0.1548 + 0.0064i	-0.1847 + 0.0419i	-0.0121 + 0.0207i	0.2847 + 0.0000i	-0.0051 - 0.0320i	0.0184 + 0.0007i
5	0.0009 - 0.0075i	-0.0595 - 0.1018i	0.1466 - 0.0063i	0.0742 - 0.0377i	0.3857 - 0.0000i	0.1308 + 0.1546i
6	-3.3569e-04 - 1.5259e-04i	0.0006 + 0.0087i	0.2330 + 0.0942i	0.0003 + 0.0024i	-0.1504 + 0.1480i	0.2881 + 0.0000i

FIGURE 7.3: Applied channel matrix in the channel emulator.

Next, we see the actual channel estimated by the UTs and reported to the GW in Fig. 7.4. This estimation differs from the actual channel matrix applied in the channel emulator due to hardware impairments, digital scaling factor, and cable losses between the GW and the UTs. We run numerical simulations of this estimated CSI data to evaluate the theoretical performance of the SLP and ZF precoders.

	1	2	3	4	5	6
1	0.3834 + 0.0000i	-0.0004 - 0.0325i	-0.0045 + 0.0112i	-0.0991 - 0.2055i	-0.0111 - 0.0359i	0.0201 - 0.0157i
2	0.0944 - 0.0920i	0.3101 + 0.0000i	0.0165 - 0.0210i	-0.0631 + 0.1730i	0.0540 + 0.0380i	0.0051 + 0.0216i
3	-0.0111 - 0.0383i	0.0382 - 0.0468i	0.3826 + 0.0000i	0.0074 + 0.0773i	-0.0616 + 0.1089i	0.0638 - 0.2535i
4	0.0470 + 0.0161i	-0.0164 + 0.0109i	-0.0369 + 0.0037i	0.4325 - 0.0000i	0.0600 - 0.0117i	0.0226 + 0.0545i
5	-0.0082 + 0.0223i	-0.0455 + 0.0045i	-0.1172 - 0.0148i	0.0079 - 0.0737i	0.2022 + 0.0000i	0.0483 + 0.1917i
6	0.0126 - 0.0213i	0.0325 - 0.0046i	0.0886 - 0.0069i	-0.0002 + 0.0179i	-0.1229 + 0.0879i	0.2641 + 0.0000i

FIGURE 7.4: Estimated channel matrix.

In Fig. 7.5 we can see the estimated TX power of ZF and SLP vs the SNR target at the UTs. The TX power of the SLP is not greater than ZF for the given channel configuration. On the same figure, we see that SLP delivers more RX power than ZF to the UTs under the same channel conditions. At this stage, we verified that the provided channel matrix can be exploited by SLP to minimize the TX power and improve the RX power.

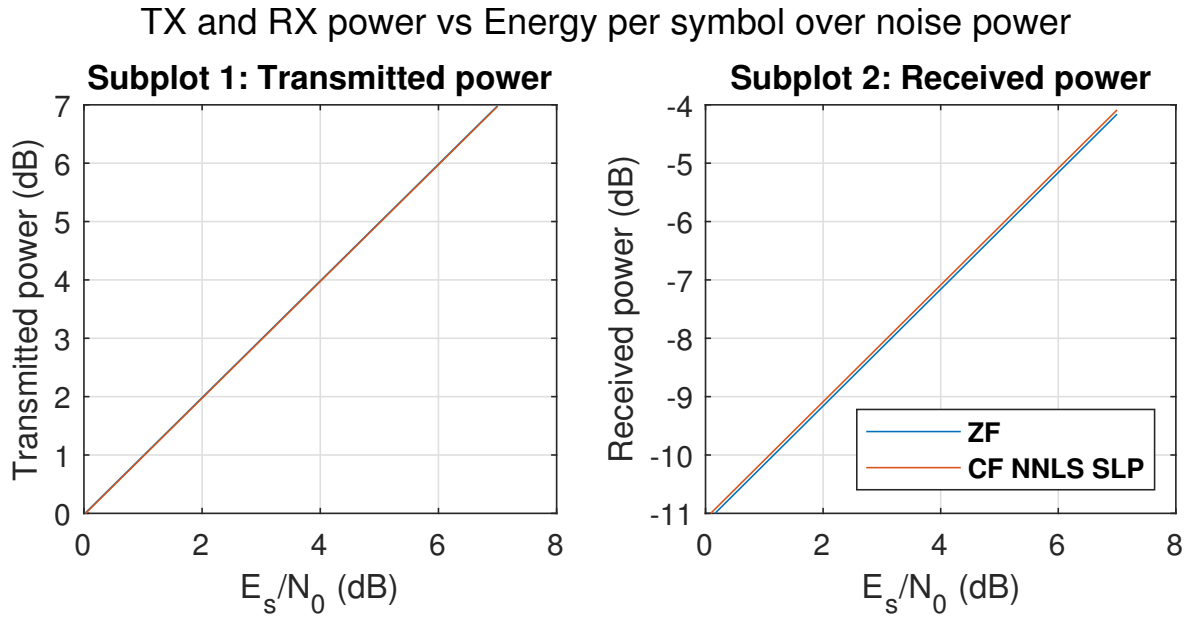## TX and RX power vs Energy per symbol over noise power

FIGURE 7.5: TX and RX power vs Energy per symbol over noise power.

In Fig. 7.6 we can see the expected RX power gains per each UT for the ZF and the SLP techniques. We can see, that using the estimated channel matrix and the SLP technique the expected gains due to SLP modified symbols appear in the UTs 2, 3, 5, and 6.
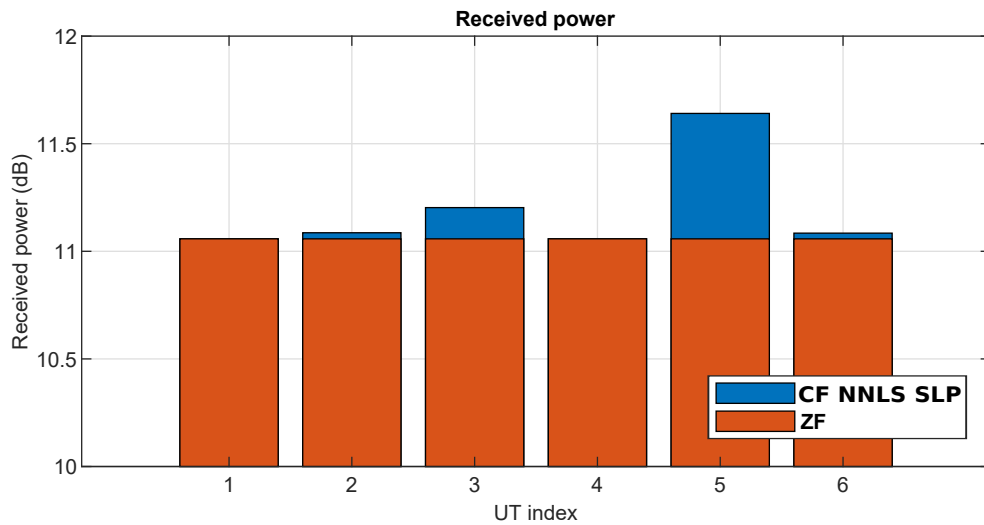

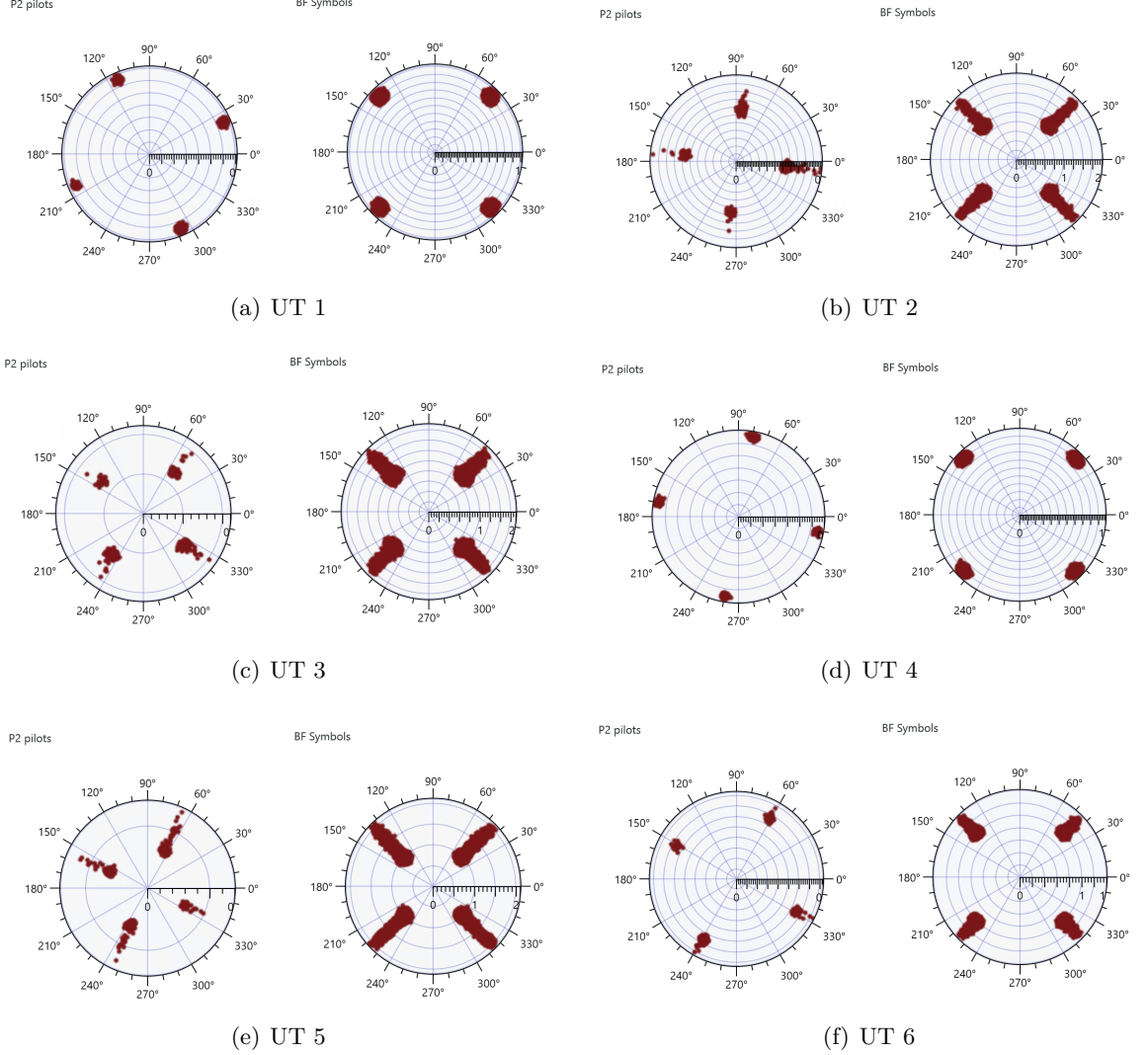
FIGURE 7.6: Average RX power per UT.

(a) UT 1   (b) UT 2

(c) UT 3   (d) UT 4

(e) UT 5   (f) UT 6

FIGURE 7.7: Received P2 pilots and bundle frame QPSK symbols at UTs modified by CF NNLS SLP.

7.4 Experimental Validation

7.4.1 Received Symbols of CF NNLS SLP

In Fig. 7.7 we can see received P2 pilots and bundle frame QPSK symbols for each UT. The phase of the P2 pilots is not fully recovered as we see the rotated QPSK constellations. The UTs use the information about the phase and amplitude of the pilots to recover the phase and amplitude of the bundle frame (BF) symbols. The BF symbols modified by the SLP are visible in the UTs 2, 3, 5, and 6. These results matching the theoretically estimated gains per each UT from the previous section, which indicates that the SLP algorithm is correctly deployed in the hardware.

Also, in Fig. 7.8 we see how the SLP technique optimizes symbol constellations from higher order PSK and APSK constellations. The symbols on the external rings of the constellations are always optimized in the fixed-phase direction. The symbols from the internal rings keep their original position and are not optimized by the SLP to avoid inter-symbol

BF Symbols
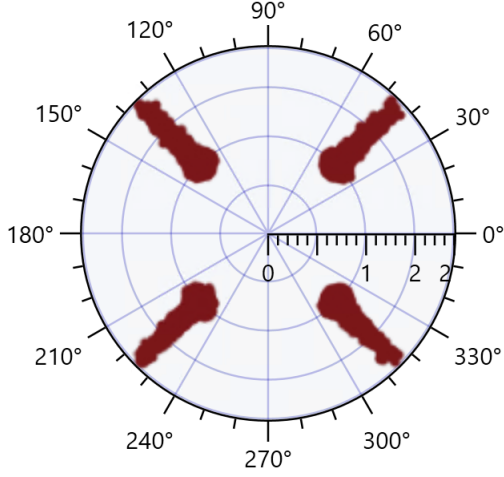
BF Symbols

BF Symbols

BF Symbols

(a) QPSK
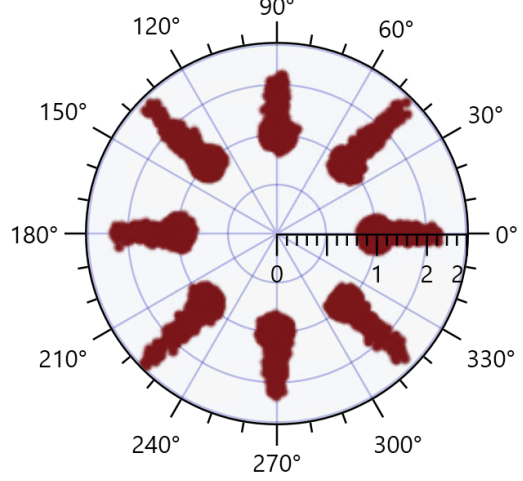
(b) 8-PSK
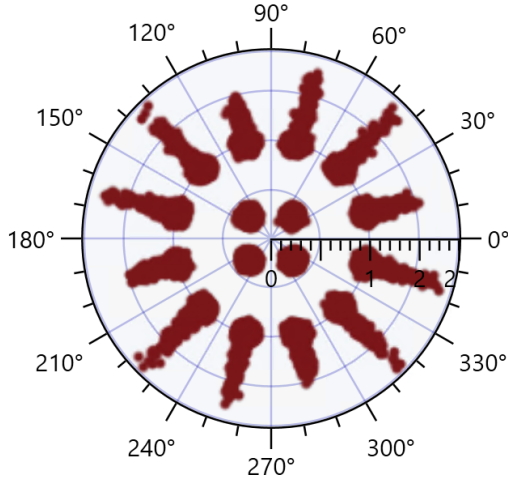
(c) 16-APSK
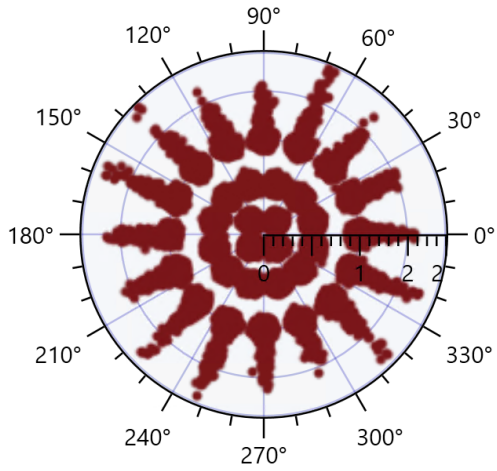
(d) 32-APSK

FIGURE 7.8: Received PSK and APSK symbols at UTs modified by CF NNLS SLP.

interference at the UTs. As discussed in Chapter 5 the SLP algorithm adapts automatically to the selected constellation and does not need to be reconfigured.

7.4.2 SINR Performance of CF NNLS SLP

We set the relative noise power in the channel emulator to 0 to measure the SINR ($SINR_0$) at the UT for the ZF technique. We then increase the relative noise power with a 0.2 dB step to measure the SINR estimations in the region of our interest. We calculate the average SINR value and the standard deviation of the average at each point by measuring SINR from

1000 bundle frames. We also calculate the SINR value at the channel emulator as $SINR_0 +$ relative noise power.

In Fig. 7.9 we can see the estimated and expected SINR curves. In the ZF case, the SINR estimation is close to the SINR, calculated using the relative noise power at the channel emulator. The values are within the range of the standard deviation from the channel emulator SINR values. In the SLP case, the estimation of the SINR in the high SINR region ($> 8 \ dB$) is lower than the channel emulator SINR and SINR estimated for ZF. Below the 8 dB threshold, SINR estimated in SLP is consistently higher than the channel emulator SINR and the ZF SINR values. The P2 pilot symbols with an amplitude excursion due to SLP in the interference-limited scenario are treated by the SNORE algorithm as interference, resulting in underestimation of the SINR. In the noise-limited scenario, these symbols result in consistent overestimation of the SINR.
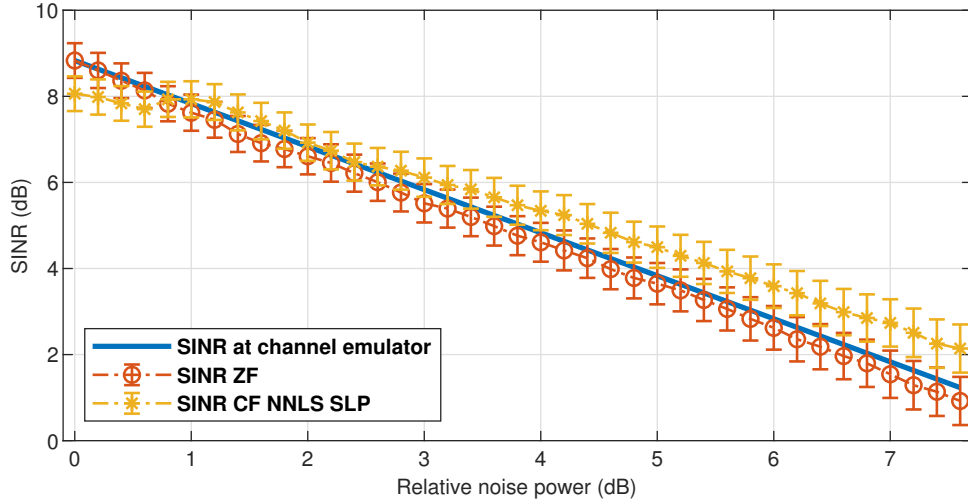
FIGURE 7.9: Experimental SINR curves for ZF and SLP techniques, and the channel emulator estimated SINR vs the relative noise power.

7.4.3 Coded Bit Error Rate Performance of CF NNLS SLP

In Fig. 7.10 we show LDPC BER using QPSK constellation. Each point is averaged from 1 million LDPC blocks, where each block is 64800 bits long. The BER curves are plotted against the SINR estimated at the channel emulator, which is based on the noise power rather than the estimated SINR by SLP or ZF to achieve a fair comparison of both systems.

We can see that SLP BER saturates (BER = 1) at lower SINR values than in the ZF case. The result is reproduced for every C_R.

FIGURE 7.10: LDPC BER plots for ZF and CF NNLS SLP vs the channel emulator SINR.

7.4.4 Frame Error Rate Performance of CF NNLS SLP

In Fig. 7.11 we show the LDPC frame error rate using QPSK constellation. The total length of an LDPC blocks with payload and parity check bits is 64800 bits. After the decoding process, the parity check bits are removed and the payload is transferred into the FER calculator. BCH (Bose-Chaudhuri-Hocquenghem) code is applied to correct the residual errors. Each point is an average of 1 million blocks. The FER curves are plotted against the channel emulator SINR as in the case of BER benchmarks. We can see that SLP FER saturates (FER = 1) at lower SINR values than in the ZF case. The result is reproduced for every C_R.
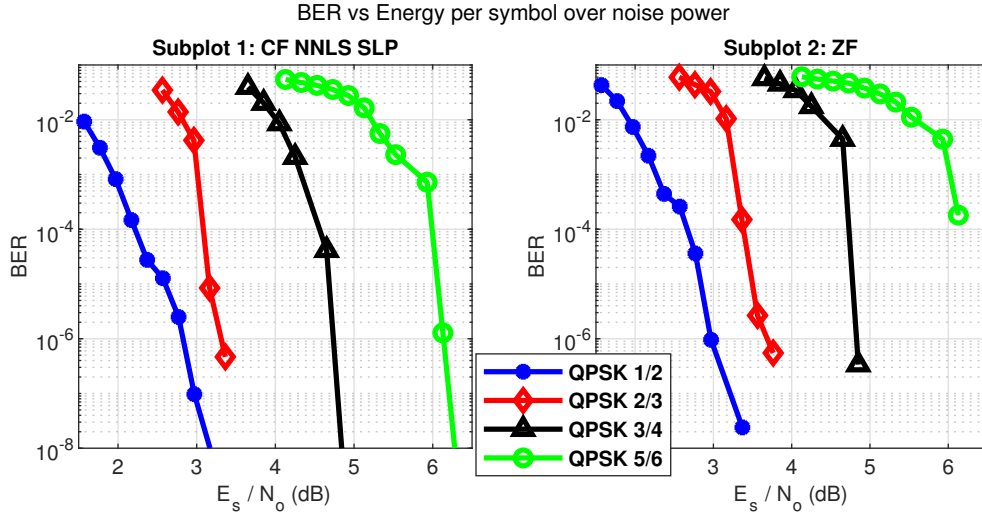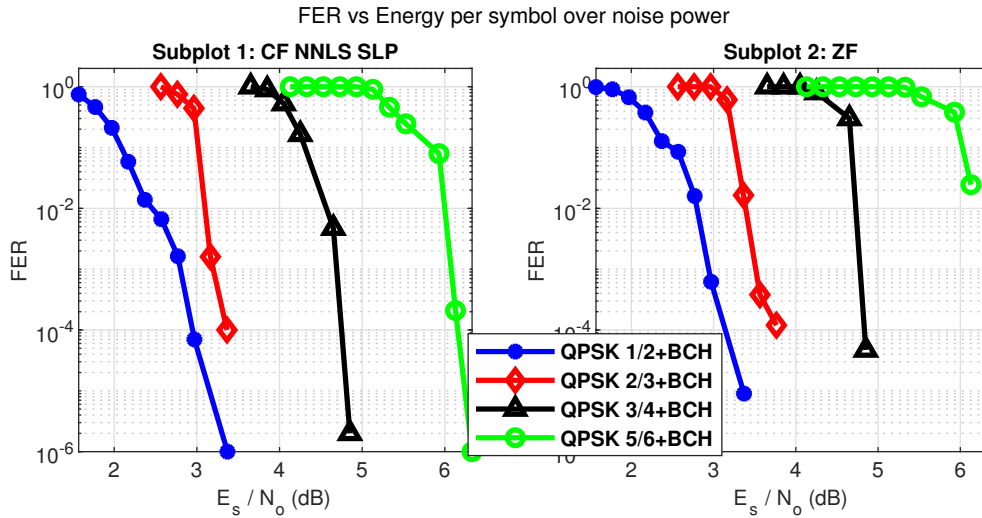

FIGURE 7.11: LDPC FER plots for ZF and CF NNLS SLP vs the expected SINR.

7.4.5 Spectral Efficiency of CF NNLS SLP

Spectral efficiency can be expressed as:

$$SE = \frac{R_b}{B_w}(1 - FER)\left(\frac{\text{b/s}}{\text{Hz}}\right),$$ (7.9)

where payload bit rate is:

$$R_b = \log_2(M)R_s C_R (b/s),$$ (7.10)

and the signal bandwidth is:

$$B_w = \frac{1}{T_s}(\beta + 1)(\text{Hz}).$$ (7.11)

Given that the symbol period and the symbol rate are related as $T_s = \frac{1}{R_s}(s)$, for QPSK modulation order is $M = 4$, and the matched filter roll-off factor is $\beta = 0.2$, we substitute eq. (7.10) and (7.11) back to eq. (7.9) and get the final expression for the spectral efficiency:

$$SE = \frac{2C_R}{(0.2 + 1)}(1 - FER)\left(\frac{\text{b/s}}{\text{Hz}}\right)$$ (7.12)

In Fig. 7.12 we can see the spectral efficiency of the ZF and SLP techniques vs SINR. We can see that SLP saturates at the maximum spectral efficiency at lower SINR values than ZF. In the case of the C_R 1/2 SLP achieves the maximum SE at 2.2 dB, for C_R 2/3 - 3.1 dB, C_R 3/4 - 4.5 dB, and C_R 5/6 - 6 dB. We can see that SLP has a consistent advantage in SE over ZF. We can see that SLP modified symbols can be correctly decoded by a receiver which has no prior knowledge of the modifications in the symbols of the conventional QPSK constellation. Additionally, these modifications result in lower BER and FER as well improves SE.
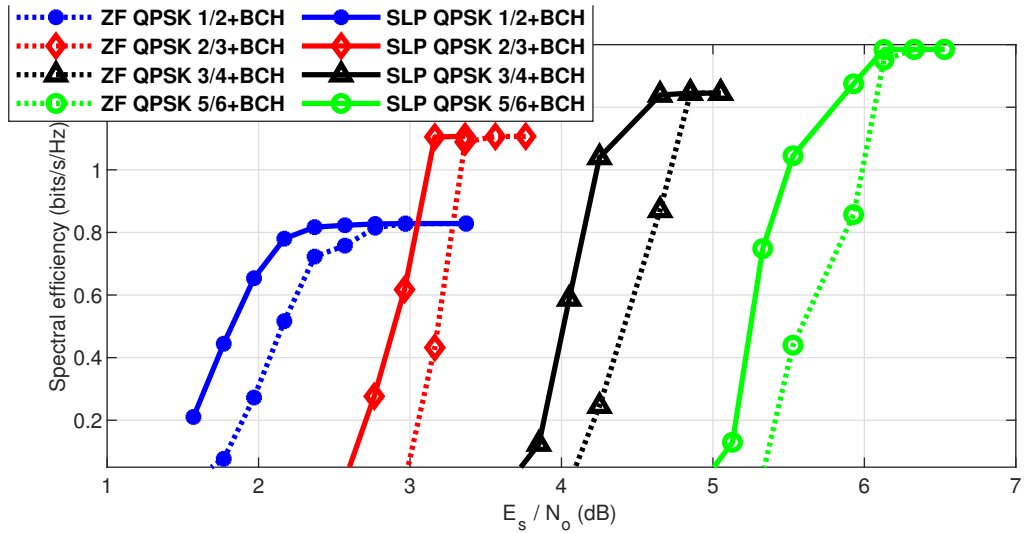
FIGURE 7.12: Experimental spectral efficiency plots for ZF and CF NNLS SLP vs the expected SINR.

7.5 Summary

In this chapter, we experimentally demonstrated that SLP can improve received signal quality in terms of SINR and Spectral efficiency then compared to ZF precoding. We showed that the design of the receiver does not need prior modifications to correctly decode symbols, modified by the SLP technique. We used the conventional LLR and LDPC decoder to extract the information bits from the symbols. SLP achieves higher spectral efficiency and lower FER at the same noise power introduced by the channel emulator. At the same, the SLP transmits power remains lower than for ZF. On another hand, we discovered, that the SNORE algorithm tends to underestimate or overestimate SNR values due to modified pilot symbols by the SLP. This can be avoided if the SLP techniques are not applied towards the transmitted pilot symbols at the gateway.

Chapter 8

In-lab Validation of M-QAM Symbol-Level Precoding

In this chapter, we demonstrate theoretically and experimentally the benefits of the precoder in terms of energy and computationally efficiency for M-QAM constellations. Towards this objective, we more thoroughly describe the practical implementation aspects of the hardware demonstrator, which consists of: a MIMO transmitter with the capability to perform real-time SLP algorithm, a MIMO channel emulator, and a set of receivers with CSI estimation capabilities. We estimate the optimal use cases of the SLP precoder in such a system.

We demonstrate an important connection between the condition number of the MIMO channel matrix and the performance of the SLP technique. The results show, that the SLP can perform better than ZF at the particular channel matrix conditions, while for some channel matrices the performance of ZF and the SLP is the same.

We present practical issues and their solutions towards utilizing the SLP techniques on the receiver side. We discuss the impact of the SLP precoding algorithm on the symbol constellation and synchronization and demodulation issues with a conventional receiver, which influence the actual Quality of Service.

8.1 Symbol-Level Precoding Design

8.1.1 System Model

The general system model focuses on the forward link of a multi-antenna system, which aims at reusing the total available bandwidth among all beams of the coverage. We define the number of transmitting antenna elements as N_t and the total number of users as N_u in the coverage area. In the specified MIMO channel model, the received signal at the i-th user is $y_i = \mathbf{h}_i^\dagger \mathbf{x} + n_i$, where $\mathbf{h}_i^\dagger$ is a $1 \times N_t$ vector representing the complex channel coefficients between the i-th user and the N_t antennas of the transmitter, $\mathbf{x}$ is defined as the $N_t \times 1$ vector of the transmitted symbols at a certain symbol period and n_i is the independent complex circularly-symmetric (c.c.s.) independent identically distributed (i.i.d) zero mean Additive White Gaussian Noise (AWGN) measured at the i-th user's receive antenna. We assuming a system having $N_t = N_u = N$, which is the present case. Looking at the general formulation of the received signal, which includes the whole set of users, the linear signal model is:

$$\mathbf{y} = \mathbf{H}\mathbf{x} + \mathbf{n} = \mathbf{H}\mathbf{W}\mathbf{s} + \mathbf{n} \qquad (8.1)$$

In this scenario, we define the linear precoding matrix $\mathbf{W} \in \mathbb{C}^{N \times N}$ which maps information symbols $\mathbf{s}$ into precoded symbols $\mathbf{x}$.

8.1.2 Precoding technique

We implemented the symbol-level precoding technique (CF SLP) presented in Chapter 4 into the demonstrator among side the Zero-Forcing technique [40]. The essential difference from the ZF precoding method is the optimization vector $\mathbf{u} \in \mathbb{C}^N$, which is recalculated per every symbol set $\mathbf{s}$ to construct optimal precoded signal as

$$\mathbf{x} = \mathbf{W}_{\text{ZF}}(\sqrt{\gamma}\mathbf{s} + \mathbf{u}), \tag{8.2}$$

where $\mathbf{W}_{\text{ZF}} = \hat{\mathbf{H}}^H \cdot (\hat{\mathbf{H}} \cdot \hat{\mathbf{H}}^H)^{-1}$ is a Zero-Forcing precoding matrix, $\hat{\mathbf{H}} \in \mathbb{C}^{N \times N}$ - a channel matrix estimated from CSI and $\sqrt{\gamma}$ - the SNR requirement. The vector $\mathbf{u}$ adds a positive excursion to the user symbols $\mathbf{s}$. The excursion is always increasing the amplitude of the symbols. It is calculated for each set of symbols to increase SNR at the receiver side due to optimally preserved constructive interference components, which occur in the MIMO channel. This effect decreases the total power of the precoded transmission signal $\mathbf{x}$ at the transmitter side. We define a convex optimization problem to minimize $\|\mathbf{x}\|_2$ with the SNR constrain as

$$\begin{aligned} \min_{\mathbf{u}} &\|\mathbf{x}\|_2 \\ \text{s. t.} &|\mathbf{y}| \geq |\mathbf{s}| \end{aligned}, \tag{8.3}$$

for $\mathbf{H}\mathbf{W}_{\text{ZF}} = \mathbf{I}$ and $\mathbf{n} = \mathbf{0}$. It was shown in [100], that the problem (8.3) can be transformed into a non-negative least squares (NNLS) problem as

$$\begin{aligned} \min_{\tilde{\mathbf{u}}} &\quad \|\widetilde{\mathbf{W}}_{\text{ZF}}\mathbf{B}\tilde{\mathbf{u}} - \mathbf{d}\|_2 \\ \text{subject to} &\quad \tilde{\mathbf{u}} \geq 0 \end{aligned}, \tag{8.4}$$

where $\mathbf{d} = -\widetilde{\mathbf{W}}_{\text{ZF}}(\sqrt{\gamma}\tilde{\mathbf{s}})$, $\widetilde{\mathbf{W}} = [\text{Re}(\mathbf{W}_{\text{ZF}}), -\text{Im}(\mathbf{W}_{\text{ZF}}); \text{Im}(\mathbf{W}_{\text{ZF}}), \text{Re}(\mathbf{W}_{\text{ZF}})]$, $\tilde{\mathbf{s}} = [\text{Re}(\mathbf{s}^T), \text{Im}(\mathbf{s}^T)]^T$, $\tilde{\mathbf{u}} = [\text{Re}(\mathbf{u}^T), \text{Im}(\mathbf{u}^T)]^T$, and $\mathbf{B}$ is defined as in (4.8).

If there is no solutions for a particular channel matrix, then $\mathbf{u} = \mathbf{0}$ and symbol-level precoding (8.2) turns into the Zero-Forcing precoding as

$$\mathbf{x}_{zf} = \mathbf{W}_{\text{ZF}}\mathbf{s}. \tag{8.5}$$

Therefore, the minimal performance of the proposed precoding technique is expected at the level of the Zero-Forcing method in a statistically averaged CSI data. If at least one element of the optimization vector $\mathbf{u}$ is non-zero, then user symbols with an excursion can be constructed to minimize the power of the precoded signal so that ($\|\mathbf{x}\|_2 < \|\mathbf{x}_{zf}\|_2$).

8.1.3 Impact of the proposed SLP on constellation

Following the previous discussion of the CF SLP algorithm, Figure 8.1 shows how one symbol of the QPSK constellation can have an amplitude excursion in the positive quadrant space due to the presented optimization vector $\mathbf{u}$. Here we obtain a theoretical BER expression assuming that the receiver recovers perfectly the phase of the reference symbols. This phase recovery may be approached in a realistic scenario using repetitive pilot symbols (precoded or not) which are not modified. Also, an accurate synchronization can be maintained if modified
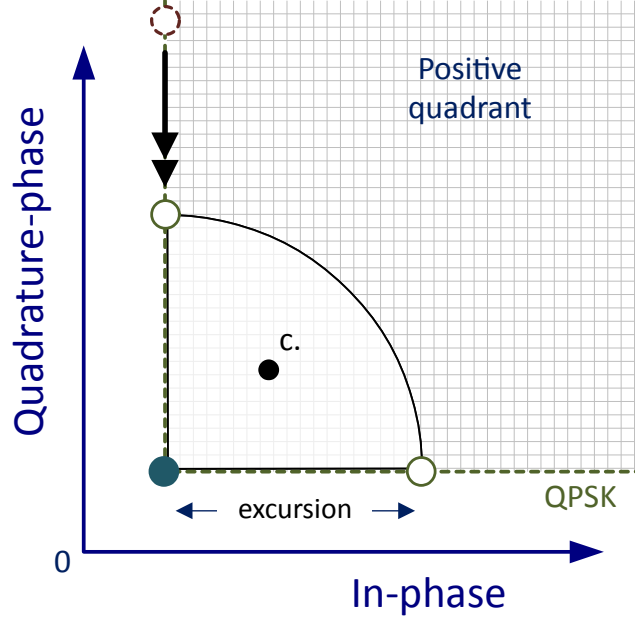
FIGURE 8.1: Symbol excursion in CF SLP in the vertical or horizontal axis.

symbols have on average the same phase of the mapping symbols. We reach such a condition by defining the excursion ratio of the mapping symbol as $\epsilon = \mathrm{Re}(u_i)/\mathrm{Re}(s_i)$ for $i = 1, \ldots, N$. The excursion ratio limits the maximum value of $\mathbf{u}$ with respect to the magnitude of the constellation symbols $\mathbf{s}$. For the particular case of a symbol of a QPSK modulation, the BER is $p_{\mathbf{es}} = 0.5(\mathcal{Q}(\sqrt{\gamma}) + \mathcal{Q}(\sqrt{\gamma}(1+\epsilon)))$ where $\mathcal{Q}(\cdot)$ is the standard Gaussian complementary cumulative distribution function, and γ is the SNR, where we assume that the received signal is affected by an additive zero-mean circularly-symmetric complex Gaussian noise. The ensemble BER is computed to be $0.75\mathcal{Q}(\sqrt{\gamma}) + 0.25\mathcal{Q}(\sqrt{\gamma}(1+\epsilon))$, under the assumption that all symbols have the same probability and half of the symbols have the same amplitude excursion in one dimension and the other half do not have any excursions.

8.2 Numerical Simulation

8.2.1 Benchmark System Parameters

We evaluate the performance of the proposed technique and compare it to other benchmark precoding methods, namely ZF and MMSE. We generate 2×2 MIMO channel matrix with a specific 2-norm matrix condition number defined as

$$\kappa_2(\mathbf{H}) = ||\mathbf{H}||_2 \cdot ||\mathbf{H^{-1}}||_2, \tag{8.6}$$

and injected the AWGN noise. The 2-norm corresponds to the ratio of the largest singular value of that matrix to the smallest singular value. By varying 2-norm from low to high values, we perform the benchmark with the channel matrices conditioned from a close-to-diagonal to a close-to-singular and increasing the power imbalance in the channel. The corresponding benchmark measurements for all the techniques performed using the same channel matrix generation.

8.2.2   Simulated Bit Error Rate Performance of CF SLP

Figures 8.2 and 8.3 show the theoretical BER performance of the CF SLP compared to ZF and MMSE techniques. The BER values at each SNR value is averaged over 10^6 samples. The CF SLP performs better than ZF in terms of improved BER. The advantage of CF SLP over ZF becomes more prominent with the increasing condition number of the channel matrix. In this case, the CF SLP technique generates the user symbols with even higher excursion which results in lower BER values (Figure 8.3). It is noticeable, that CF SLP benchmarks at lower BER than ZF in the whole range of the E_b/N_0 and lower than MMSE techniques for E_b/N_0 higher than 0 dB.

FIGURE 8.2: Simulated BER values averaged over 10^6 samples for ZF, MMSE and CF SLP compared to the theoretical QPSK BER curve. The perfect compensation of the phase rotation at the receiver is considered. The condition number of the channel matrix is 3.
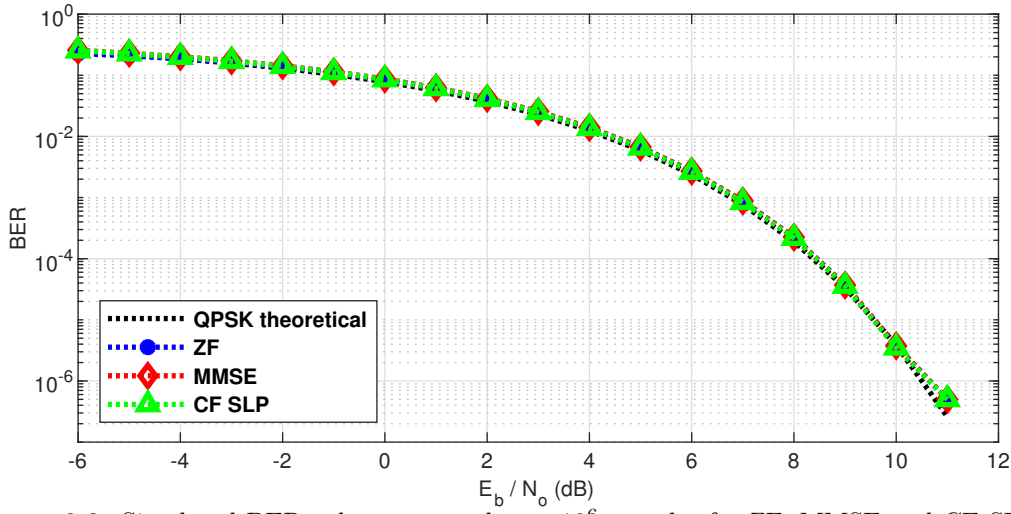

FIGURE 8.3: Simulated BER values averaged over 10^6 samples for ZF, MMSE and CF SLP compared to the theoretical QPSK BER curve. The perfect compensation of the phase rotation at the receiver is considered. The condition number of the channel matrix is 6.
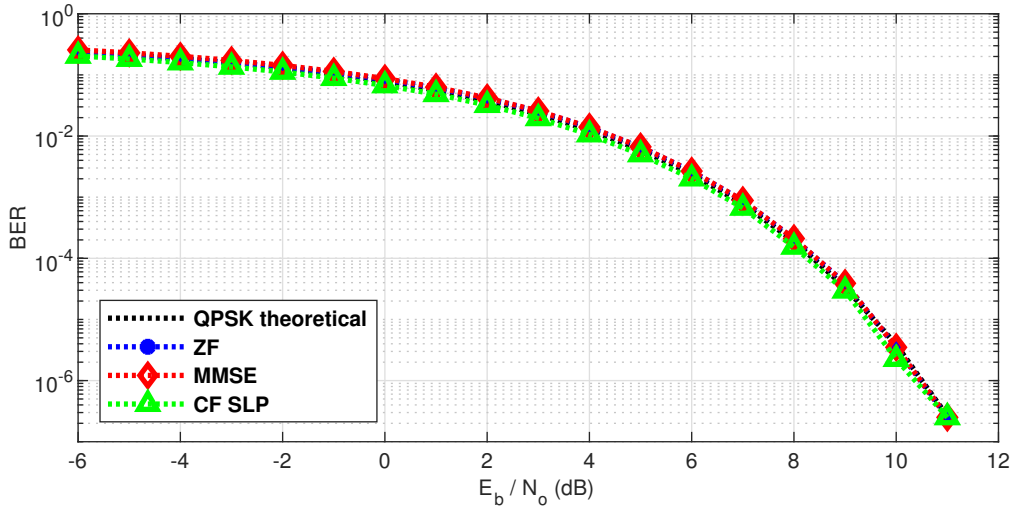
8.2.3   Simulated Total Consumed Power of CF SLP

Table 8.1 shows the difference between the total average power of the precoded symbols generated using ZF and CF SLP algorithms. We can see that with the higher channel matrix condition number we generate less total power using the CF SLP algorithm. At the same time, we observe an improved Quality of Service over the ZF as we saw in the previous section. At the greater condition number of the channel matrix, the power unbalance at the receivers is higher. The interfering signal can be higher in power than the useful signal for one of the receivers. The occurring inter-user interference can be both constructive and destructive toward the useful signal. The CF SLP technique does not cancel the components of constructive interference, which provide additional excursion of the mapping symbols and push the symbols deeper into their detection region providing higher BER score. The ZF cancels all the components of interference to have constant mapping symbols, and therefore requires more energy at the transmitter than the CF SLP.

TABLE 8.1: Reduction of the total average power of the precoded symbols in 2×2 MIMO system by CF SLP.

Matrix condition number	Power reduction
2.5	0.03 dB
3	0.04 dB
3.5	0.07 dB
4	0.09 dB
5	0.35 dB
6	0.72 dB
8	0.88 dB

8.3   Experimental Validation

8.3.1   Symbol-Level Optimized Precoding Evaluation

We use the aforementioned experimental environment to benchmark the optimized symbol-level precoding technique. We generate a set of random channel matrices $\mathbf{H}$ with unitary matrix F-norm, defined by $||\mathbf{H}||_{\mathbf{F}} = \mathrm{trace}(\mathbf{H}^H \mathbf{H})$, and for different matrix conditioning numbers, defined by 8.6.

For each channel matrix generation, we apply the CF SLP and compare the results to conventional channel-inversion ZF precoding. In both cases, we normalize the precoding matrix to have a unitary 2-norm, so that we obtain a constant value for the expectancy of transmitted power per antenna. Under these constraints, we measured the power in the two receivers and compare the results for different channel realizations for a set of channel matrix conditioning numbers between 2.5 and 4, as is shown in Figures 8.4 and 8.5. It is worth noting that in both cases ZF and CF SLP we use the same channel inversion matrix.
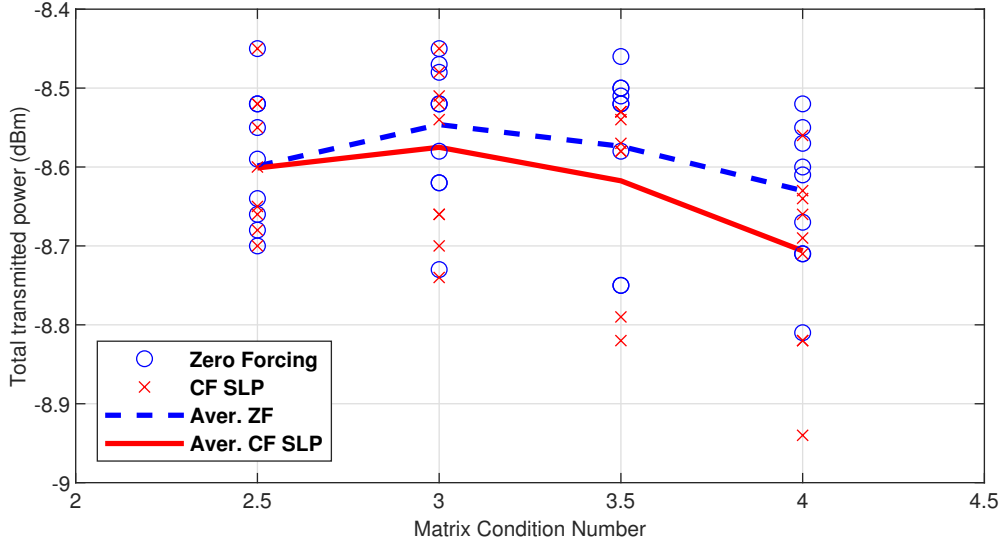
FIGURE 8.4: Different realizations of the total transmitted power on 2 output antenna ports, for conventional ZF and CF SLP.

We see in Figure 8.4 that the Zero-Forcing technique generates a signal with a higher averaged total transmitted power than the CF SLP technique. The reduction of the transmitted power by CF SLP is increasing as the matrix condition number increases comparing to ZF. The magnitudes of the power reduction very closely match the theoretically values from Table 8.1. By enabling the CF SLP the total power is reduced by 0.03 dB (theoretical - 0.04 dB) at the condition number 3 and by 0.07 dB (theoretical - 0.09 dB) at the condition number 4.
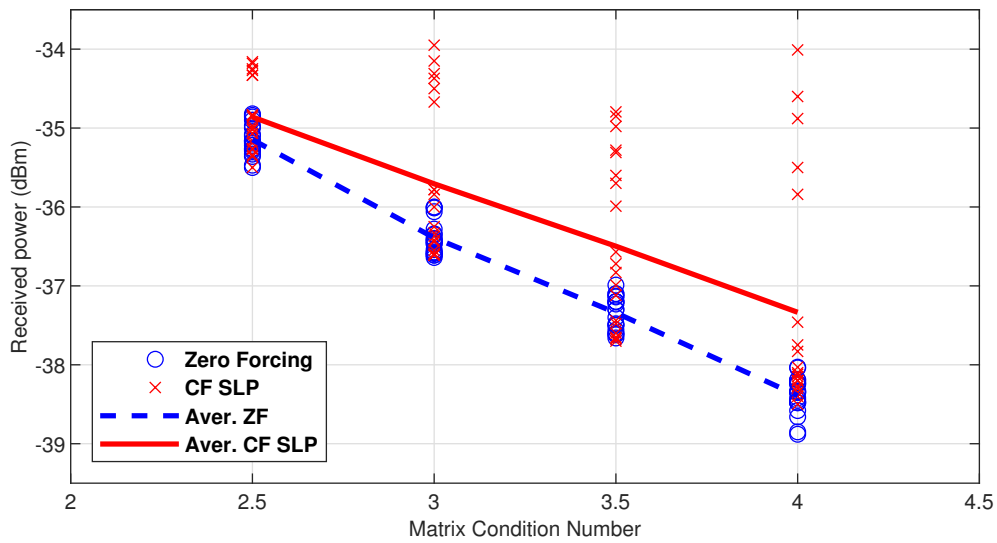

FIGURE 8.5: Different realizations of detected power, in 2 receivers indistinctly, for conventional ZF and CF SLP.

From Figure 8.5 we can observe that the received power for ZF precoding is not a constant for a given conditioning number as should be expected from the theory. These variations come from the imperfections in the actual hardware implementation. Some of these imperfections are the limited accuracy in the CSI estimation and its quantization error. Nevertheless, these imperfections have the same impact on the ZF and the CF SLP, we can observe that the CF SLP has gains in the received power. These gains become more frequent as the matrix conditioning number is increased. There are particular channel realizations in which the CF SLP performs the same as ZF for both receivers and other realizations in which the optimized symbol is only produced for one of the receivers. Up to this point, we have observed the gains in received power for CF SLP. In the following, we will observe how this gain is translated into BER performance in the receiver.

8.3.2 Uncoded Bit Error Performance of CF SLP

Figure 8.6 shows an example of received modified constellation with the CF SLP algorithm with some AWGN already applied. The symbol excursion will help for the cases in which the phase is correctly recovered and also for very low SNR conditions in which the received signal is very affected by additive noise.
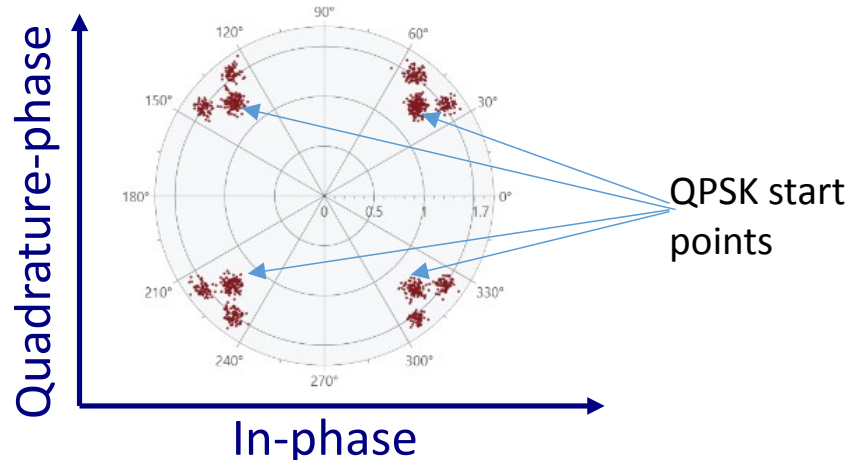
FIGURE 8.6: Received symbols modified by CF SLP.

The SNR is set by injecting of artificial AWGN in the channel emulator. The noise power can be accurately controlled to adjust the desired SNR, knowing the exact value of the received signal power. First, we performed a single link BER measurement using an unmodified QPSK constellation. We use it as a reference to evaluate the effects of imperfect phase synchronization for low SNR values. The phase-locked loop of the demodulator is reset for every frame. For the case of CF SLP, the precoded pilot symbols are not modified from the QPSK original mapping points.

We performed measurements of BER for ZF and CF SLP for different channel matrices, where the SNR was estimated using ZF precoding. This is a fair comparison, since, despite the average received power can increase while using CF SLP, minimal received power can still match the one gained with ZF precoding for some symbols. Figure 8.7 shows the theoretical ideal QPSK BER values, the BER for a single non-interference link, and the BER for ZF and

CF SLP for a particular matrix with conditioning number 2.5 which gives and excursion (in the horizontal and vertical axis) of 4%.

FIGURE 8.7: Experimental BER plots for ZF and CF SLP compared to an experimental baseline non-interference QPSK BER and to the theoretical BER curve. The matrix condition for the precoded channel is 2.5. The CF SLP in this case provides an excursion of 4.

Here we see a degradation of the BER which use precoding compared to the single link BER curve. This may occur due to inaccurate CSI estimati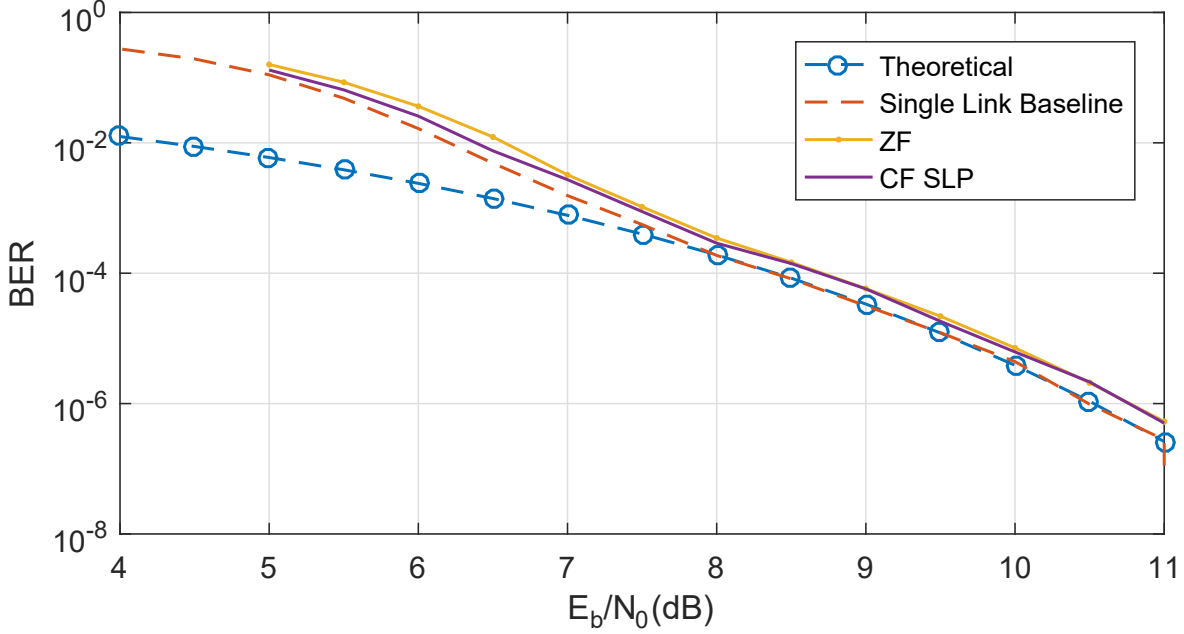on, which results in residual interference and affects the BER performance. However, the case of precoded signals, we obtain twice spectral efficiency since the system provides two separate streams using the same frequency band. We showed that the CF SLP performs better than ZF for low SNR values and that the ZF performs better at some points of higher SNR values using a conventional receiver. The experiment is repeated with some channel matrices with higher proposed excursion values, which in some cases gives a degradation in BER performance for high SNR values. Most of these errors are due to the lack of phase synchronization and phase tracking. These effects can be observed as a rotated shaking in the constellation plots in the graphical user interface at the receiver.

It is worth clarifying that, at the transmitter, the QPSK modulator maps the transmitted symbols in correspondence to optimization excursion from the CF SLP. However, at the receiver QPSK demodulator normalizes the received symbols in correspondence to the conventional QPSK symbol constellations.

Figure 8.8 shows the BER curves for ZF and CF SLP for a particular matrix with a conditioning number of 3 which gives and excursion (in the horizontal and vertical axis) of 20%. Here we can observe how the CF SLP scores lower BER than the conventional ZF for E_b/N_0 values lower than 8 dB.
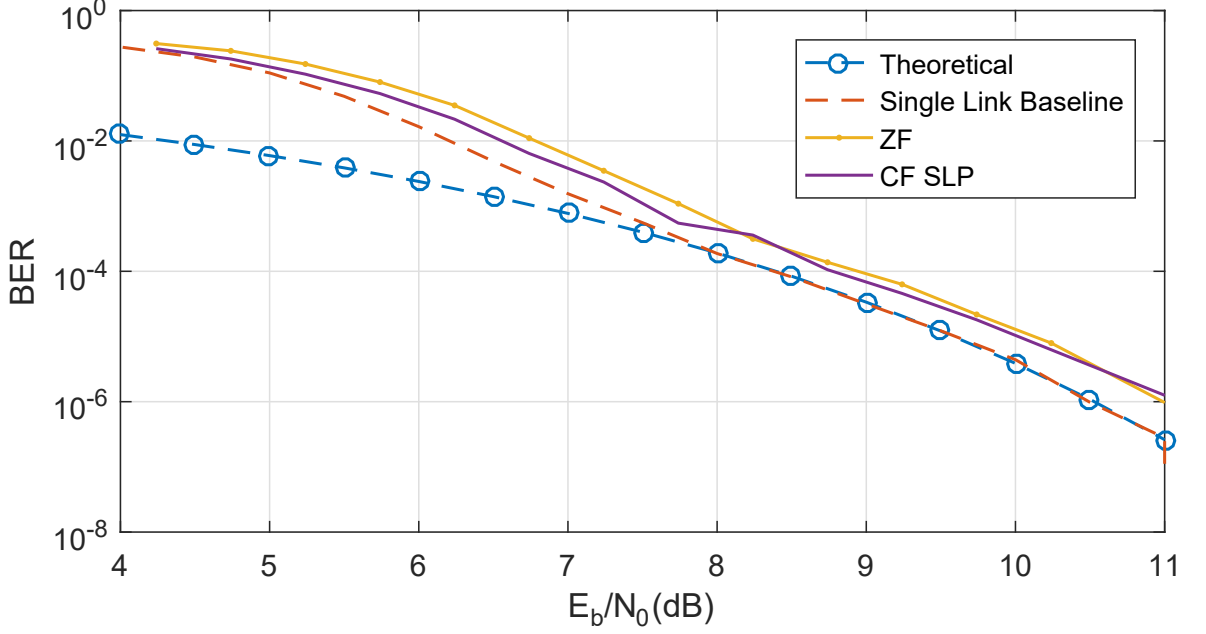
FIGURE 8.8: Experimental BER plots for ZF and CF SLP compared to an experimental baseline QPSK BER and the theoretical BER curve. The matrix condition number for the precoded channel is 3 The CF SLP in this case provides an excursion of 20%.

8.4 Summary

In this chapter, we presented the theoretical and experimental results using the hardware demonstration of precoded satellite communications based on state-of-art SLP technique. The SLP beamforming benchmarked similar BER results to ZF beamforming in the case scenario of high SNR. However, it is experimentally proven that the CF SLP technique takes advantage of unbalanced channel matrices with strong interference components to increase received signal SNR, improve service quality, and minimize the transmit power at the gateway.

Therefore, we showed that the SLP technique can provide better SNR performance than the conventional ZF technique in real-time transmissions for low SNR scenarios. The theoretical simulation data predicted improvement of the BER performance for high SNR scenarios. However, a decrease in the BER performance was observed in the experimental data. This performance decrease, which is generated by an imperfection in the carrier synchronization, and tracking can be avoided if global synchronization is achieved. Some examples of this are the multi-carrier or OFDM systems in which many carriers are jointly synchronized and aided by additional synchronization carrier pilots. Another example in which this method can be applied is in the low SNR regimes of single-carrier communications, which maintain phase coherency along time, such as the satellite communication standards as DVB-S2X, where the receiver synchronization is improved over longer averaging periods. Besides, the improvements for the evaluated method will increase with higher-order MIMO systems, where the gains obtained from the symbol-level optimization can increase.

We demonstrated, that the condition number of the channel matrix has an impact on the performance of the CF SLP technique in theoretical and experimental benchmarks. At the larger condition number of the channel matrix, the power unbalance at the receivers is

higher, which enables the CF SLP technique to exploit occurring constructive interference between the users. We show experimentally the feasibility of the proposed SLP in terms of complexity and energy efficiency.

Chapter 9

Conclusions and Future Works

9.1 Main Conclusion

In this thesis, we worked on the computationally and energy-efficient SLP for the sum power minimization for M-APSK and M-QAM modulated waveforms. We developed the closed-form algorithms for real-time SLP operation. The closed-form algorithm has an asymptotic complexity of $O(N^2)$ and has a significantly faster processing time in comparison to other optimization algorithms (Fast NNLS and CVX) for convex quadratic optimization problems. The closed-form algorithm provides a trade-off between the increased sum power and much faster processing time. The efficient processing time and low complexity of the algorithm are essential in the real-time transmission systems with very short symbol periods like DVB-S2X and millimeter-wave communications.

We implemented the closed-form algorithm in the in-lab hardware demonstrator for precoding in DVB-S2X systems. The hardware demonstrator is a full-chain closed-loop communication system with a multi-beam gateway transmitter, MIMO channel emulator, and user terminals with real-time CSI estimation and feedback. With the hardware demonstrator, we were able to experimentally show demonstrated the application of the conventional linear precoding and SLP in realistic satellite communications based on the DVB-S2X standard. For the in-lab demonstration, we implemented the closed-form SLP into the FPGA platform. We optimized the design of the FPGA code to operate at up to 83 MSymbols per second throughput per each receiver terminal with up to 20 simultaneously operating terminal units while utilizing a reasonable amount of the FPGA resources. The designed HDL core universally supports single- and multi-level symbol modulations with fixed-phase optimization. It can directly operate with any M-PSK and M-APSK constellation and does not need to reconfigure. The approximate closed-form algorithm, which we developed for the FPGA design, demonstrated a 2 dB loss of energy efficiency during the conducted benchmarks against conventional Fast NNLS and CVX optimization algorithms. We also measured an additional 1 dB loss of energy efficiency of the approximate closed-form algorithm when deployed on an actual FPGA platform. Finally, we were able to experimentally demonstrate that SLP can improve received signal quality in terms of SINR and Spectral efficiency then compared to ZF precoding. We showed that the design of the receiver does not need prior modifications to correctly decode symbols, modified by the SLP technique. We used the conventional LLR and LDPC decoder to extract the information bits from the symbols. SLP achieves higher spectrum efficiency and lower FER at the same noise power introduced by the channel

emulator. At the same, the SLP transmitting power remains lower than for ZF.

9.2 Future Works

Although the results presented in this thesis have demonstrated the effectiveness of the proposed designs and optimization methods for SLP communications, many opportunities for extending the scope of this thesis remain open. This section discusses some of the topics that we consider particularly interesting for extension and new problems.

Hereby, we name several possible extensions:

- **Enhance pilots and SINR estimation for ACM with SLP**: It was shown that the conventional algorithm for SINR estimation treats symbols, which are modified by SLP, as a source of interference. Thus, the SINR is underestimated in such cases, which will affect the adaptive coding and modulation (ACM) selection.

- **Enhance LLR calculation**: The current LLR calculation can be improved for SLP symbols for further improve FEC. Currently, LLR distances are calculated between received symbols and expected symbol points. Improved performance is expected if LLR distances are calculated between the received symbols and constructive interference regions of expected symbols.

- **Perform over-the-air precoding**: The current in-lab test-bed is suitable for over-the-air (OTA) precoding validations. We plan to set up a 2 by 2 test-bed using an actual multi-beam satellite link. The OTA test-bed will provide more accurate precoding performance analysis and help to facilitate the adoption of the technology in the industry.

Bibliography

[1] Full5G project and the 5G Infrastructure Association, *Full 5G Annual Journal 2020*. Montpellier, France: IDATE DigiWorld, 2020.

[2] (2013) METIS: Scenarios, Requirements and KPIs for 5G Mobile and Wireless System, Deliverable D1.1, ICT-317669-METIS/D1.1. [Online]. Available: https://cordis.europa.eu/docs/projects/cnect/9/317669/080/deliverables/001-METISD11v1pdf.pdf

[3] B. Evans, O. Onireti, T. Spathopoulos, and M. A. Imran, "The Role of Satellites in 5G," in *2015 23rd European Signal Processing Conference (EUSIPCO)*, Aug 2015, pp. 2756–2760.

[4] S. Chatzinotas, B. Ottersten, and R. De Gaudenzi, *Cooperative and Cognitive Satellite Systems*, 1st ed. Orlando, FL, USA: Academic Press, Inc., 2015.

[5] D. Christopoulos, "Multibeam Joint Processing in Satellite Communications," PhD Thesis, University of Luxembourg, 2014. [Online]. Available: https://orbilu.uni.lu/handle/10993/21721

[6] A. Kalantari, "Signal Processing for Physical Layer Security With Application in Satellite Communications," PhD Thesis, University of Luxembourg, 2016. [Online]. Available: https://orbilu.uni.lu/handle/10993/27631

[7] M. Alodeh, "Interference in Multiple-antenna Communications: From Channel Estimation to Exploitation," PhD Thesis, University of Luxembourg, 2015. [Online]. Available: https://orbilu.uni.lu/handle/10993/24346

[8] D. Spano, "Advanced Symbol-level Precoding Schemes for Interference Exploitation in Multi-antenna Multi-user Wireless Communications," PhD Thesis, University of Luxembourg, 2018. [Online]. Available: https://orbilu.uni.lu/handle/10993/36227

[9] S. Domouchtsidis, "Symbol Level Precoding Techniques for Hardware and Power Efficient Wireless Transceivers," PhD Thesis, University of Luxembourg, 2020.

[10] T. Weber, A. Sklavos, and M. Meurer, "Imperfect Channel-State Information in MIMO Transmission," *IEEE Transactions on Communications*, vol. 54, no. 3, pp. 543–552, March 2006.

[11] E. Lagunas, S. Andrenacci, S. Chatzinotas, and B. Ottersten, "Cross-Layer Forward Packet Scheduling for Emerging Precoded Broadband Multibeam Satellite System,"

in *2018 9th Advanced Satellite Multimedia Systems Conference and the 15th Signal Processing for Space Communications Workshop (ASMS/SPSC)*, Berlin, Germany, Sep. 2018, pp. 1–8.

[12] Z. An, G. Song, and H. Chen, "Open-Loop Precoding Scheme for Multi-Beam Mobile Satellite Communication Systems," in *2018 IEEE 4th International Conference on Computer and Communications (ICCC)*, Chengdu, China, Dec 2018, pp. 795–799.

[13] A. Haqiqatnejad, F. Kayhan, and B. Ottersten, "An Approximate Solution for Symbol-Level Multiuser Precoding Using Support Recovery," in *2019 IEEE 20th International Workshop on Signal Processing Advances in Wireless Communications (SPAWC)*, Cannes, France, July 2019, pp. 1–5.

[14] C. G. Tsinos, A. Kalantari, S. Chatzinotas, and B. Ottersten, "Symbol-Level Precoding with Low Resolution DACs for Large-Scale Array MU-MIMO Systems," in *2018 IEEE 19th International Workshop on Signal Processing Advances in Wireless Communications (SPAWC)*, Kalamata, Greece, June 2018, pp. 1–5.

[15] M. Heed, "The ERIEYE Phased Array Antenna from a Systems Viewpoint," in *2000 IEEE International Conference on Phased Array Systems and Technology (Cat. No.00TH8510)*, Dana Point, CA, USA, May 2000, pp. 391–394.

[16] E. Brookner, "Phased Arrays for the New Millennium," in *IEEE International Symposium on Phased Array Systems and Technology, 2003.*, Oct 2003, pp. 617–.

[17] S. Harput and A. Bozkurt, "Ultrasonic Phased Array Device for Acoustic Imaging in Air," *IEEE Sensors Journal*, vol. 8, no. 11, pp. 1755–1762, Nov 2008.

[18] K. Higuchi, K. Suzuki, and H. Tanigawa, "Ultrasonic Phased Array Transducer for Acoustic Imaging in Air," in *IEEE 1986 Ultrasonics Symposium*, Williamsburg, VA, USA, Nov 1986, pp. 559–562.

[19] S. Kashyap, E. Björnson, and E. G. Larsson, "Can Wireless Power Transfer Benefit from Large Transmitter Arrays?" in *2015 IEEE Wireless Power Transfer Conference (WPTC)*, Boulder, CO, USA, May 2015.

[20] Y. Qian, X. Zhou, J. Li, F. Shu, and D. N. K. Jayakody, "A Novel Precoding and Impulsive Noise Mitigation Scheme for MIMO Power Line Communication Systems," *IEEE Systems Journal*, vol. 13, no. 1, pp. 6–17, March 2019.

[21] S. Neshvad, S. Chatzinotas, and J. Sachau, "Wideband Identification of Power Network Parameters Using Pseudo-Random Binary Sequences on Power Inverters," *IEEE Transactions on Smart Grid*, vol. 6, no. 5, pp. 2293–2301, Sept 2015.

[22] L. Liu, R. Zhang, and K. Chua, "Multi-Antenna Wireless Powered Communication With Energy Beamforming," *IEEE Transactions on Communications*, vol. 62, no. 12, pp. 4349–4361, Dec 2014.

[23] S. Gautam, "Design and Optimization Of Simultaneous Wireless Information and Power Transfer Systems," PhD Thesis, University of Luxembourg, 2020. [Online]. Available: https://orbilu.uni.lu/handle/10993/42673

[24] I. Binyamini and I. Bergel, "Adaptive Precoder Using Sign Error Feedback for FEXT Cancellation in Multichannel Downstream VDSL," *IEEE Transactions on Signal Processing*, vol. 61, no. 9, pp. 2383–2393, May 2013.

[25] R. B. Moraes, P. Tsiaflakis, J. Maes, and M. Moonen, "General Framework and Algorithm for Data Rate Maximization in DSL Networks," *IEEE Transactions on Communications*, vol. 62, no. 5, pp. 1691–1703, May 2014.

[26] C. A. Balanis, *Antenna Theory - Analysis and Design.* New York: John Wiley & Sons, 2016.

[27] M. Z. Win and J. H. Winters, "Analysis of Hybrid Selection/Maximal-ratio Combining in Rayleigh Fading," *IEEE Transactions on Communications*, vol. 47, no. 12, pp. 1773–1776, Dec 1999.

[28] B. Friedlander and S. Scherzer, "Beamforming Versus Transmit Diversity in the Downlink of a Cellular Communications System," *IEEE Transactions on Vehicular Technology*, vol. 53, no. 4, pp. 1023–1034, July 2004.

[29] S. M. Alamouti, "A Simple Transmit Diversity Technique for Wireless Communications," *IEEE Journal on Selected Areas in Communications*, vol. 16, no. 8, pp. 1451–1458, Oct 1998.

[30] M. Elkhodr and M. Elkhodr, *Enabling Technologies and Architectures for Next-Generation Networking Capabilities*, 1st ed. USA: IGI Global, 2018.

[31] W. Zeng, C. Xiao, M. Wang, and J. Lu, "Linear Precoding for Finite-Alphabet Inputs Over MIMO Fading Channels With Statistical CSI," *IEEE Transactions on Signal Processing*, vol. 60, no. 6, pp. 3134–3148, June 2012.

[32] N. Song, T. Yang, and M. Haardt, "Efficient Hybrid Space-Ground Precoding Techniques for Multi-Beam Satellite Systems," in *2017 IEEE International Conference on Acoustics, Speech and Signal Processing (ICASSP)*, March 2017, pp. 6284–6288.

[33] Q. H. Spencer, A. L. Swindlehurst, and M. Haardt, "Zero-Forcing Methods for Downlink Spatial Multiplexing in Multiuser MIMO Channels," *IEEE Transactions on Signal Processing*, vol. 52, no. 2, pp. 461–471, Feb 2004.

[34] X. Artiga, M. A. Vazquez, A. Perez-Neira, C. Tsinos, E. Lagunas, S. Chatzinotas, V. Ramireddy, C. Steinmetz, R. Zetik, K. Ntougias, D. Ntaikos, and C. B. Papadias, "Spectrum Sharing in Hybrid Terrestrial-Satellite Backhaul Networks in the Ka Band," in *2017 European Conference on Networks and Communications (EuCNC)*, June 2017, pp. 1–5.

[35] K. Roth, H. Pirzadeh, A. L. Swindlehurst, and J. A. Nossek, "A Comparison of Hybrid Beamforming and Digital Beamforming With Low-Resolution ADCs for Multiple Users and Imperfect CSI," *IEEE Journal of Selected Topics in Signal Processing*, vol. 12, no. 3, pp. 484–498, June 2018.

[36] A. G. Orozco-Lugo, M. M. Lara, and D. C. McLernon, "Channel Estimation Using Implicit Training," *IEEE Transactions on Signal Processing*, vol. 52, no. 1, pp. 240–254, Jan 2004.

[37] Q. T. Zhang, "Maximal-Ratio Combining Over Nakagami Fading Channels With An Arbitrary Branch Covariance Matrix," *IEEE Transactions on Vehicular Technology*, vol. 48, no. 4, pp. 1141–1150, July 1999.

[38] G. Caire and S. Shamai, "On Achievable Rates in a Multi-Antenna Gaussian Broadcast Channel," in *Proceedings. 2001 IEEE International Symposium on Information Theory (IEEE Cat. No.01CH37252)*, Washington, DC, USA, June 2001, pp. 147–.

[39] T. Haustein, C. von Helmolt, E. Jorswieck, V. Jungnickel, and V. Pohl, "Performance of MIMO Systems with Channel Inversion," in *Vehicular Technology Conference. IEEE 55th Vehicular Technology Conference. VTC Spring 2002 (Cat. No.02CH37367)*, vol. 1, Birmingham, AL, USA, May 2002, pp. 35–39 vol.1.

[40] C. B. Peel, B. M. Hochwald, and A. L. Swindlehurst, "A Vector-Perturbation Technique for Near-capacity Multiantenna Multiuser Communication Part I: Channel Inversion and Regularization," *IEEE Transactions on Communications*, vol. 53, no. 1, pp. 195–202, Jan 2005.

[41] X. Gao, O. Edfors, F. Rusek, and F. Tufvesson, "Linear Pre-Coding Performance in Measured Very-Large MIMO Channels," in *2011 IEEE Vehicular Technology Conference (VTC Fall)*, Sep. 2011, pp. 1–5.

[42] S. Shi and M. Schubert, "MMSE Transmit Optimization for Multi-User Multi-Antenna Systems," in *Proceedings. (ICASSP '05). IEEE International Conference on Acoustics, Speech, and Signal Processing, 2005.*, vol. 3, March 2005, pp. iii/409–iii/412 Vol. 3.

[43] E. Björnson, M. Bengtsson, and B. Ottersten, "Optimal Multiuser Transmit Beamforming: A Difficult Problem with a Simple Solution Structure [Lecture Notes]," *IEEE Signal Processing Magazine*, vol. 31, no. 4, pp. 142–148, July 2014.

[44] M. Alodeh, D. Spano, A. Kalantari, C. G. Tsinos, D. Christopoulos, S. Chatzinotas, and B. Ottersten, "Symbol-Level and Multicast Precoding for Multiuser Multiantenna Downlink: A State-of-the-Art, Classification, and Challenges," *IEEE Communications Surveys Tutorials*, vol. 20, no. 3, pp. 1733–1757, thirdquarter 2018.

[45] A. Müller, A. Kammoun, E. Björnson, and M. Debbah, "Efficient Linear Precoding for Massive MIMO Systems Using Truncated Polynomial Expansion," in *2014 IEEE 8th Sensor Array and Multichannel Signal Processing Workshop (SAM)*, June 2014, pp. 273–276.

[46] A. Kammoun, A. Müller, E. Björnson, and M. Debbah, "Linear Precoding Based on Polynomial Expansion: Large-Scale Multi-Cell MIMO Systems," *IEEE Journal of Selected Topics in Signal Processing*, vol. 8, no. 5, pp. 861–875, Oct 2014.

[47] N. Fatema, G. Hua, Y. Xiang, D. Peng, and I. Natgunanathan, "Massive MIMO Linear Precoding: A Survey," *IEEE Systems Journal*, vol. 12, no. 4, pp. 3920–3931, Dec 2018.

[48] A. Li, D. Spano, J. Krivochiza, S. Domouchtsidis, C. G. Tsinos, C. Masouros, S. Chatzinotas, Y. Li, B. Vucetic, and B. Ottersten, "A Tutorial on Interference Exploitation via Symbol-Level Precoding: Overview, State-of-the-Art and Future Directions," *IEEE Communications Surveys Tutorials*, vol. 22, no. 2, pp. 796–839, Secondquarter 2020.

[49] M. Alodeh, S. Chatzinotas, and B. Ottersten, "Symbol-Level Multiuser MISO Precoding for Multi-Level Adaptive Modulation," *IEEE Transactions on Wireless Communications*, vol. 16, no. 8, pp. 5511–5524, Aug 2017.

[50] D. Spano, M. Alodeh, S. Chatzinotas, and B. Ottersten, "Symbol-Level Precoding for the Nonlinear Multiuser MISO Downlink Channel," *IEEE Transactions on Signal Processing*, vol. 66, no. 5, pp. 1331–1345, March 2018.

[51] Y. I. Choi, J. W. Lee, C. G. Kang, and M. Rim, "Constructive Multi-User Interference for Symbol-Level Link Adaptation: MMSE Approach," in *2017 IEEE Globecom Workshops (GC Wkshps)*, Dec 2017, pp. 1–6.

[52] Y. C. B. Silva and A. Klein, "Linear Transmit Beamforming Techniques for the Multigroup Multicast Scenario," *IEEE Transactions on Vehicular Technology*, vol. 58, no. 8, pp. 4353–4367, Oct 2009.

[53] C. Masouros and E. Alsusa, "Dynamic Linear Precoding for the Exploitation of Known Interference in MIMO Broadcast Systems," *IEEE Transactions on Wireless Communications*, vol. 8, no. 3, pp. 1396–1404, March 2009.

[54] M. Alodeh, D. Spano, S. Chatzinotas, and B. Ottersten, "Faster-than-Nyquist Spatiotemporal Symbol-Level Precoding in the Downlink of Multiuser MISO Channels," in *2017 IEEE International Conference on Acoustics, Speech and Signal Processing (ICASSP)*, March 2017, pp. 3779–3783.

[55] C. Masouros and G. Zheng, "Exploiting Known Interference as Green Signal Power for Downlink Beamforming Optimization," *IEEE Transactions on Signal Processing*, vol. 63, no. 14, pp. 3628–3640, July 2015.

[56] D. Spano, M. Alodeh, S. Chatzinotas, J. Krause, and B. Ottersten, "Spatial PAPR Reduction in Symbol-Level Precoding for the Multi-Beam Satellite Downlink," in *2017 IEEE 18th International Workshop on Signal Processing Advances in Wireless Communications (SPAWC)*, July 2017, pp. 1–5.

[57] D. Spano, M. Alodeh, S. Chatzinotas, and B. Ottersten, "Papr Minimization Through Spatio-Temporal Symbol-Level Precoding for the Non-Linear Multi-User MISO Channel," in *2018 IEEE International Conference on Acoustics, Speech and Signal Processing (ICASSP)*, April 2018, pp. 3599–3603.

[58] M. Alodeh, D. Spano, S. Chatzinotas, and B. Ottersten, "Peak Power Minimization in Symbol-Level Precoding for Cognitive MISO Downlink Channels," in *2016 IEEE International Conference on Digital Signal Processing (DSP)*, Oct 2016, pp. 240–244.

[59] N. Mazzali, S. Boumard, J. Kinnunen, B. S. M. R., M. Kiviranta, and N. Alagha, "Enhancing Mobile Services with DVB-S2X Superframing," *International Journal of Satellite Communications and Networking*, vol. 0, no. 0.

[60] S. Jiang, F. Gong, and X. Chen, "A Low-Complexity Soft Demapper for 128APSK of DVB-S2X," in *2016 8th International Conference on Wireless Communications Signal Processing (WCSP)*, Oct 2016, pp. 1–4.

[61] J. Lucciardi, P. Potier, G. Buscarlet, F. Barrami, and G. Mesnager, "Non-Linearized Amplifier and Advanced Mitigation Techniques: DVB-S2X Spectral Efficiency Improvement," in *GLOBECOM 2017 - 2017 IEEE Global Communications Conference*, Dec 2017, pp. 1–7.

[62] D. Spano, S. Chatzinotas, S. Andrenacci, J. Krause, and B. Ottersten, "Per-Antenna Power Minimization in Symbol-Level Precoding for the Multibeam Satellite Downlink," *International Journal of Satellite Communications and Networking*, vol. 37, no. 1, pp. 15–30, 2019.

[63] A. Mengali, R. B. S. Mysore, and B. Ottersten, "Joint Predistortion and PAPR Reduction in Multibeam Satellite Systems," in *2016 IEEE International Conference on Communications (ICC)*, May 2016, pp. 1–7.

[64] M. Baek, J. Yun, H. Lim, Y. Kim, and N. Hur, "Joint Masking and PAPR Reduction for Digital Broadcasting System with Faster-than-Nyquist Signaling," in *2017 IEEE International Symposium on Broadband Multimedia Systems and Broadcasting (BMSB)*, June 2017, pp. 1–2.

[65] G. Zheng, S. Chatzinotas, and B. Ottersten, "Generic Optimization of Linear Precoding in Multibeam Satellite Systems," *IEEE Transactions on Wireless Communications*, vol. 11, no. 6, pp. 2308–2320, June 2012.

[66] P. Arapoglou, K. Liolis, M. Bertinelli, A. Panagopoulos, P. Cottis, and R. De Gaudenzi, "MIMO over Satellite: A Review," *IEEE Communications Surveys Tutorials*, vol. 13, no. 1, pp. 27–51, First 2011.

[67] M. A. Vazquez, A. Perez-Neira, D. Christopoulos, S. Chatzinotas, B. Ottersten, P. D. Arapoglou, A. Ginesi, and G. Tarocco, "Precoding in Multibeam Satellite Communications: Present and Future Challenges," *IEEE Wireless Communications*, vol. 23, no. 6, pp. 88–95, December 2016.

[68] P. B. Ottersten, D. S. Chatzinotas, D. S. Andrenacci, D. J. M. Duncan, and D. M. Alodeh. (2017) SERENADE: Satellite Precoding Hardware Demonstrator. [Online]. Available: https://wwwfr.uni.lu/snt/technology_transfer_office/success_stories/serenade_satellite_precoding_hardware_demonstrator

[69] B. Hamet, T. Kolb, C. Rohde, F. Leschka, M. U. Pavan Bhave and, and A. Lidde, "Over-the-Air Operation of Mobile and Multicast Linear Precoding for a Multi-Spot-Beam Mobile Satellite Service," in *24th Ka and Broadband Communications Conference*, Oct 2018.

[70] P.-D. Arapoglou, A. Ginesi, S. Cioni, S. Erl, F. Clazzer, S. Andrenacci, and A. Vanelli-Coralli, "DVB-S2X-Enabled Precoding for High Throughput Satellite Systems," *International Journal of Satellite Communications and Networking*, vol. 34, no. 3, pp. 439–455, 2016. [Online]. Available: https://onlinelibrary.wiley.com/doi/abs/10.1002/sat.1122

[71] N. Letzepis and A. J. Grant, "Capacity of the Multiple Spot Beam Satellite Channel with Rician Fading," *IEEE Transactions on Information Theory*, vol. 54, no. 11, pp. 5210–5222, Nov 2008.

[72] D. Christopoulos, S. Chatzinotas, G. Zheng, J. Grotz, and B. Ottersten, "Linear and Nonlinear Techniques for Multibeam Joint Processing in Satellite Communications," *EURASIP Journal on Wireless Communications and Networking*, vol. 2012, no. 1, p. 162, May 2012.

[73] C. Masouros, "Correlation Rotation Linear Precoding for MIMO Broadcast Communications," *IEEE Transactions on Signal Processing*, vol. 59, no. 1, pp. 252–262, Jan 2011.

[74] V. Joroughi, M. R. B. Shankar, S. Maleki, S. Chatzinotas, J. Grotz, and B. Ottersten, "Robust Precoding Techniques for Multibeam Mobile Satellite Systems," in *2019 IEEE Wireless Communications and Networking Conference (WCNC)*, April 2019, pp. 1–8.

[75] C. Qi, H. Chen, Y. Deng, and A. Nallanathan, "Energy Efficient Multicast Precoding for Multiuser Multibeam Satellite Communications," *IEEE Wireless Communications Letters*, vol. 9, no. 4, pp. 567–570, April 2020.

[76] C. Qi and X. Wang, "Precoding Design for Energy Efficiency of Multibeam Satellite Communications," *IEEE Communications Letters*, vol. 22, no. 9, pp. 1826–1829, Sep. 2018.

[77] C. G. Tsinos, A. Arora, and B. Ottersten, "Constant-Envelope Precoding for Satellite Systems," in *ICASSP 2020 - 2020 IEEE International Conference on Acoustics, Speech and Signal Processing (ICASSP)*, May 2020, pp. 8807–8811.

[78] D. Christopoulos, S. Chatzinotas, and B. Ottersten, "Multicast Multigroup Precoding and User Scheduling for Frame-Based Satellite Communications," *IEEE Transactions on Wireless Communications*, vol. 14, no. 9, pp. 4695–4707, Sept 2015.

[79] B. Deng, C. Jiang, J. Yan, N. Ge, S. Guo, and S. Zhao, "Joint Multigroup Precoding and Resource Allocation in Integrated Terrestrial-Satellite Networks," *IEEE Transactions on Vehicular Technology*, vol. 68, no. 8, pp. 8075–8090, Aug 2019.

[80] A. Guidotti and A. Vanelli-Coralli, "Geographical Scheduling for Multicast Precoding in Multi-Beam Satellite Systems," in *2018 9th Advanced Satellite Multimedia Systems Conference and the 15th Signal Processing for Space Communications Workshop (ASMS/SPSC)*, Sep. 2018, pp. 1–8.

[81] Y. Gao, Y. He, W. Zheng, B. Li, and J. Wu, "Resource Scheduling for TH-Precoding Adoption on Multi-Beam Satellite Downlink Signals," in *16th International Conference on Advanced Communication Technology*, Feb 2014, pp. 1203–1207.

[82] A. Bandi, R. Bhavani Shankar Mysore, S. Chatzinotas, and B. Ottersten, "Joint User Scheduling, and Precoding for Multicast Spectral Efficiency in Multigroup Multicast Systems," in *2020 International Conference on Signal Processing and Communications (SPCOM)*, July 2020, pp. 1–5.

[83] V. Joroughi, M. . Vázquez, and A. I. Pérez-Neira, "Generalized Multicast Multibeam Precoding for Satellite Communications," *IEEE Transactions on Wireless Communications*, vol. 16, no. 2, pp. 952–966, Feb 2017.

[84] C. Mosquera, R. López-Valcarce, T. Ramírez, and V. Joroughi, "Distributed Precoding Systems in Multi-Gateway Multibeam Satellites: Regularization and Coarse Beamforming," *IEEE Transactions on Wireless Communications*, vol. 17, no. 10, pp. 6389–6403, Oct 2018.

[85] H. Prabhu, O. Edfors, J. Rodrigues, L. Liu, and F. Rusek, "Hardware Efficient Approximative Matrix Inversion for Linear Pre-coding in Massive MIMO," in *2014 IEEE International Symposium on Circuits and Systems (ISCAS)*, June 2014, pp. 1700–1703.

[86] H. Prabhu, J. Rodrigues, L. Liu, and O. Edfors, "Algorithm and Hardware Aspects of Pre-coding in Massive MIMO Systems," in *2015 49th Asilomar Conference on Signals, Systems and Computers*, Nov 2015, pp. 1144–1148.

[87] M. Chung, L. Liu, O. Edfors, and F. Tufvesson, "Demo: Millimeter-Wave Massive MIMO Testbed with Hybrid Beamforming," in *2020 IEEE Wireless Communications and Networking Conference Workshops (WCNCW)*, April 2020, pp. 1–2.

[88] J. Vieira, S. Malkowsky, K. Nieman, Z. Miers, N. Kundargi, L. Liu, I. Wong, V. Öwall, O. Edfors, and F. Tufvesson, "A Flexible 100-Antenna Testbed for Massive MIMO," in *2014 IEEE Globecom Workshops (GC Wkshps)*, Dec 2014, pp. 287–293.

[89] T. Wang, C. Liao, and T. Chiueh, "A Real-Time Digital Baseband MIMO Channel Emulation System," in *2007 IEEE International Symposium on Circuits and Systems*, May 2007, pp. 2606–2609.

[90] Q. Zhu, W. Huang, K. Mao, W. Zhong, B. Hua, X. Chen, and Z. Zhao, "A Flexible FPGA-Based Channel Emulator for Non-Stationary MIMO Fading Channels," *Applied Sciences*, vol. 10, no. 12, p. 4161, Jun 2020. [Online]. Available: http://dx.doi.org/10.3390/app10124161

[91] J. Garcia, S. Alfredsson, A. Brunstrom, and C. Beckman, "Train Velocity and Data Throughput - A Large Scale LTE Cellular Measurements Study," in *2017 IEEE 86th Vehicular Technology Conference (VTC-Fall)*, Sep. 2017, pp. 1–6.

[92] S. Boyd and L. Vandenberghe, *Convex Optimization*. Cambridge University Press, 2004.

[93] K. Lange and H. Zhou, "MM Algorithms for Geometric and Signomial Programming," *Mathematical Programming*, vol. 143, no. 1, pp. 339–356, Feb 2014. [Online]. Available: https://doi.org/10.1007/s10107-012-0612-1

[94] Y. Liu and W. Ma, "Symbol-Level Precoding is Symbol-Perturbed ZF when Energy Efficiency is Sought," in *2018 IEEE International Conference on Acoustics, Speech and Signal Processing (ICASSP)*, April 2018, pp. 3869–3873.

[95] A. Li and C. Masouros, "Interference Exploitation Precoding Made Practical: Optimal Closed-Form Solutions for PSK Modulations," *IEEE Transactions on Wireless Communications*, vol. 17, no. 11, pp. 7661–7676, 2018.

[96] A. Haqiqatnejad, F. Kayhan, and B. Ottersten, "Power Minimizer Symbol-Level Precoding: A Closed-Form Suboptimal Solution," *IEEE Signal Processing Letters*, vol. 25, no. 11, pp. 1730–1734, Nov 2018.

[97] B. M. Hochwald, C. B. Peel, and A. L. Swindlehurst, "A Vector-Perturbation Technique for Near-capacity Multiantenna Multiuser Communication Part II: Perturbation," *IEEE Transactions on Communications*, vol. 53, no. 3, pp. 537–544, March 2005.

[98] C. Masouros, M. Sellathurai, and T. Ratnarajah, "Vector Perturbation Based on Symbol Scaling for Limited Feedback MISO Downlinks," *IEEE Transactions on Signal Processing*, vol. 62, no. 3, pp. 562–571, Feb 2014.

[99] S. Domouchtsidis, C. G. Tsinos, S. Chatzinotas, and B. Ottersten, "Symbol-Level Precoding for Low Complexity Transmitter Architectures in Large-Scale Antenna Array Systems," *IEEE Transactions on Wireless Communications*, vol. 18, no. 2, pp. 852–863, Feb 2019.

[100] J. Krivochiza, A. Kalantari, S. Chatzinotas, and B. Ottersten, "Low Complexity Symbol-Level Design for Linear Precoding Systems," in *2017 Symposium on Information Theory and Signal Processing in the Benelux*. Delft University of Technology, 2017, p. 117.

[101] J. C. Merlano-Duncan, J. Krivochiza, S. Andrenacci, S. Chatzinotas, and B. Ottersten, "Computationally Efficient Symbol-Level Precoding Communications Demonstrator," in *2017 IEEE 28th Annual International Symposium on Personal, Indoor, and Mobile Radio Communications (PIMRC)*, Oct 2017, pp. 1–5.

[102] J. Krivochiza, J. C. Merlano-Duncan, S. Andrenacci, S. Chatzinotas, and B. Ottersten, "Closed-Form Solution for Computationally Efficient Symbol-Level Precoding," in *2018 IEEE Global Communications Conference (GLOBECOM)*, Dec 2018.

[103] J. Krivochiza, J. C. Merlano-Duncan, S. Chatzinotas, and B. Ottersten, "M-QAM Modulation Symbol-Level Precoding for Power Minimization: Closed-Form Solution," in *2019 16th International Symposium on Wireless Communication Systems (ISWCS)*, Aug 2019, pp. 395–399.

[104] J. Krivochiza, J. C. Merlano-Duncan, S. Andrenacci, S. Chatzinotas, and B. Ottersten, "Computationally and Energy Efficient Symbol-Level Precoding Communications Demonstrator," *Physical Communication*, vol. 28, pp. 108 – 115, 2018.

[105] J. Duncan, J. Krivochiza, S. Andrenacci, S. Chatzinotas, and B. Ottersten, "Hardware Demonstration of Precoded Communications in Multi-Beam UHTS Systems," in *36th International Communications Satellite Systems Conference (ICSSC)*, Oct 2018.

[106] R. Bro and S. De Jong, "A Fast Non-Negativity-Constrained Least Squares Algorithm," *Journal of Chemometrics*, vol. 11, no. 5, pp. 393–401, 1997.

[107] M. Alodeh, S. Chatzinotas, and B. Ottersten, "Constructive Multiuser Interference in Symbol Level Precoding for the MISO Downlink Channel," *IEEE Transactions on Signal Processing*, vol. 63, no. 9, pp. 2239–2252, May 2015.

[108] C. Lawson and R. Hanson, *Solving Least Squares Problems*. Society for Industrial and Applied Mathematics, 1995. [Online]. Available: http://epubs.siam.org/doi/abs/10.1137/1.9781611971217

[109] M. Grant and S. Boyd, "CVX: Matlab Software for Disciplined Convex Programming, version 2.1," http://cvxr.com/cvx, Mar. 2014.

[110] M. Grant and S. Boyd, "Graph Implementations for Nonsmooth Convex Programs," in *Recent Advances in Learning and Control*, ser. Lecture Notes in Control and Information Sciences, V. Blondel, S. Boyd, and H. Kimura, Eds. Springer-Verlag Limited, 2008, pp. 95–110, http://stanford.edu/~boyd/graph_dcp.html.

[111] Y. Luo and R. Duraiswami, "Efficient Parallel Nonnegative Least Squares on Multicore Architectures," *SIAM Journal on Scientific Computing*, vol. 33, no. 5, pp. 2848–2863, 2011. [Online]. Available: https://doi.org/10.1137/100799083

[112] M. K. Simon and M. S. Alouini, *Digital Communication over Fading Channels; 1st ed.* Newark, NJ: Wiley, 2000.

[113] S. Banerjee, *Linear Algebra and Matrix Analysis for Statistics (Texts in Statistical Science).* Chapman and Hall, jun 2014.

[114] J. Krivochiza, J. C. Merlano-Duncan, S. Andrenacci, S. Chatzinotas, and B. Ottersten, "Closed-Form Solution for Computationally Efficient Symbol-Level Precoding," in *GLOBECOM 2018 - 2018 IEEE Global Communications Conference*, Dec 2018.

[115] ETSI EN 302 307-2, "Digital Video Broadcasting (DVB); Second Generation Framing structure, Channel Coding and Modulation Systems for Broadcasting, Interactive Services, News Gathering and Other Broadband Satellite Applications; Part 2: DVB-S2 Extensions (DVB-S2X)," 2015.

[116] ETSI TS 102 376-1, "Digital Video Broadcasting (DVB); Implementation Guidelines for the Second Generation System for Broadcasting, Interactive Services, News Gathering and Other Broadband Satellite Applications; Part 1: DVB-S2," 2015.

[117] C. Politis, S. Maleki, J. M. Duncan, J. Krivochiza, S. Chatzinotas, and B. Ottesten, "SDR Implementation of a Testbed for Real-Time Interference Detection With Signal Cancellation," *IEEE Access*, vol. 6, pp. 20 807–20 821, 2018.

[118] S. Andrenacci, D. Spano, D. Christopoulos, S. Chatzinotas, J. Krause, and B. Ottersten, "Optimized Link Adaptation for DVB-S2X Precoded Waveforms Based on SNIR Estimation," in *2016 50th Asilomar Conference on Signals, Systems and Computers*, Nov 2016, pp. 502–506.

[119] J. Duncan, J. Querol, N. Maturo, J. Krivochiza, D. Spano, N. Saba, L. Marrero, S. Chatzinotas, and B. Ottersten, "Hardware Precoding Demonstration in Multi-Beam UHTS Communications under Realistic Payload Characteristics," in *37th International Communications Satellite Systems Conference (ICSSC 2019)*, 2019.

[120] N. E. Maammar, S. Bri, and J. Foshi, "Layered Offset Min-Sum Decoding for Low Density Parity Check Codes," in *2018 International Symposium on Advanced Electrical and Communication Technologies (ISAECT)*, Nov 2018, pp. 1–5.